bioRxiv preprint doi: https://doi.org/10.1101/2021.05.03.442497; this version posted November 12, 2021. The copyright holder for this preprint (which was not certified by peer review) is the author/funder. All rights reserved. No reuse allowed without permission.

Revisiting the Hayflick Limit: Insights from an Integrated Analysis of Changing Transcripts, Proteins, Metabolites and Chromatin

Michelle Chan[1], Han Yuan[1†], Ilya Soifer[1†], Tobias M. Maile[1], Rebecca Y. Wang[1], Andrea Ireland[1], Jonathon O'Brien[1], Jérôme Goudeau[1], Leanne Chan[1], Twaritha Vijay[1], Adam Freund[1], Cynthia Kenyon[1], Bryson Bennett[1], Fiona McAllister[1], David R. Kelley[1], Margaret Roy[1], Robert L. Cohen[1], Arthur D. Levinson[1], David Botstein[1‡], David G. Hendrickson[1‡]

[1]Calico Life Sciences, LLC

***For correspondence:**
botstein@calicolabs.com (FS);
dgh@calicolabs.com (FS)

[†]These authors contributed equally to this work
[‡]These are corresponding authors

Abstract The process wherein dividing cells exhaust proliferative capacity and enter into replicative senescence has become a prominent model for cellular aging *in vitro*. Despite decades of study, this cellular state is not fully understood in culture and even much less so during aging. Here, we revisit Leonard Hayflick's original observation of replicative senescence in WI-38 human lung fibroblasts equipped with a battery of modern techniques including RNA-seq, single cell RNA-seq, proteomics, metabolomics, and ATAC-seq. We find evidence that the transition to a senescent state manifests early, increases gradually, and corresponds to a concomitant global increase in DNA accessibility in nucleolar and lamin associated domains. Furthermore, we demonstrate that senescent WI-38 cells acquire a striking resemblance to myofibroblasts in a process similar to the epithelial to mesenchymal transition (EMT) that is regulated by the transcription factors YAP1/TEAD1 and TGF-$\beta 2$. Lastly, we show that verteporfin inhibition of YAP1/TEAD1 activity in aged WI-38 cells robustly attenuates this gene expression program.

Introduction

Replicative senescence in animal cells growing *in vitro* was first discovered by Leonard Hayflick. He found that primary human diploid fibroblast cell lines ceased to proliferate after an extended number of serial passages (***Hayflick, 1965***). Since then, considerable work has been done to describe this phenomenon. A major causal feature of replicative senescence is telomere erosion, a process in which the telomeres gradually shorten with increasing cellular divisions. Eventually, the telomeres become uncapped which triggers a DNA damage response that results in cell cycle exit (***Harley et al., 1990***). It is understood that this is due to the absence of the telomerase reverse transcriptase (hTERT), the catalytic component of human telomerase which adds telomeric sequences to the ends of chromosomes to maintain telomere length in germ cells and stem cells. As hTERT activity is undetectable in normal human somatic cells, telomere attrition is a common aging phenotype hypothesized to underlie cellular senescence at the organismal level (***López-Otín et al., 2013a***; ***Meyerson et al., 1997***). Replicative senescence of human somatic cell lines *in vitro* can be avoided by overexpression of hTERT which prevents telomere shortening and confers apparently unlimited replicative capacity (***Bodnar et al., 1998***).

bioRxiv preprint doi: https://doi.org/10.1101/2021.05.03.442497; this version posted November 12, 2021. The copyright holder for this preprint (which was not certified by peer review) is the author/funder. All rights reserved. No reuse allowed without permission.

Beyond growth arrest and telomere shortening, phenotypic changes exhibited in replicatively senescent cells include the senescence associated secretory phenotype (SASP). Proteins of the SASP include proinflammatory cytokines, growth factors, angiogenic factors, and proteases. The SASP has been shown to play a role in paracrine signaling whereby senescent cells can promote local wound healing and/or drive healthy neighboring cells into senescence (***Acosta et al., 2013***; ***Coppé et al., 2006***; ***Demaria et al., 2014***; ***Coppé et al., 2008***). Replicatively senescent cells also accumulate DNA and protein damage, accumulate lipids, and lose regulatory control of mitochondria and lysosomes (***Gorgoulis et al., 2019***).

The phenotypic similarity (telomere attrition, epigenetic alterations, mitochondrial dysfunction and loss of proteostasis) between the cell autonomous aging hallmarks and *in vitro* senescence has led to the hypothesis that senescent cells *in vivo* play a causal role in organismal aging and aging-related diseases (***Hernandez-Segura et al., 2018***; ***Campisi and Di Fagagna, 2007***; ***Sedelnikova et al., 2004***; ***Jeyapalan and Sedivy, 2008***; ***Herbig et al., 2006***; ***Childs et al., 2015***; ***López-Otín et al., 2013b***).

Consistent with this model several age-related disease states can be directly linked to telomere length or telomerase activity. For example to 15% of familial idiopathic pulmonary fibrosis cases arise from mutations in telomerase and up to 25% of sporadic cases occur in people with telomere lengths less than the 10th percentile. (***Tsakiri et al., 2007***; ***Armanios et al., 2007***; ***Cronkhite et al., 2008***; ***Alder et al., 2008***; ***Stuart et al., 2015***; ***Raghu et al., 2006***; ***Duckworth et al., 2021***; ***Stuart et al., 2014***; ***Dai et al., 2015***). Furthermore, the elimination of senescent cells in a number of age-related diseases, such as cardiac fibrosis, pulmonary fibrosis, neurodegenerative diseases, osteoporosis, and metabolic disorders have been argued to alleviate the disease state (***Pignolo et al., 2020***). Clinical trials for senolytics targeting fibrotic diseases, osteoporosis, frailty, and metabolic syndromes are currently underway (***Borghesan et al., 2020***).

The mechanism by which senescent cells might contribute to aging phenotypes is currently still unclear ***Hernandez-Segura et al.*** (***2018***, 2017). In an effort to bring clarity to the replicative senescence process *in vitro* that in turn could elucidate *in vivo* function, we revisited and redesigned the original Hayflick experiment. Making use of recent advances in high-dimensional technologies, (bulk RNA-seq, single cell RNA-seq (scRNA-seq), ATAC-seq, metabolomics and proteomics) we tracked changes throughout the replicative lifespan of the original Hayflick WI-38 cell line.

Overall, our data recapitulate many known features of the *in vitro* senescence process while simultaneously providing novel insight. First, the time resolution of our experiment coupled with single cell trajectory analysis reveals that senescence is a gradual process that shares transcriptional, proteomic, and metabolomic features with epithelial-mesenchymal transition (EMT). Second, our metabolomic data identifies Nicotinamide N-methyltransferase (NNMT) activity as a potential initiating event in replicative senescence dependent loss of silenced genomic regions. Third, we show that these genomic regions that exhibit increased accessibility with increasing cellular age are concentrated in nucleolar/lamin associated domains and correspond with observed changes in the replicative senescence transcriptome. Lastly, integration across data modalities reveals that replicatively senescent WI-38 cells bear a strong resemblance to myofibroblasts. We provide bioinformatic and experimental evidence that the YAP1/TEAD1 transcription factor complex and TGF-β2 signaling are putative regulators of the transition to this state. Together our data suggests that a process similar to fibroblast to myofibroblast transition (FMT; analogous to EMT) is an intrinsic aspect of the replicative senescence phenotype in WI-38 fibroblasts.

Results

Transcriptomic profiles of replicative senescence (RS), radiation induced senescence and increasing cellular density.

To capture the replicative senescence process with high resolution we designed an experiment to continuously grow and intermittently sample cells from a starter batch of WI-38 cells that had undergone only 20 population doublings (PDL 20) (Supplemental methods). To distinguish between

bioRxiv preprint doi: https://doi.org/10.1101/2021.05.03.442497; this version posted November 12, 2021. The copyright holder for this preprint (which was not certified by peer review) is the author/funder. All rights reserved. No reuse allowed without permission.

replicative senescence dependent changes and those arising from altered cell density and growth rate, we performed a cell density control study (Supplemental methods). Briefly, early PDL cells were sampled at increasing levels of cell density to measure gene expression changes associated with cellular density and decreasing cell proliferation independent of replicative senescence (Figure 1A). In addition to the cell density control, we also included TERT immortalized WI-38 cells (hTERT) grown in parallel and sampled alongside WT cells as a control for long term culturing and day-to-day sampling batch effects (***Bodnar et al., 1998***). The hTERT cell line was generated in advance of the experiment. Frozen aliquots of the hTERT line were thawed alongside and sampled in parallel with WT WI-38 cells. As expected, hTERT immortalized cells grew at a constant rate and did not slow or cease growth (Figure 1B).

We also included a radiation induced senescence condition to test for differences between replication and radiation induced senescence and to isolate changes arising from acute DNA damage response. Finally, we sampled proliferating WT and hTERT WI-38 cells at multiple PDLs for RNA-seq, scRNA-seq, proteomics, metabolomics and ATAC-seq until the WT WI-38 cells had reached senescence as measured by the cessation of growth (Figure 1B, Figure 1 supplement 1).

We first examined the bulk RNA-seq data to compare and contrast replicative senescence with radiation induced senescence, cell density, and hTERT cells (quality control metrics located in Figure 1 source data 1). Differential gene expression analysis using RNA-seq revealed 6,955 genes change with increasing PDL, 7,065 genes change in response to ionizing radiation, and 9,958 genes vary with increasing cell density (FDR adjusted p-value < 0.01, Figure 1 source data 2). Notably, the transcriptional changes we observed were consistent with previous studies. Figure 1D shows the strong correlation of the pattern of induced transcription established in our PDL 50 cultures and the fibroblast derived senescence-associated signature compiled across multiple fibroblast senescence gene expression experiments from cell lines derived from different tissue depots (***Hernandez-Segura et al., 2017***). We also observed induction of senescence-associated-β galactosidase activity (Figure 1C) as well as p16 and p21 in both our RNA-seq, proteomics data, and via western blot (Figure 1 supplement 2, Figure 1 supplement 3). These data reveal that the cells in our time course display classic features of senescent cells and exhibit transcriptomic changes that are highly correlated with previous studies of replicative senescence. Together, these data strongly suggest that our WI-38 cells successfully reached replicative senescence.

Hierarchical clustering of all significantly changing genes across the four conditions highlighted several important features of our experiment. First, as expected, gene expression in the hTERT-immortalized WI-38 cells remained largely stable. Second, replicative senescence, radiation induced senescence, and cell density exhibited many shared, but also unique, gene expression changes with respect to both the identity of differentially expressed genes and the magnitude of their changes (Figure 1E).

To facilitate a biological interpretation of these shifting transcriptomic landscapes, we applied Gene Set Enrichment Analysis (GSEA) using the MSigDB Hallmark annotation sets to learn which general processes are shared and distinct between replicative senescence, radiation induced senescence, and cell density (Figure 1F, Figure 1 source data 3) (***Liberzon et al., 2015***; ***Subramanian et al., 2005***; ***Mootha et al., 2003***). All three perturbations (and not the immortalized cells), exhibited dramatic reductions in expression of genes belonging to S, G2M, and M cell cycle phases, consistent with cessation of cell division (Figure 1F - top cluster). Perhaps driven by this shift, we also found significant overlap in additional enriched annotations among genes induced in replicative senescence, radiation induced senescence and cell density, albeit with some variation in significance. Many of the shared enriched annotations can be categorized as stress responses, e.g. apoptosis, p53 pathway, inflammatory and interferon responses, and STAT3/5 signaling. In addition, we also observed enrichment of several development/diff0erentiation gene sets, including myogenesis, angiogenesis, and adipogenesis.

We observed relatively few gene sets with discordant patterns across the replicative senescence, radiation induced senescence, and cell density experiments (Figure 1E). However, the gene

bioRxiv preprint doi: https://doi.org/10.1101/2021.05.03.442497; this version posted November 12, 2021. The copyright holder for this preprint (which was not certified by peer review) is the author/funder. All rights reserved. No reuse allowed without permission.

set for Epithelial to Mesenchymal Transition (EMT) was significantly enriched in genes that increased with replicative senescence as opposed to radiation induced senescence (Benjamini-Hochberg corrected p=5.5e-6 vs. Benjamini-Hochberg corrected p=0.12) or cell density wherein the term was actually underrepresented, but not significantly so (Benjamini-Hochberg corrected p=0.4). Although replicative senescence, radiation induced senescence and cell density are highly similar at the abstracted level of enriched gene sets, it is clear in Figure 1E that there are many induced genes specific to replicative senescence. In addition, we applied GSEA to each individual time point for each condition (Figure 1 supplement 4, Figure 1 source data 4) and found the EMT gene set is enriched early and robustly during replicative senescence. Thus the EMT gene set appears to represent a particularly important aspect of replicative senescence biology.

Single-cell RNA-seq reveals that replicative senescence is a gradual process

Interestingly, the vast majority of gene expression changes evident by PDL 50 begin to manifest at much earlier PDLs. This observation is consistent with two distinct possibilities: (A) The senescence expression changes accrue early and gradually in the majority of cells without respect to proliferation status, or (B) the bulk RNA-seq profiles are a changing admixture of transcriptionally distinct mitotic, G1, and senescent cells. Both models have substantial support in the literature (***Tang et al., 2019***; ***Wiley et al., 2017***; ***Nassrally et al., 2019***; ***Whitney et al., 1980***; ***Passos et al., 2007***; ***Smith and Whitney, 1980***). To discriminate between these possibilities, we employed single-cell RNA-seq (scRNA-seq) to directly measure percentages of senescent and cycling cells.

Briefly, we collected between 1,000-2,000 cells at increasing PDLs of WI-38s and matched hTERT time points at beginning and end of time course. We applied a modified (see methods) 10X Genomics protocol to capture and preserve the more fragile senescent cells (Figure 2 supplement 1). We profiled a total of 11,000 cells (9,000 WT and 2,000 hTERT). When aggregated into pseudo-bulk profiles (i.e the sum the single-cell reads) expression profiles, the single cell results are highly correlated with expression changes observed in bulk RNA-seq (r=0.81), Figure 2 supplement 2).

We first classified cells as either S, G2M, or G1 phase using canonical markers for the S and G2M phases as previously described ***Nestorowa et al.*** (***2016***). As expected, based on bulk transcriptomics, the number of cells in either S or G2M decreases with increasing PDL whereas the cycling cell proportions are stable in the hTERT timepoints (Figure 2A,B).

Next, we projected all wild type (WT) cells and two hTERT time points together to identify broad patterns in replicative aging PDL cells versus cycling hTERT cells. To do this, we employed UMAP projection as opposed to t-SNE as the former is faster and preserves local structure more so than the latter (***McInnes et al., 2018***). Cells from the two cell lines organize separately, however share a similar geometry composed of a S/G2M phase roundabout and a large G1 lobe (Figure 2C). Although the overall pattern of WI-38 cells for both cultures was highly similar, we observed progression of cell grouping with PDL that had no concordance with increasing hTERT time points (Figure 2D - red to blue). Specifically, PDL 50 cells (but not the temporally paired hTERT PDL.ctrl 50 time point) organize apart from all other cells within the UMAP. To test if these cells were senescent, we scored all cells with a senescent gene expression signature derived from the bulk RNA-seq and found that the highest scoring cells reside within this grouping composed of PDL 50 cells (methods) (Figure 2 supplement 4).

To test model A vs B, we compared the pseudo-bulk gene expression profiles across the cell cycle at each PDL. We reasoned that if replicative senescence were gradual, we would observe the replicative senescence gene expression pattern even in young cycling cells without respect to G1/S/G2M. Indeed, the replicative senescence signature is present in all cell cycle phases even in early PDLs (Figure 2E- left panels vs. far right panel). In addition, bioinformatic segregation and UMAP projection of cells scored as S/G2M phase cells revealed that the dominant source of variance in cycling cells is the PDL (Figure 2 supplement 3). Lastly, we did not observe any cells < PDL 50 in close association with the senescent cells in the UMAP projection PDLs (Figure 2C,D).

It has previously been reported and observed here (Figure 2 supplement 5) that cell size in-

bioRxiv preprint doi: https://doi.org/10.1101/2021.05.03.442497; this version posted November 12, 2021. The copyright holder for this preprint (which was not certified by peer review) is the author/funder. All rights reserved. No reuse allowed without permission.

creases with PDL in primary cell lines (***Ogrodnik et al., 2019***). We hypothesized that perhaps the higher PDL cells by nature of their larger size, might reach contact inhibition faster than early PDL cells. In this scenario, given the high correlation between the gene expression signatures of senescence and cell density, the increase in senescence signature could be an artifact of cell culture arising from changing morphology. To test this possibility, we scored our single cells again with modified signatures for senescence and cell density composed only of genes uniquely induced in either perturbation (Figure 2 supplement 4). We found that the specific senescent signature increases with PDL in WT WI-38 cells in contrast with the specific cell density signature which stays relatively flat. These data provide more evidence supporting a gradual increase in the senescent gene expression program that is independent from changes in cell density.

Together, these results argue in favor of a gradual model (A) of replicative senescence wherein cells ramp up expression of the replicative senescence program with increasing PDL even when still proliferative. We cannot rule out there are a small minority of cells that enter senescence early in the experiment as previously reported (***Smith and Whitney, 1980***; ***Passos et al., 2007***). However, for the lineages of cells that make it to PDL 50, we observe that the senescent gene expression program manifests in their primogenitors. These data are also consistent with the previously reported changes in cellular phenotype (larger cell size and increased cycling time) with increasing PDL (***Macieira-Coelho and Azzarone, 1982***; ***Ogrodnik et al., 2019***; ***Neurohr et al., 2019***; ***Absher et al., 1974***). Importantly, this observation suggests that aspects of cellular senescence are present in non-senescent cells. This result raises the intriguing possibility that the reported pathological features of senescent or senescent-like cells *in vivo* might also manifest in cells that are not classically senescent.

Proteomic landscape of replicative senescence WI-38 cells suggests large metabolic alterations

We next turned to our proteomics data generated from the same cultures and time points as above. We obtained high confidence measurements for ~8500 proteins (Figure 3 supplement 1, Figure 3 source data 1). Similar to our transcriptional results, the hTERT samples did not exhibit large changes in the proteome with experimental progression (Figure 3 supplement 1). Overall, we observed high concordance between transcript and protein levels with very few outliers (r=0.71 for PDL 50 vs PDL 20, Figure 3 supplement 2). We employed GSEA using hallmark annotations and observed a sharp depletion of proliferation and mitosis associated gene sets supporting our previous findings (Figure 3A, Figure 3 source data 1). Likewise, the proteomics data recapitulated enrichment of the EMT annotation set along with the adipogenesis and myogenesis.

Multiple enriched sets pointed to replicative senescence dependent shifts in cellular energy utilization (Figure 3A). Of note, we found that although under-enriched in our replicative senescence transcriptome (Figure 1F), The oxidative phosphorylation hallmark was highly enriched in the proteomics data. We plotted the oxidative phosphorylation genes driving the set enrichment in Figure 3 supplement 2. This projection revealed that many genes in this set fall into a quadrant (positive proteomic, negative transcriptomic) suggesting discordant regulation of these genes.

The oxidative phosphorylation hallmark set is composed of multiple closely linked mitochondrial complexes and functions that regulate cellular energy flux e.g. TCA cycle, fatty acid oxidation, pyruvate metabolism, ATP synthase etc. We divided the oxidative phosphorylation gene set into into these constituent parts and visualized the changes in proteins with increasing PDL. We observed PDL-dependent increased in proteins from all categories except for mitochondrial assembly and structures. These results are consistent with altered mitochondrial function (Figure 3 supplement 3).

Next, we examined the annotations for the highest enriched hallmark sets from Figure 3A and found strong enrichment of multiple KEGG metabolic pathways. (Figure 3B). In addition, both the glucose transporter SLC2A1/GLUT1 and the fatty acid scavenger CD36 transcripts exhibited strong, early, and replicative senescence specific up-regulation (Figure 3C). Together these results point to

bioRxiv preprint doi: https://doi.org/10.1101/2021.05.03.442497; this version posted November 12, 2021. The copyright holder for this preprint (which was not certified by peer review) is the author/funder. All rights reserved. No reuse allowed without permission.

a drastically altered replicative senescence metabolic landscape.

RS WI-38 cells exhibit increased utilization of fatty acid metabolism and glycolytic shunts

To generate a metabolic profile for replicative senescence in WI-38 cells, we harvested samples at increasing PDLs alongside input material for all other data types (methods). From our metabolomics data, we identified 285 compounds (Figure 3 supplement 4, Figure 3 source data 2). To remove batch effects that were observed in several PDL and the matched hTERT samples, we corrected each PDL with its paired hTERT sample. We then calculated significant changes over time for each metabolite (FDR adjusted $p < 0.05$, Figure 3 source data 2). To further guide our metabolic analysis, we focused our queries based on the enriched metabolic pathways found in the proteomic analysis. Specifically we studied the changes to glycolysis, oxidative phosphorylation and fatty acid metabolism (Figure 3D).

Following the glucose, we looked at the central stem of glycolysis as a potential source of energy supplying the observed increases in the TCA cycle and oxidative phosphorylation (Figure 3D,E). We found that metabolites and enzymes dedicated to pyruvate generation and/or lactate production did not change concordantly. We instead found that most of the glycolytic shunts exhibited up-regulation at both the metabolite and protein level (Figure 3E). These results suggest an increase in allocation of glucose for manufacture of various biomolecules and their precursors (glycogen, hexosamines, phospholipids) (Figure 3E).

In contrast, metabolites and enzymes involved in fatty acid import and oxidation for the purpose of energy generation appear strongly up-regulated (Figure 3E). We also saw that metabolites involved in the *de novo* production of phospholipids via the Kennedy pathway are highly up-regulated, specifically phosphotidylethanolamines precursors (Figure 3 supplement 5).

From these data, it is clear that replicative senescence WI-38 cells undergo drastic shifts in metabolism. Specifically, we see increased glucose utilization in glycolytic shunts coupled with an increase in fatty acid import and oxidation. It is possible that replicative senescence cells are switching to fatty acid oxidation to fuel increased TCA cycling and oxidative phosphorylation as glucose is diverted to macromolecule production. Indeed, metabolomic data collected from various types of senescence models has shown increased fatty acid oxidation, lipid accumulation, TCA up-regulation, and glycolytic alterations (***Zwerschke et al., 2003***; ***Ogrodnik et al., 2017***; ***Flor et al., 2017***; ***Unterluggauer et al., 2008***; ***Johmura et al., 2021***). Likewise, consensus metabolomic findings in EMT models report increased TCA cycle products, altered lipid metabolism, and activated hexosamine pathway (***Hua et al., 2020***; ***Corbet et al., 2020***; ***Lucena et al., 2016***). These data provide functional metabolic evidence supporting a connection between replicative senescence and the EMT hallmark enrichment observed in RNA and protein expression.

Nicotinamide N-methyltransferase (NNMT) links nicotinamide adenine dinucleotide (NAD) and methionine metabolism as a putative heterochromatin regulator

Metabolic regulation of epigenetic state is an increasingly recognized mechanism through which nutrient availability influences cellular function by regulating the abundance of co-factors required for histone modifications (***Lu and Thompson, 2012***). Specifically, Nicotinamide adenine dinucleotide (NAD+) and methionine metabolism power the deacetylation and methylation required for maintaining repressive DNA conformations (***Lu and Thompson, 2012***). In a compelling intersection, perturbation of NAD, methionine, and heterochromatin levels have all previously been reported in multiple aging contexts including replicative senescence (***James et al., 2016***; ***López-Otín et al., 2016***; ***Kozieł et al., 2014***; ***Yousefzadeh et al., 2020***; ***Benayoun et al., 2015***). In compiling our replicative senescence data for the metabolic and proteomic components of the NAD and methionine pathways, we found that one of the largest and earliest changes for any protein (or transcript) was the increased expression of Nicotinamide N-methyltransferase (NNMT) (Figure 4A,B).

bioRxiv preprint doi: https://doi.org/10.1101/2021.05.03.442497; this version posted November 12, 2021. The copyright holder for this preprint (which was not certified by peer review) is the author/funder. All rights reserved. No reuse allowed without permission.

DNA and histone methylation require abundant levels of the universal methyl donor S-adenosyl methionine (SAM). NNMT not only depletes SAM by catalyzing the removal of the SAM methyl group, it does so by fusing it to the NAD+ precursor nicotinamide (NAM) resulting in the production of methyl nicotinamide (MNA) (***Ulanovskaya et al., 2013***). Thus, NNMT effectively acts as a sink for the two primary metabolites a cell requires for silencing chromatin and regulating gene expression (***Komatsu et al., 2018***). We found that MNA levels mirror those of NNMT; increasing early and robustly during replicative senescence progression consistent with high NNMT activity. SAM and its sans-methyl version (S-adenosyl homocysteine (SAH)) were depleted with replicative senescence albeit to a lesser extent than the observed increase in MNA. NAMPT and NMNAT1, enzymes in the NAD salvage pathway, were weakly down-regulated at the protein level (Figure 4A,B).

High NNMT expression has been implicated in methyl depletion in embryonic stem cells and cancer-associated fibroblasts (CAFs) (***Eckert et al., 2019***; ***Sperber et al., 2015***). In both cases the functional consequences were similar; DNA hypomethylation and decreased capacity to form or maintain silenced loci and heterochromatin. The important point is that the loss of silencing is actively promoted through NNMT activity. One intriguing hypothesis is that increased NNMT activity with replicative senescence promotes loss of silencing and heterochromatin via SAM depletion (Figure 4C).

Increased DNA accessibility and transcription from nucleolar and lamin associated domains is a dominant feature of the replicative senescence epigenome

To study genome-wide changes in the epigenetic landscape of senescent cells, we collected ATAC-seq data during the replicative senescence time course. We size selected our ATAC-seq libraries for smaller fragments (< 300 base pairs) to enrich for nucleosome free regions (Figure 5 supplement 1 and Figure 5 supplement 2). Samples from all PDLs and hTERT PDL controls exhibited similar ATAC-seq fragment size distribution emblematic of nucleosomal patterning, high alignment rates, very low mitochondrial read percentages, and strong enrichment around transcriptional start sites (Figure 5 supplement 1, Figure 5 supplement 3, Figure 1 source data 1). These QC metrics are indicative of high quality ATAC-seq libraries at all sampling time points and PDLs. We then quantified the read distribution across chromatin states previously annotated for another human fetal lung fibroblast cell line (IMR-90, Figure 5 source data 1) (***Ernst and Kellis, 2015***). We categorized 25 distinct states into 4 broad categories: promoters, enhancers, transcription, and miscellaneous, the last of which is composed largely of heterochromatic and undefined states, e.g. H3K9me3 and H3K27me3 rich regions, zinc-finger repeats, and quiescent (defined by the absence of histone marks, accessibility, or gene features) which we refer to as "undefined" (***Ernst and Kellis, 2015***).

In comparing the read distribution into chromatin states between hTERT immortalized cells and WT WI-38 cells of increasing PDL, we observed an increase in ATAC-seq reads falling into the undefined chromatin regions at the relative cost to all other states (Figure 5A-left panel). We plotted the read distribution across chromatin states as a function of increasing time for both cell lines and found these shifts to be associated with increasing PDL in the WT WI-38 cells; hTERT ATAC-seq read proportions across chromatin states remained stable over time (Figure 5A-right panel).

To determine if this shift in accessibility to undefined and heterochromatic states was indicative of increasing noise versus coherent changes in accessibility, we used the ATAC-seq reads to call peaks of localized accessibility. From the WT and hTERT ATAC-seq data from all time points we identified 363,470 ATAC-seq peaks (***Zhang et al., 2008***) (Figure 5 source data 2 and 3). We found a slight ~5% but significant (p=0.014) linear PDL-dependent decrease in the fraction of reads in peaks during replicative senescence (Figure 5 supplement 4A, Figure 5 source data 4). We tested experimentally whether the increased heterochromatic accessibility was an artifact of increasing numbers of dead cells in later PDL samples by repeating the experiment using late (PDL 45) cells with a cross-linking agent (propidium monoazide-PMA) that renders DNA from dead cells inert as previously described (***Hendrickson et al., 2018***). No significant change in read distribution across

bioRxiv preprint doi: https://doi.org/10.1101/2021.05.03.442497; this version posted November 12, 2021. The copyright holder for this preprint (which was not certified by peer review) is the author/funder. All rights reserved. No reuse allowed without permission.

chromatin states was observed with addition of PMA (Figure 5 supplement 4B).

We then divided the ATAC-seq peaks into each of the 25 discrete chromatin states and calculated the fold change in accessibility for each state and PDL compared to the first sample. We observed that changes in peak accessibility mirrors that for all reads. Again we observed a clear increase in accessibility with PDL across the miscellaneous category with a concomitant decrease in all other states in WT WI-38 cells and not in immortalized hTERTs (Figure 5B).

The quiescent or "undefined" state from the miscellaneous category piqued our interest for two reasons, one being that it alone accounted for 20-40% of all ATAC-seq reads and a large 10% increase with senescence. The second point of interest was the observed early onset of change (Figure 5A,B). Dillinger et. al. previously reported that the quiescent state is largely overlapping with both LADs and NADs (***Dillinger et al., 2017***; ***Sadaie et al., 2013***) (Figure 5 source data 5 and 6). Likewise, we found that the undefined chromatin domains and most of the heterochromatic domains to be markedly gene poor and overwhelmingly overlapping with both LADs and NADs experimentally defined in IMR-90 fibroblasts (Z-score 90 and 150) (Figure 5 supplement 4C). For reference, Figure 5 supplement 4E provides a chromosome level view of the significant overlap between replicative senescence accessible ATAC-seq peaks in the quiescent state with NADs and LADs compared to all peaks annotated in WI-38 cells.

To control for the fact that the chromatin state annotations we used were derived from a different, albeit closely related, cell line, we performed the same analysis using gene annotations which are cell line independent. We found that peaks in intergenic regions increase in accessibility with PDL on average consistent with the undefined gene poor annotation from IMR-90 cells. These results suggest that the chromatin states defined in IMR-90 cells are capturing the chromatin states in WI-38 cells (Figure 5 supplement 4D).

We tested and found that ATAC-seq peaks falling within NADs and LADs exhibit increased accessibility with replicative senescence ($p < 10$ e-16 for both: Wilcoxon rank-sum test). Notably, this trend was much greater for peaks in NADs versus peaks in LADs, with a median log2 fold change of 0.98 for NADs vs. 0.24 for LADs (Figure 5D).

Digging deeper into NADs, we next asked if chromatin states within NADs might respond differently than the rest of the genome to increasing PDL given the large PDL-dependent increase in accessibility we observed in Figure 5D. We repeated the analysis shown in Figure 5B with two subsets; peaks excluded from NADs or peaks overlapping NADS. (Figure 5 supplement 5). Dividing these two sets of peaks into the 25 chromatin states revealed that as expected, NAD excluded peaks mirror the pattern observed for significantly changing peaks across all chromatin states. Conversely peaks overlapping NADs were found to increase in accessibility in a variety of chromatin states (e.g. poised promoters and many classes of enhancers) that exhibit reduced accessibility across the rest of the genome with increasing PDL.

One interpretation is that although the aggregate peak accessibility data appear to suggest that transcription is globally shutting down, the NAD specific view reveals rather that transcription is induced in a subset of loci. Although widespread, the reduced accessibility in euchromatin we observed in aggregate is not reflective of a pervasive shutdown of transcription across the entire genome. To formally test this hypothesis, we next asked if the shifts in NAD/LAD accessibility correlate with productive transcription and found that indeed, senescence induced genes significantly overlap NAD domains. Radiation and cell density induced genes exhibited weaker (cell density) or nonexistent (radiation) overlap with NADs and LADs. These data suggest that increasing accessibility in LADs and specifically NADs is a prominent feature of the replicative senescence epigenome that is directly connected to the senescent gene expression program (Figure 5C).

Together these results highlight a striking increase in accessibility within nucleolar associated DNA that connects changes in the transcription with a global shift in the epigenome.

bioRxiv preprint doi: https://doi.org/10.1101/2021.05.03.442497; this version posted November 12, 2021. The copyright holder for this preprint (which was not certified by peer review) is the author/funder. All rights reserved. No reuse allowed without permission.

Transcriptional regulators of the replicative senescence transcriptome and epigenome

To parse out the regulatory logic of replicative senescence gene expression, we leveraged our ATAC-seq data to gain insight into which transcription factors regulate replicative senescence accessibility via transcription factor motif analysis. Having cataloged a universe of ATAC-seq peaks with significant changes in accessibility, we next assigned peaks to neighboring genes. Taking the top replicative senescence differentially expressed genes, we searched the proximal ATAC-seq peaks enriched transcription factor motifs (Figure 6A). We found enriched motifs for TEAD1, CEBP family transcription factors, SMAD EMT transcription factors, AP1 transcription factors, and multiple FOX family transcription factor motifs.

We also applied an orthogonal gene-independent methodology for determining which motifs are predictive of replicative senescence induced increases in ATAC-seq peak accessibility. Consistently, we again found TEAD1 to be the most predictive feature (mean coefficient = 0.25 across 10 models-methods). In addition, we also found evidence for FOXE1 and SMAD1 regulation as well as other senescence related transcription factors, e.g. CEBPB and TP53 (Figure 6B).

Out of the FOX family transcription factors, FOXE1 is unique in that it exhibits one of the most specific (no change in hTERT, cell density or radiation) and largest increases in replicative senescence gene expression (40-50x) (Figure 6 supplement 1). FOXE1 is annotated as a thyroid specific transcription factor with putative roles in thyroid development and cancer (**?*Kallel et al., 2011***; ***Ding et al., 2019***). It has also been reported to regulate two signaling molecules up-regulated in the replicative senescence time course; TGF-β3 and WNT5A ***Venza et al.*** (***2011***); ***Pereira et al.*** (***2015***). Furthermore, it has been reported that many of the FOX family transcription factors are relatively promiscuous binders of each others canonical motifs. Thus it is possible that the increased accessibility in peaks with FOX motifs during replicative senescence may be driven by FOXE1 activity ***Rogers et al.*** (***2019***). Despite the specificity and magnitude of replicative senescence induction, FOXE1's function in replicative senescence is unclear and warrants further investigation.

We returned to our bulk RNA-seq to test for enrichment of protein-DNA binding events (mapped by ENCODE) in regulatory elements proximal to our replicative senescence differentially expressed genes by using Landscape *in silico* deletion Analysis (LISA) (***Qin et al., 2020***). Plotting transcription factor enrichment for genes depleted with replicative senescence against genes induced during replicative senescence revealed 3 broad cohorts of transcription factors; proliferating cell transcription factors, replicative senescence transcription factors, and transcription factors whose binding was enriched around both sets of genes (Figure 6C). As expected, proliferation specific transcription factors are replete with cell cycle specific transcription factors e.g. E2F and RBP family transcription factors. A large portion of the transcription factors exhibiting replicative senescence specificity belong to 4 categories; inflammation transcription factors (NFKB, CEBPB), AP1 subunits (JUN,JUND,FOSL2), YAP1-TEAD1 components (TEAD1/4, YAP1, WWTR1), and EMT transcription factors (SNAI2, TCF21).

TEAD1 is a member of the TEA domain transcription factors whose functions range across a wide swath of biology depending on context and binding partner. TEAD transcription factors cannot induce gene expression without a cofactor, which is most often YAP1 (yes-associated protein 1) a key downstream effector of Hippo signaling. (***Azakie et al., 2005***; ***Chen et al., 1994***; ***Benhaddou et al., 2012***; ***Yu et al., 2015***; ***Landin Malt et al., 2012***; ***Vassilev et al., 2001***; ***Zhao et al., 2008***; ***Ma et al., 2019***; ***Piccolo et al., 2014***). Consistent with our identification of TEAD1 and YAP1 as replicative senescence regulators, YAP1 activation has been tied to EMT, anti-apoptosis, telomere dysfunction, inflammation, and positive regulation of fatty acid oxidation (***Kurppa et al., 2020***; ***Lee et al., 2019***; ***Peng et al., 2017***; ***Zhang et al., 2017***; ***Chakravarti et al., 2020***).

Lastly, given that YAP1/TEAD1 activity appears to increase during replicative senescence against the backdrop of an altered epigenomic context, we tested for an interaction between TEAD1 motifs and the increasingly accessible NADs and LADs. We found that not only are TEAD1 sites significantly enriched within NADs and LADs (($p < 7.17e-07$, and $p < 6.12e-03$ respectively hypergeometric), but

bioRxiv preprint doi: https://doi.org/10.1101/2021.05.03.442497; this version posted November 12, 2021. The copyright holder for this preprint (which was not certified by peer review) is the author/funder. All rights reserved. No reuse allowed without permission.

we also discovered a greater-than-additive increase in accessibility with replicative senescence for TEAD1 motifs that occur within a NAD ($p < 3.12$ e-07). These results suggest that there is a functional connection between TEAD1 activity and NAD domains during replicative senescence The changing epigenetic context of replicative senescence may alter TEAD1 binding and thus target activity with increasing PDL.

Collectively, these analyses uncover a common theme amongst putative regulatory transcription factors; Hippo signaling (YAP1/TEAD1), EMT transcription factors, and TGF-β signaling (SNAI2, SMAD activity). SNAI2 has been shown to work in tandem with the YAP1/TEAD1 complex and these pathways often work towards similar biological ends (***Tang et al., 2016***; ***Kurppa et al., 2020***). Together, these transcription factors are reported as highly involved with proliferation, EMT, ECM production, fibrosis, and apoptosis avoidance (***Kim et al., 2019a***).

Lastly, given that the LISA results are based on binding events collected from a vast multitude of cell lines, we wondered if the same transcription factors might be found to regulate senescence in a completely different cellular context. To test this we took significantly induced genes from a senescence model using astrocytes and oxidative stress as the senescence trigger (***Crowe et al., 2016***). Plotting transcription factor enrichment for genes induced in astrocyte senescence against transcription factor enrichment for WI-38 replicative senescence genes revealed that although there were a substantial number of discordant transcription factors, there was a clear population of transcription factors highly enriched in both senescence models (Figure 6D). Notably, the top concordant transcription factors ranked at the top in both contexts and recapitulate all the previous results e.g. YAP1/TEAD1, SNAI2, CEBP family transcription factors and AP1 subunits.

scRNA-seq trajectory analysis resolves WI-38 cells' approach to replicative senescence

A wealth of recent work in single cell transcriptomics has demonstrated that ordering single cells in a process-specific trajectory often reveals nuanced timing and dynamics of gene expression that bulk assays cannot capture (***Qiu et al., 2017***; ***Trapnell et al., 2014***). Mapping this trajectory is frequently referred to as "pseudotime analysis". We employed pseudotime analysis to arrange single WI-38 cells along a pathway to senescence setting proliferating cells as the trajectory "root". As expected, early and late PDL cells concentrated at the beginning and end of the pseudotime trajectory respectively (Figure 7A). We next performed differential expression analysis to identify genes that change significantly over pseudotime. We plotted examples of genes changing early (CENPK–an S-phase cell-cycle-regulated gene), midway (SNAI2–a master regulator of EMT), or late (PAPPA–a prominent SASP factor) in pseudotime in Figure 7B.

We next generated gene expression trajectories for the top (by significance $p < 0.001$) 5,000 differentially expressed genes across pseudotime (Figure 7 supplement 1, Figure 7 source data 1). To identify the temporal relationship between the biological processes and transcription factors that compose replicative senescence in WI-38 cells, we clustered and ordered pseudotime trajectories (Figure 7 supplement 2). Broadly, we classified the pseudotime expression pattern as early, transition, or late based on the maximum median value of all constituent genes for each cluster (Figure 7C). We performed LISA transcription factor and GO enrichment analysis on each cluster and used our findings to assign putative functional labels across pseudotime (Figure 7D, Figure 7 supplement 2, Figure 7 source data 1 and 2).

Early pseudotime is dominated by the transcription factors (E2F) and GO terms associated with cell cycle progression through the G2M and S phases. Moving down the y-axis deeper into pseudotime, we observe that the next primary cluster of transcription factors and functional annotations exhibited widespread enrichment across all of pseudotime. Furthermore, transcription factors enriched in this cluster are involved with basic cellular functions (e.g. euchromatin maintenance, transcription, growth) and are likely representative of normal WI-38 function in G1 phase.

Moving forward into the transition phase of pseudotime, we observed an enrichment of transcription factors regulating higher order chromatin structure (CTCF) and epigenetic silencing (poly-

bioRxiv preprint doi: https://doi.org/10.1101/2021.05.03.442497; this version posted November 12, 2021. The copyright holder for this preprint (which was not certified by peer review) is the author/funder. All rights reserved. No reuse allowed without permission.

comb group complex). Also in the transition region of pseudotime, the earliest enrichments appear for transcription factors related to EMT (SNAI2), TGF-β signaling (SMAD3), YAP1/TEAD1 activity, and the AP1 complex (JUN, FOS, FOSL2). We observed continued enrichment for these transcription factors and processes throughout the rest of the transition phase and into late pseudotime.

Lastly, late in pseudotime, we observed enrichment of transcription factors and functional annotations related to regulation of inflammatory processes (NFKB1, RELA, ERG1, CEBPB) and changes in cellular morphology (Figure 7D, Figure 7 supplement 2). These observations are consistent with observations made with bulk RNA-seq that replicative senescence WI-38 cells exhibit transcriptomic features similar to that observed in TGF-β signaling, EMT, and with YAP1/TEAD1 activity. Collectively, these results present a possible order of operations for replicative senescence progression that highlights an initial cessation of active mitotic cycling, followed by an epigenetic shift that precedes a strong EMT/TGF-β signal before segueing into a pro-inflammatory secretory state.

Replicatively senescent WI-38 fibroblasts express canonical myofibroblast markers and metabolic features

Given the repeated observations linking replicative senescence with EMT, (Figure 1, Figure 3), TGF-β and YAP1/TEAD1 activity (Figure 6, Figure 7), we considered the possibility that these processes are connected through the fibroblast to myofibroblast transition (FMT), a subtype of EMT in which stressed or injured fibroblasts differentiate into myofibroblasts (***Phan, 2008***; ***Piersma et al., 2015***; ***Hinz, 2007***). Upon receiving cues mediated by injury or stress (e.g. activated TGF-β), fibroblasts can trans-differentiate into myofibroblasts, whose functions as "professional repair cells" include increased proliferation, migration, apoptosis avoidance, cell and tissue contraction, and ECM/collagen deposition to promote tissue repair and wound closure (***Hinz and Lagares, 2020***; ***Gibb et al., 2020***).

Previous work has demonstrated that there exists mechanistic and functional association between telomerase inhibition, senescence, and myofibroblasts. Senescence is an integral part of the wound healing processes; upon injury resolution, activation of a senescence-like phenotype prevents unchecked collagen secretion and fibrosis by preventing myofibroblast proliferation and earmarking them for subsequent immune clearance (***Demaria et al., 2014***; ***Krizhanovsky et al., 2008***; ***Jun and Lau, 2010***; ***Mellone et al., 2016***; ***Razdan et al., 2018***; ***Liu et al., 2002***, ***2006***).

To further explore this proposition, we retrieved canonical myofibroblast marker genes and direct transcriptional targets of the YAP1/TEAD1 complex to determine to what extent these genes are expressed in WI-38 replicative senescence cells at both the RNA and protein level. First, we examined canonical myofibroblast markers (***Hinz and Lagares, 2020***), collagen produced by myofibroblasts (***Zhang et al., 1994***), genes upregulated in myofibroblasts derived from idiopathic pulmonary fibrosis patients (***Strunz et al., 2020***), and effectors and targets of TGF-β signaling in two data modalities: bulk RNA-seq and and bulk proteomics (Figure 8A).

For the majority of genes in the curated myofibroblast panel, expression increased with PDL. Importantly, expression of smooth-muscle actin (ACTA2), a classic myofibroblast marker, increases strongly in replicative senescence. The expression of follistatin-like protein (FSTL1), also known to be strongly expressed in smooth muscle, shows a similar pattern, as does fibrillin (FBN1). All three of these are associated with smooth muscle and TGF-β family regulation. In addition we observed an increase in both fibrillar and basal lamina collagens in our data at both the RNA and protein levels.

Collagen processing is a multi-step process requiring the coordination of multiple enzymes and metabolites (***Lodish and Zipursky, 2001***). Review of the collagen synthesis pathway alongside our metabolomic and proteomic data provide further confirmation that WI-38 replicative senescence cells exhibit altered collagen metabolism (Figure 8B). We observed up-regulation of multiple pathway enzymes as well as increased abundance of hydroxyproline, a primary constituent amino acid of collagen protein. In addition, we observe a striking depletion of ascorbate (vitamin C) which is

bioRxiv preprint doi: https://doi.org/10.1101/2021.05.03.442497; this version posted November 12, 2021. The copyright holder for this preprint (which was not certified by peer review) is the author/funder. All rights reserved. No reuse allowed without permission.

required for proline hydroxylation and is an essential vitamin. It is possible that our observations underestimate the collagen production potential of replicative senescent WI-38 cells as they appear limited in terms of collagen production by the amount of supplemented vitamin C (***Boyera et al., 1998***).

Mellone et al. (***2016***) recently reported that although senescent fibroblasts share features with myofibroblasts, this resemblance does not extend to fibrogenic ECM components, e.g. collagen (***Mellone et al., 2016***). However, it is important to note that ***Mellone et al.*** (***2016***) focused on radiation induced senescence rather than replicative senescence, and we similarly observed less or no induction of many of these same genes in our radiation induced senescence experiment. In addition, it is possible that with more time (> 10 days), fibrogenic ECM expression could initiate in the irradiation WI-38 cells.

Moving forward in our myofibroblast panel, we observed that expression of TGF-β cytokine, TGF-β1, decreased significantly with replicative senescence in both RNA and protein. However, we see robust induction of the TGF-β isotype 2 (TGF-β2) cytokine with replicative senescence (Figure 8A) as TGF-β1 abundance drops, which indicates a switch in TGF-β isotypes with replicative senescence. It has been shown TGF-β2 is a more potent inducer of the endothelial to mesenchymal transition (EndMT) *in vitro* compared to TGF-β1 and TGF-β3 in human microvascular endothelial cells, and TGF-β2 may be playing a similar role here in inducing FMT and replicative senescence in WI-38 cells (***Sabbineni et al., 2018***). The distinct functional roles of different TGF-β isotypes are largely unknown, although both are known to activate the SMAD transcription factors. On the basis of our data, it seems likely that the TGF-β paralog relevant here might not be TGF-β1, but TGF-β2.

Expression of YAP1/TEAD1 targets during RS

Next, we retrieved a gene set of YAP1/TEAD1 targets assembled by Kurrpa et al. from five separate studies (***Kurppa et al., 2020***). Taking the intersection of the five YAP1/TEAD1 gene target lists, we only kept genes present in at least 2 of the studies and plotted the remainder in Figure 8C across the three data types. We arranged the YAP1/TEAD1 targets by the two predominant expression patterns–decrease with replicative senescence (top) and increase with replicative senescence (bottom). As with myofibroblast markers, the data from both modalities is largely concordant.

Interestingly, we noted a striking bifurcation whereby YAP1 targets tend towards either strong down-regulation or strong up-regulation. The down regulated partition is heavily enriched for classic cell cycle regulated genes such as TOP2A, CDC20, BIRC5, and CDK9 suggesting that this dichotomy in YAP1 activity is heavily influenced by the cell cycle and consistent with recent work (***Kim et al., 2019b***; ***de Sousa et al., 2018***).

Excitingly, TGF-β2 was one of the two genes found in four out of five collected YAP1/TEAD1 gene sets, supporting the inference that the TGF-β2 and not TGF-β1 is the relevant paralog and potentially regulated by YAP1/TEAD1 in the replicative senescence context. In addition, another YAP1 target, thrombospondin-1 (THBS1), is also upregulated with RS; THBS1 is known to act as an activator of TGF-β signaling, and specifically TGF-β2, through proteolytic cleavage of latent TGF-β (***Ribeiro et al., 1999***).

Inhibiting the YAP1/TEAD1 interaction in WI-38 cells suppresses expression of YAP1/TEAD1 targets and the replicative senescence gene signature

In all, the data reveal that replicative senescence WI-38 cells share multiple defining transcriptomic and proteomic features with myofibroblasts. Furthermore, we found that a subset of YAP1/TEAD1 targets are both induced with RS, and are principal components of TGF-β signaling (TGF-β2, THBS1). Thus the YAP1/TEAD1 complex may be acting in convergence with TGF-β signaling with increasing PDL to enact a myofibroblast-like state that we recognize as replicative senescence.

Recently ***Mascharak et al.*** (***2021***) showed verteporfin treatment of wounds in mice alleviated the fibrotic state during wound healing, reverted the profibrotic transcriptional program, and reduced the myofibroblast population. Verteporfin is also known to be an inhibitor to the formation of the

bioRxiv preprint doi: https://doi.org/10.1101/2021.05.03.442497; this version posted November 12, 2021. The copyright holder for this preprint (which was not certified by peer review) is the author/funder. All rights reserved. No reuse allowed without permission.

YAP1/TEAD1 complex (***Wang et al., 2016***). To test for a direct role for YAP1/TEAD1 in transcriptional regulation of YAP target genes, myofibroblast marker expression and the EMT signature during replicative senescence transition, we treated late passage WI-38 PDL 40 cells with verteporfin or DMSO as an untreated control. We utilized RNA-seq to capture the gene expression changes on cells treated with verteporfin. First, to confirm the verteporfin treatment inhibited expression of canonical YAP target genes in WI-38 cells, we checked the expression of CTGF, CYR61, and TGFB2 (Figure 8 supplement 1A) (***Zhao et al., 2008***; ***Zhang et al., 2009***; ***Chen et al., 2001***). We found that treatment with 10 uM VP for 2 hours reduced expression of these three YAP target genes by 70% relative to the no treatment control (Figure 8 supplement 1A, Figure 8 source data 1). We expanded the analysis to the myofibroblast markers and YAP targets used in Figure 8 and observed that verteporfin treatment reduces the gene expression of most myofibroblast markers and collagen and many YAP1 target genes that were shown to increase with replicative senescence (Figure 8A, C).

We applied GSEA analysis using the MSigDB Hallmark annotation to understand what pathways are affected by verteporfin treatment of cells using the RNA-seq data from the verteporfin treated samples relative to non-treated control. Consistent with our hypothesis that YAP1/TEAD1 plays a role in regulating the FMT-like transition of cells undergoing replicative senescence, treatment of late passage cells with verteporfin resulted in negative enrichment of pathways relevant to FMT and TGF-β signaling (Figure 8 supplement 1B). We also took genes driving the Hallmarks EMT annotation enrichment in replicative senescence cells to see if inhibition of YAP1/TEAD1 complex formation aids in reducing EMT pathway gene expression. Compared to the no treatment control, the majority of genes induced during replicative senescence that drive the GSEA Hallmarks EMT enrichment have strikingly decreased in expression after 2 hrs of treatment. These data suggest that the use of verteporfin to inhibit the YAP1/TEAD1 interaction can impede the FMT-like transition observed in replicative senescent cells (Figure 8 supplement 1D).

To gain a global understanding of how inhibiting the YAP1/TEAD1 interaction affects the transcriptomic landscape of late passage WI-38 cells, we compared the gene expression signature of replicative senescence cells to that of verteporfin treated cells and found that verteporfin treatment globally reverses many of the gene expression changes occurring with replicative senescence (Figure 8 supplement 1C). This results suggest that YAP1/TEAD1 transcriptional activity is a crucial regulator of a large swath of the replicative senescence transcriptome.

Discussion

The study of replicative senescence in human tissue culture has proven to be an informative model for learning how genetic and environmental factors impact cellular senescence. However, the field has not fully taken advantage of the 'omics' revolution. Rekindled by the advent of senolytics, interest in the molecular underpinnings of senescence has burgeoned in recent years as researchers seek to design therapeutic strategies for ablating senescent cells (***Amor et al., 2020***; ***Elmore et al., 2018***; ***Wagner and Gil, 2020***; ***Aghajanian et al., 2019***). However, many such studies span only one or two systematic data modalities. Here, to fully leverage the power of recent advances in high-dimensional profiling, we revisit the original Hayflick limit in WI-38 lung fibroblasts cells with a battery of assays including RNA-seq, ATAC-seq, scRNA-seq, proteomics, and metabolomics in an effort to capture the defining features of replicative senescence at every step of the central dogma and beyond. Our results are summarized graphically in Figure 9.

One important feature of our study is the number and type of control conditions. From our pilot studies, it was clear that studying replicative senescence in isolation would preclude our ability to know what features of change were specific to replicative senescence versus high cell density and/or DNA damage induced growth arrest. Thus, we included cellular density as an alternate method for arresting growth and exposure to ionizing radiation as an alternate methodology for senescence induction and DNA damage response. Lastly, all of our modalities were paired with samples collected from an hTERT immortalized cell line grown in parallel. Importantly, very little

bioRxiv preprint doi: https://doi.org/10.1101/2021.05.03.442497; this version posted November 12, 2021. The copyright holder for this preprint (which was not certified by peer review) is the author/funder. All rights reserved. No reuse allowed without permission.

changed across all modalities in the hTERT cell line consistent with the changes we highlight in 9 as specific to replicative senescence.

The kinetics and precise timing of senescence onset have been obscured by low temporal resolution and ensemble measurements that cannot differentiate between global shifts in gene expression versus changing proportions of senescent cells (***Passos et al., 2007***; ***Xu et al., 2013***; ***Victorelli and Passos, 2017***; ***Smith and Whitney, 1980***; ***Tang et al., 2019***; ***Wiley et al., 2017***; ***Nassrally et al., 2019***; ***Whitney et al., 1980***). Here, with a combination of high time resolution and single cell RNA-seq, we provide evidence that the early manifestation of the senescent gene expression reflects gradual changes on a per cell basis rather than changing cell proportions. In effect, individual cells "show their age" with increasing PDL long before permanently exiting the cell cycle and transiting fully into the senescent state. The implications of this conclusion extend to organismal aging. For example, the percentage of senescent cells calculated from aging organisms varies greatly depending on the marker/phenotype used (***Ogrodnik, 2021***). The reported disparities could be explained in part by the use of early versus end stage markers. Likewise, it is possible the reported increase in fibroblast heterogeneity and altered functionality with age is a direct result of cells slowly moving along a spectrum towards replicative senescence (***Shin et al., 2020***; ***Mahmoudi et al., 2019***). Importantly, the gradual progression suggests that cells need not reach the endpoint to elicit a phenotype. For instance, proliferative fibroblasts isolated from IPF patients exhibited multiple senescent features and phenotypes in addition to accelerated senescence progression (***Yanai et al., 2015***). Lastly, this phenomenon is not constrained to fibroblasts as we observe that the salient regulatory features of replicative senescence extend to cell types as distant as astrocytes (Figure 6D).

In our data, the pattern of gene expression annotated to EMT as a unique feature of replicative senescence that consistently presents early and robustly at both the RNA, protein, and single cell level. Given the fundamental nature of the EMT transition with respect to cellular function (development, fibrosis, and wound healing), it is not surprising that this hallmark tracks with multiple proteins and gene sets suggesting drastic metabolic rewiring. In our metabolic data we highlight shifts in carbon and fatty acid utilization that have been reported previously as hallmark metabolic features of EMT. These metabolic changes demonstrate that our observations represent an authentic change in cellular state as opposed to a superficial uptick in a few EMT related genes.

The data presented above across multiple data modalities to provide a clear connection between senescent cells and myofibroblasts supported by independent observations at the level of DNA, RNA, protein, transcription factor activity and metabolism (Figure 9). In light of these, replicative senescence resembles a specialized subtype of EMT specific to the trans-differentiation of fibroblasts into myofibroblasts (FMT) in response to wound healing (***Lombardi et al., 2019***; ***Gibb et al., 2020***; ***Hinz and Lagares, 2020***). We hypothesize that during fibrotic disease states and/or age, fibroblasts migrate to sites of micro-injuries. As these proliferating fibroblasts become replicatively aged, they are triggered (by DNA damage or other insults) to rewire their metabolism to induce FMT via active epigenetic reorganization (NNMT-SAM/NAD sink). It is important to note here that the *in vitro* DNA damage here arises primarily from telomere erosion documented by the observation that our hTERT control cultures do not exhibit the same changes. However, genotoxic stress *in vivo* may originate from a variety of endogenous and environmental sources e.g. reactive oxygen species, replication stress, chemical exposure etc.

Following increases in DNA accessiblity, expression of newly opened TEAD1/YAP1/SMAD target genes cement FMT transition by promoting fibrosis and a myofibroblast-like, ECM-secreting state. This model is supported by the synergy between TEAD1 motifs and NAD domains we report and reconciles conflicting reports that YAP1/TEAD1 inhibition can both prevent and promote senescence (***Fu et al., 2019***; ***Kurppa et al., 2020***; ***Xie et al., 2013***; ***Jia et al., 2018***). Basically, the functional consequences of YAP1/TEAD1 inhibition will depend on the epigenetic organization of the cells used.

Further metabolic changes (hexoasmine/collagen synthesis and fatty acid oxidation) then support the new pro-fibrotic state. Finally, end point senescent cells reinforce the senescent state

bioRxiv preprint doi: https://doi.org/10.1101/2021.05.03.442497; this version posted November 12, 2021. The copyright holder for this preprint (which was not certified by peer review) is the author/funder. All rights reserved. No reuse allowed without permission.

and contribute to neighboring cell progression towards senescence via secretion of inflammatory factors and SASP.

We think that this transition is distinct from classic FMT as the endpoint cells are not proliferative, but instead bear striking resemblance to lingering senescent myofibroblasts that can persist long after wound repair is complete (***Hinz and Lagares, 2020***). Rather than a privileged or unique state, perhaps replicative senescence is better categorized as a DNA damage mediated path to a potentially common stress-induced endpoint.

The complex interplay between metabolism and epigenetic regulation preclude easy determination of a causal factor in translating DNA damage into the replicative senescence/EMT program in WI-38 cells. Does EMT regulate metabolism or vice versa? Here we present compelling evidence on the side of metabolism. We observe both an early and sharp rise in NNMT expression and activity in addition to a global increase in heterochromatin accessibility. These results are consistent with NNMT's reported role as global epigenetic regulator through its methylation sink activity (***Komatsu et al., 2018***; ***Eckert et al., 2019***; ***Pissios, 2017***; ***Ulanovskaya et al., 2013***).

Importantly, the observed shifts in repressed chromatin induced by NNMT are functional and may play a central role in fibroblast biology and stress response in multiple contexts. First, ***Eckert et al.*** (***2019***) recently demonstrated that NNMT activity and the resulting heteromchromatin reorganization initiate the expression program of cancer-associated fibroblasts (CAFs) associated with oncogenic stroma *in vivo* (***Eckert et al., 2019***). Similar to senescent fibroblasts and myofibroblasts, the defining features of CAFs are increased cytokine production, metabolic rewiring, and ECM alteration and production (***Sahai et al., 2020***). Second, NNMT is one the most up-regulated genes in a TGF-β mediated *in vitro* FMT conversion in WI-38 cells (***Walker et al., 2019***). Finally, the changes in silenced chromatin we observed during replicative senescence overlap with induction of gene expression driving the senescent phenotype (Figure 5D). In fact, pseudotime analysis argues that chromatin reorganization may precedes the FMT induction as evidenced by the loss of polycomb activity that appears prior to enrichment of the EMT and YAP1/TEAD1 transcription factors enrichments (Figure 7D).

The path to replicative senescence process has many *in vivo* parallels with implications for aging and pathogenesis. After observing induction in WI-38 cells of IPF myofibroblast markers (Fig. 8A), we expanded our literature search and found a striking overlap (TGF-β signaling, YAP1 activity, and EMT) between our data and scRNA-seq expression profiles from alveolar epithelial cells collected from IPF patients (***Xu et al., 2016***). These studies also report a large induction of TGF-β2 relative to TGF-β1 which is consistent with our findings and highlights a clear connection between *in vitro* replicative senescence and an *in vivo* disease state.

Another example of such a connection arises from our LISA analysis: one of the top enriched transcription factors, TCF21, has been implicated in atherosclerotic disease progression. Wirka et. al. found that TCF21 promotes the transition of vascular smooth muscle cells into a novel fibroblast-like cell type they dub "fibromyocytes" owing to their possession of both fibroblast and myocyte phenotypes in atherosclerotic lesions in both mice and humans (***Wirka et al., 2019***).

In general, the FMT hypothesis provides a conceptual framework and integrative model for linking the multi-modal senescent phenotypes we observed to multiple human age-related diseases. Given the observation that fibrosis and senescence markers correlate with increasing age in multiple tissues, it is possible that FMT might be a widespread phenomenon underlying many age-related pathologies (***Yousefzadeh et al., 2020***; ***Idda et al., 2020***). Future work harnessing multimodal single cell technology coupled with relevant *in vivo* models will aid greatly in determining the exact order of events and physiological import.

bioRxiv preprint doi: https://doi.org/10.1101/2021.05.03.442497; this version posted November 12, 2021. The copyright holder for this preprint (which was not certified by peer review) is the author/funder. All rights reserved. No reuse allowed without permission.

Table 1: Key Resources Table.

Reagent type	Designation	Source or reference	Identifiers	Additional info
Cell Line (H. sapiens)	WI-38 fibroblasts	Coriell	AG06814-N	
Cell Line (H. sapiens)	WI-38 hTERT	This paper		
Transfected construct	pCDH-CMV-hTERT-EF1a-puro	This paper	N/A	Lentiviral plasmid
Commercial assay	Senescence *beta*-Galactosidase	Cell Signaling Tech.	9860	
Commercial assay	MycoAlert Mycoplasma Detection	Lonza	LT07-218	
Commercial assay	Direct-zol RNA Miniprep Plus	Zymo Research	R2072	
Commercial assay	Chromium Single Cell 3' v2	10x Genomics	120237	
Commercial assay	Chromium Single Cell A Chip	10x Genomics	1000009	
Commercial assay	Tagment DNA Enzyme and Buffer	illumina	20034197	
Commercial assay	Clean and Concentrator-5	Zymo Research	D4014	
Commercial assay	NEBNext® High-Fidelity 2X PCR	NEB	M0541L	
Commercial assay	TruSeq Stranded mRNA Library	illumina	20020595	
Commercial assay	Bioanalyzer High Sensitivity DNA	Agilent	5067-4626	
Commercial assay	Pierce BCA Protein Assay	Thermo Fisher	23227	
Commercial antibody	Mouse anti-human p16 antibody	BD Biosciences	554079	
Commercial antibody	Mouse anti-human p21 antibody	BD Biosciences	556430	
Commercial assay	Pippin Prep 2% 100-600 bp	Sage Science	CDF2010	
Commercial Media	TrypLE Express Enzyme	Gibco	12604013	
Commercial Media	DMEM	Gibco	11885084	
Chemical compound	Verteporfin	RD Systems	1243926	
Other	Zorbax Extend C18 column	Aglient	759700-902	
Other	SeQuant ZIC-pHILIC column	EMD Millipore	150460	
Software, algorithm	R (v4.0.3 and 3.6.2)	r-project.org/	RRID:SCR_001905	
Software, algorithm	Salmon (v 0.8.2)	combine-lab.github.io/salmon/	RRID:SCR_017036	
Software, algorithm	DESeq2 (v1.30.1)	bioconductor	RRID:SCR_015687	
Software, algorithm	sva package(v3.38.0)	bioconductor	RRID:SCR_012836)	
Software, algorithm	fgsea 1.16.0	bioconductor	RRID:SCR_020938	
Software, algorithm	CellRanger 3.0	10x Genomics	RRID:SCR_017344	
Software, algorithm	SCTransform (v 0.3.2)	satijalab.org/seurat		
Software, algorithm	Seurat (v4.0.1.9005)	satijalab.org/seurat	RRID:SCR_007322	
Software, algorithm	monocle3 (v1.0.0)	cole-trapnell-lab.github.io/monocle3	RRID:SCR_018685	
Software, algorithm	bowtie2 (v2.3.4.1)	bowtie-bio.sourceforge.net	RRID:SCR_016368	
Software, algorithm	samtools (v1.2)	www.htslib.org	RRID:SCR_002105	
Software, algorithm	Picard (v2.6.4)	broadinstitute.github.io/picard	RRID:SCR_006525	
Software, algorithm	macs2 (v2 2.1.2)	hbctraining.github.io	RRID:SCR_013291	
Software, algorithm	GenomicRanges (v1.42.0)	bioconductor	RRID:SCR_000025	
Software, algorithm	cutadapt (v2.4)	github.com/marcelm/cutadapt	RRID:SCR_011841	
Software, algorithm	bcl2fastq (v2.20)	Illumina	RRID:SCR_015058)	
Software, algorithm	regioneR v1.22.0)	bioconductor		
Software, algorithm	ATACseqQC v1.14.4)	bioconductor		
Software, algorithm	LIMMA v3.46.0)	bioconductor	RRID:SCR_010943	
Software, algorithm	Qvalue v2.26.0)	combine-lab.github.io/salmonQvalue	RRID:SCR_001073	
Software, algorithm	LISA v1	lisa.cistrome.org		

bioRxiv preprint doi: https://doi.org/10.1101/2021.05.03.442497; this version posted November 12, 2021. The copyright holder for this preprint (which was not certified by peer review) is the author/funder. All rights reserved. No reuse allowed without permission.

Methods and Materials

Cell Culture

WI-38 maintenance and subculturing for replicative senescence time course-WT and hTERT

WI-38 cells were obtained from the Coriell Institute (AG06814-N) at PDL 15. The cells were grown in Dulbecco's modified Eagle's medium (DMEM, Gibco, 11885084) supplemented with 10% dialyzed fetal bovine serum (FBS, Sigma, F0392) and maintained in an incubator set to 37° C, 5% CO_2, and 20% O_2. 0.3-0.5 E6 WI-38 cells were seeded and maintained on 10 cm collagen coated plates (Corning, 354450) and split when cells reached about 70% confluence. For WI-38 cells PDL 15 tp PDL 40, it took about 4 days to reach 70% confluence. WI-38s >PDL 40 were slower growing, and therefore split every 5-7 days instead; media was replenished every 3-4 days (SText 1). Cells were passaged by washing the cell monolayer with PBS, followed by incubating cells with TrypLE Express (Gibco, 12604013) for 5 minutes. Media was added to neutralize the TrypLE and the cell suspension was collected into conical tubes. The cell suspension was spun at 200 x g for 5 minutes and the supernatant was aspirated. The resulting cell pellet was resuspended in media and cells were counted with viability measurements on a ViCell XR Cell Analyzer (Beckman Coulter). Cell numbers taken from the ViCell were used to calculate population doublings (PDLs). The following formula was used to calculate PDLs:

PDL = log2(number of cells harvested)−log2(number of cells seeded)

All cells collected for assays were sampled in triplicate, at 2.5-3 days after seeding, targeting 60-70% confluence to avoid the confounding effects of confluence. Confluence levels were determined with a phase contrast EVOS microscope (ThermoFisher). Slower growing cells (PDL > 40) were sampled at 3.5-4 days after seeding. Cells were tested every month for mycoplasma contamination using the MycoAlert Mycoplasma Detection Kit (Lonza). A smaller subset of three PDL timepoints (PDL 45, PDL 55, PDL 56) were generated in a secondary time course to ensure "deep" senescence (2-4 months after cell cycle cessation) was maintained as previously reported (***De Cecco et al., 2019***).

WI-38 hTERT cells were maintained using the same conditions as WT WI-38s, targeting 50-70% confluence for cell splitting and sampling alongside WT cells.

WI-38 irradiation time course

WI-38 cells at PDL 20 were plated in DMEM supplemented with 10% FBS with 50,000 cells per well in a 6-well collagen coated plate. Cells were allowed to settle and adhere to plates. All cells were adhered to the TC plate by 2 hours and were subsequently treated with 10 Gy of X-rays (Faxitron CellRad). Cells were sampled between 1 day and 9 days for transcriptome profiling. Each time point was sampled in triplicate. RNA was extracted according to methods below.

WI-38 cell density time course

0.3 E6 WI-38 cells at PDL 23 were seeded and grown on 10 cm collagen coated plates in DMEM supplemented with 10% FBS. Cells were grown and sampled intermittently between 1 day and 10 days for transcriptome profiling. Samples at each time point were taken in triplicate. RNA was extracted according to methods below.

SA-βGAL staining

Cells were stained for senescence associated beta-gal using the Senescence β-Galactosidase Staining Kit (Cell Signaling, 9860) by following the manufacturer's published protocols exactly.

WI-38 hTERT cells and lentiviral transduction

293T cells were transfected with a lentiviral target plasmid expressing hTERT (pCDH-CMV-hTERT-EF1a-puro) and lentiviral packaging constructs overnight; 48 hours later, viral supernatant was collected. WI-38 cells were transduced with viral supernatant in the presence of 5 μg/mL polybrene and selected for 7 days with 1 μg/ml of puromycin.

bioRxiv preprint doi: https://doi.org/10.1101/2021.05.03.442497; this version posted November 12, 2021. The copyright holder for this preprint (which was not certified by peer review) is the author/funder. All rights reserved. No reuse allowed without permission.

WI-38 + verteporfin treatment

200,000 WI-38 cells at PDL 38 were seeded onto each well of a 6-well collagen coated plate and grown with 2 ml of DMEM supplemented with 10% FBS. After 4 days of growth, cells were treated with 5 or 10 μM of verteporfin (RD Systems 5305/10) for 2 hours or DMSO. RNA was extracted after 2 hours of treatment according to methods described below.

Bulk RNA-seq methods

RNA collection and library preparation

Total RNA was extracted from cells using the Direct-zol RNA Miniprep Plus kit (Zymo Research R2072) for all bulk RNA-seq time course experiments and verteporfin treatment experiment. Manufacturer's protocol was followed exactly and in-column DNAase digestion was performed. RNA quality score and concentration was measured using the Fragment Analyzer (Agilent 5200) with the Fragment Analyzer Standard Sense RNA kit (Agilent Technologies DNF-471-0500). All samples required to have a RIN score of >7 for processing. RNA sequencing libraries were prepared as directed using TruSeq® Stranded mRNA Library Prep Kit (Illumina 20020595), with 1000ng of input material. Samples were amplified for 12 cycles of PCR with TruSeq RNA CD Index Plate (Illumina) and pooled. 3nM libraries were loaded across 4 lanes on the HiSeq 4000 (Illumina).

Read processing and quantification

Reads generated from the Illumina HiSeq 4000 were demultiplexed with bcl2fastq (version=2.20) based on the barcode sequence of each sample. Average read depth across samples was 50 million paired-end reads. Reads were pseudo-aligned and quantified using Salmon (version=0.8.2) by deploying the mapping based mode using a Salmon command "index" with default parameters based on 10X genomics hg38 transcriptome annotations optimized for single cell RNA-seq ("refdata-cellranger-GRCh38-3.0.0", cellRanger version 3) to ensure accurate comparison between bulk and single cell RNA-seq (***Patro et al., 2017***). Annotations can be obtained running "wget https://cf.10xgenomics.com/supp/cell-exp/refdata-cellranger-GRCh38-3.0.0.tar.gz"

Differential expression analysis

DESeq2 (version=1.30.1) was used for differential analysis of the RNA-seq data ***Love et al.*** (***2014***). Wald test was used to estimate fold change and significance using the model: ~time + batch, where time is a numeric variable representing the fraction of time course complete and batch is a categorical variable used only with replicative senescence with the addition of the "deep" senescence time points. DEGs were defined as having FDR adjusted p-values < 0.01.

Batch correction and hierarchical clustering

For clustering and visualization we corrected the raw replicative senescence count table by batch before converting to transcripts per million (TPM) with a +1 pseudocount and combining with radiation induced senescence and cell density samples using Combat-seq (sva R package version=3.38.0) (***Zhang et al., 2020***). Significant genes from each condition were concatenated to generate a universe of significant change genes used for Figure 1. Each sample was then converted to log2 fold change vs. the mean of the initial time point.

Gene set enrichment analysis

For gene set enrichment analysis, we downloaded the MSigDB Hallmark gene sets from misgDB website (version 7, gene symbols) ***Liberzon et al.*** (***2015***). For each time course (replicative senescence, radiation induced senescence, and cell density) we we ranked all genes by the log2 fold change across time generated by DESeq2. Then GSEA was performed on the ranked gene set using the R package "fgsea" version 1.16.0 which is an implementation of GSEA in R (***Subramanian et al., 2005***; ***Korotkevich et al., 2019***; ***Mootha et al., 2003***). By default, GSEA tests for enrichment of each gene set in each condition in both directions. We report the -log10 Benjamini-Hochberg

bioRxiv preprint doi: https://doi.org/10.1101/2021.05.03.442497; this version posted November 12, 2021. The copyright holder for this preprint (which was not certified by peer review) is the author/funder. All rights reserved. No reuse allowed without permission.

corrected p-value in Figure 1 and use the normalized enrichment score (NES) to assign direction of the change.

Single Cell 3' RNASeq Methods

Cell collection

At each time point, singlet hTERT controls and experimental samples were processed with Chromium Single Cell 3' RNAseq kit V2 (10x Genomics 120237) through cDNA amplification cleanup, where they were frozen at -20°C. Once all time points were converted to cDNA, the frozen cDNAs were thawed and batched for library construction. The following modifications were made to the process: Reverse transcription reactions were brought up to volume with DMEM + 10% FBS instead of water, each emulsion targeted 3000 cells (5200 cells loaded), and cDNA was amplified 12 cycles, with 12 cycles of index PCR. There was no hTERT control for time point 3, and one of the replicates for PDL 25 dropped out during library construction. Remaining samples were pooled at equimolar concentration and sequenced on a HiSeq4000 with the standard 26,8,0,98 run base pairs per read configuration.

Single cell data processing, normalization, scoring, clustering and DEG analysis

The raw single cell reads were demultiplexed by sample using bcl2fastq. Alignment, cell barcode demultiplexing, transcript quantification and sample merging were carried out with CellRanger 3.0 using the hg38 CellRanger 3.0 gene annotation ("refdata-cellranger-GRCh38-3.0.0", cellRanger) with default options and parameters. Filtered cell by gene matrices were normalized using Seurat (version = 4.0.1.9005) and SCTransform (version = 0.3.2) (***Hafemeister and Satija, 2019***; ***Stuart et al., 2019***). Dimension reductionality was carried out with PCA (n = 50). Clusters were defined using the louvain algorithm resolution= and cells were visualized with UMAP projection ***McInnes et al.*** (***2018***); ***Becht et al.*** (***2019***); ***Blondel et al.*** (***2008***). For cell cycle scoring and phase determination as well as senescence scoring we applied the Seurat implementation of the scoring function as previously described (***Nestorowa et al., 2016***).

DESeq2 was used for differential gene expression analysis to identify significantly changing genes within individual clusters as a function of increasing PDL (PDL by mitotic phase) (Fig. 3D) using a an input matrix of gene counts by cells per PDL by mitotic phase. Gene counts were summarized across cells for each mitotic phase (PDL 50 removed). To expedite computation, we restricted analysis to highest expressed 8,000 genes. For each PDL by cell cycle phase grouping, we required that >15 representative cells must exist to be considered in analysis. To visualize differentially expressed genes, we converted single cell counts to counts per million (+1 pseudocount) and averaged across PDL by cell cycle phase and calculated the log2 fold change at each PDL by cell cycle phase against the earliest PDL for that cell cycle phase using a concatenated list of all significantly changing genes generated by DESeq2 from each cell cycle phase.

Pseudotime analysis

For pseudotime analysis of the single cell data, we used the R package monocle3 (version=1.0.0) which implements PCA, Leiden clustering, and UMAP prior to partitioning and trajectory analysis. We first isolated WT cells by removing hTERT cells and those not belonging to the primary grouping. To focus trajectory analysis on the replicative senescence progression, we used only the top genes found to significantly change with replicative senescence in bulk RNA-seq for PCA (padj < 0.01) and log2 fold change > 3 or log2 fold change < -3). In applying the Monocle trajectory analysis: (learn_graph(cds,close_loop = FALSE,learn_graph_control = list(minimal_branch_len = 35, geodesic_distance_ratio = .5, euclidean_distance_ratio=1), we designated cycling cells at the opposite end of UMAP project from the senescent cells as the start point manually. (***Trapnell et al., 2014***; ***Qiu et al., 2017***; ***Cao et al., 2019***; ***Traag et al., 2019***; ***Levine et al., 2015***; ***McInnes et al., 2018***). After establishing a trajectory, we then employed the Monocle3 "graph test" function to isolate genes that significantly change as a function of pseudotime. Pseudotime estimation was output

bioRxiv preprint doi: https://doi.org/10.1101/2021.05.03.442497; this version posted November 12, 2021. The copyright holder for this preprint (which was not certified by peer review) is the author/funder. All rights reserved. No reuse allowed without permission.

from monocle3 using the learn graph function for building a trajectory. Smoothed pseudotime trajectories use for Figure 7C were calculated for significantly changing genes (with pseudotime) by binning cells across pseudotime into 60 bins and using a cubic spline to estimate expression at each bin. For each gene, the smoothed trajectory was set from 0 (minimal) to (1) maximal expression. Genes were organized with K-median clustering (k=25) using cosine similarity. For visualization the median expression value for each pseudotime bin and cluster was calculated. Genes from each cluster were fed into LISA TF analysis (below)

ATAC-SEQ methods

ATAC-seq Library Preparation and Sequencing

Freshly harvested cells were used for all reactions. Briefly, the cell monolayer was washed with PBS, trypsinized with TrypLE Express (Gibco 12604013), resuspended in media, and cells were pelleted. Cells were counted and 100,000 cells were used in each reaction. Cell lysis, DNA transposition, and library construction was followed from the Omni-ATAC protocol (Corces et al. 2017). Libraries were amplified for 13 total cycles. Sample purification and size selection were performed on the Pippin high throughput size selection platform using 2% agarose cassettes to isolate fragments < 300 base pairs (Sage Science). Quality of ATAC-seq libraries were assessed with the Agilent Bioanalyzer 2100 with DNA high sensitivity chips (Agilent Technologies 5067-4626). Libraries were sequenced on the HiSeq4000 with paired end sequencing using 2 x 150 bp reads (Illumina).

ATAC-seq data processing, peak calling, and differential accessibility

We first trimmed the raw fastq files with cutadapt (version=2.4) to remove standard Nextera PE adapters:

adapt -a file:$ADAPTER -A file:$ADAPTER -o $SAMPLE.R1.fq -p $SAMPLE.R2.fq –pair-filter=any –minimum-length=30 $R1 $R2

Then we aligned with bowtie2 (version version 2.3.4.1) to align the trimmed reads to hg38: bowtie2 -x $INDEX -1 $SAMPLE.R1.fq -2 $SAMPLE.R2.fq –no-mixed –no-discordant -X 1000

After alignment, we used samtools (version=1.2) flags (-f 0x02 and -q2 0) to filter for only properly paired and high quality reads. PCR duplicates are removed using picard (version=2.6.4) MarkDuplicates. Finally for each bam file, we adjusted the reads ends by Tn5 offset (+4 on + strand, -5 on -strand).

ATAC-seq QC (mitochondrial percent and transcription start site score) and alignment metrics were generated with R package ATACseqQC (version=1.14.4) and multiQC respectively (version=1.11) (***Ewels et al., 2016***) using TxDb.Hsapiens.UCSC.hg38.knownGene (version = 3.10.0) annotations for transcription start site score calculation.

For peak calling, we created a condition specific peak atlas by pooling all replicates in a specific condition and applied macs2 (version = 2 2.1.2) for peak calling on the pooled bam file with options (-g hs -p 1e-1 –nomodel –shift -37 –extsize 73). In addition, we performed peak calling on each individual replicates as well. Then we performed irreproducible discovery rate analysis on each condition specific peak atlas for each pair of replicates and filter for peaks that are reproducible in at least two replicates (IDR threshold of 0.05). A single accessibility atlas is created by merging condition-specific peak atlas across all conditions (Figure 5 source data 3). Peaks were assigned to nearest gene if it is within 50kb, otherwise it is annotated as intergenic.

Read count was performed using countOverlaps function from R package GenomicRanges (version = 1.42.0) (***Lawrence et al., 2013***). We performed quantile normalization of the count matrix using normalize.quantiles function of R package preprocessCore (version=1.52.1).

Limma-voom (Limma version = 3.46.0) was used for differential accessibility analysis (***Ritchie et al., 2015***). Fold change and fdr adjusted p-values were estimated using moderated t-test statistic based on the model: time + condition + time:condition. We performed separate tests for time point 1 versus each of the other time points.

bioRxiv preprint doi: https://doi.org/10.1101/2021.05.03.442497; this version posted November 12, 2021. The copyright holder for this preprint (which was not certified by peer review) is the author/funder. All rights reserved. No reuse allowed without permission.

ATAC-seq chromatin state and NAD/LAD analysis

To quantify ATAC-seq reads in chromatin states we retrieved hg38 ENCODE IMR-90 chromatin state labels from (***Ernst and Kellis, 2015***) (Figure 5 source data 1). Next we quantified coverage for each instance of all 25 chromatin states genome wide using countOverlaps function from R package GenomicRanges (***Lawrence et al., 2013***). We performed quantile normalization of the chromatin state count matrix using normalize.quantiles function of R package preprocessCore (Fig. 5A).

ATAC-seq peaks were assigned to chromatin states using the findOverlapsOfPeaks function from the R package GenomicRanges (***Lawrence et al., 2013***). We used only significantly ($p < 0.001$) changing peaks(with senescence) from LIMMA-voom analysis. To simplify the overlap of these two sets of genomic intervals, we took only peaks that fell within ("inside") or encompassed a chromatin state annotation ("inside feature"). Peaks encompassing more than one chromatin state interval were discarded (Fig. 5A,B).

For analysis of NAD and LAD domain overlap we collected IMR-90 NAD labels from (***Dillinger et al., 2017***) and IMR-90 LAD labels from (***Sadaie et al., 2013***) (Figure 5 source data 5 and 6). For calculating overlap Z-score between genomic intervals sets (e.g. NADs/LADs vs gene annotation (TxDb.Hsapiens.UCSC.hg38.knownGene, version = 3.10.0) for Figure S18C we used the overlapPermTest function from the R package regioneR (version = 1.22.0) ***Gel et al.*** (***2016***).

For testing overlaps between NAD/LAD domains and significantly changing genes, we used the overlapPermTest function from the regioneR package using the top induced genes from each bulk RNA-seq condition (RS,RIS, and CD) against a universe of all genes sampled from the same expression distribution to control NAD and LAD bias across different levels of expression. For gene annotations we used TxDb.Hsapiens.UCSC.hg38.knownGene (version = 3.10.0).

Metabolomics

Extraction of water-soluble metabolites from lung fibroblast cell culture

Twenty-four hours before metabolite extraction, the medium was aspirated, cells were washed with unconditioned medium and then the medium was replaced. For metabolite extraction, cells were washed once in 37°C warm PBS-buffer immediately followed by the addition of 3.5 mL of freezer-cooled ($-20\,°C$) LC-MS grade 80:20 MeOH/H_2O (Sigma Aldrich). The plates were then held at $-20\,°C$ for 2 hours, then harvested with a sterile cell scraper while at -20°C and transferred to $-20\,°C$ cold 5 mL centrifuge tubes (Eppendorf Lo-Bind). After centrifuging the cell-extracts in a $4\,°C$ centrifuge for 5 min at 2000 x g, the supernatants were transferred into new cold centrifuge tubes and dried under nitrogen at $4\,°C$. Dried extracts were stored at $-20\,°C$.

LC-MS/MS analysis of cell culture extracts

Dried supernatants were resuspended in 200 µL of water containing 1 µg/mL of deuterated lysine and deuterated phenylalanine and 250 ng/mL of deuterated succinate (Sigma Aldrich) as internal standards. For negative ion mode, the resuspended samples were diluted 1:4 in water, for positive ion mode, they were diluted 1:4 in acetonitrile. Samples were then centrifuged at 18000 x g for 5 minutes, the supernatant was moved to HPLC vials and 5 µL was injected for analysis by LC-MS on Vanquish UPLCs (Thermo Scientific) coupled to Q Exactive Plus mass spectrometers (Thermo Scientific).

For analysis in negative ion mode, separation of compounds was achieved by reverse-phase liquid chromatography on a Zorbax Extend C18 column (150 x 2.1 mm, 1.8 µm particle size (Agilent 759700-902). Mobile phase A was 10 mM Tributylamine and 15 mM Acetic Acid in 97:3 water:methanol at pH 4.95 and mobile phase B was methanol. Prior to injection, the column was equilibrated in 0% B for 4 minutes. The gradient eluted isocratically in 0% B for 2.5 minutes, increased to 20% B over 2.5 min, held at 20% B for 2.5 min, increased to 55% B over 5.5 min, increased to 95% B over 2.5 minutes, maintained at 95% B for 3 min, then decreased to 0% B over 0.5 min, where it was held for 3 min, resulting in a total run time of 26 min. The LC separation was carried out at $30\,°C$ column temperature using a 200 µL/min flow rate. For MS-analysis, parameters on

bioRxiv preprint doi: https://doi.org/10.1101/2021.05.03.442497; this version posted November 12, 2021. The copyright holder for this preprint (which was not certified by peer review) is the author/funder. All rights reserved. No reuse allowed without permission.

MS1 were set to 70,000 resolution with an AGC target of 1e6 at a maximum IT of 100 ms. The scan range was 70 to 1050 m/z. MS2 parameters were set to 17,500 resolution at loop count 6, an AGC target of 1e5 at a maximum IT of 50 ms, an isolation window of 1 m/z and an underfill ratio of 1%. Dynamic exclusion was set at 20s with an apex trigger from 3 to 12s. Stepped collision energies were set to 20, 50 and 100% NCE.

For analysis in positive ion mode, compounds were separated via hydrophilic liquid interaction chromatography (HILIC), using a SeQuant ZIC-pHILIC column (150 x 2.1 mm, 5 µm particle size) Millipore (150460). Mobile phase A consisted of 20 mM ammonium bicarbonate at pH 9.2 in H2O, and mobile phase B was acetonitrile. Prior to injection, the column was equilibrated for 6 minutes in 80% B. The gradient then decreased to 20% B over 20 min, then to 15% B over 2 min, returned to 80% B over 0.5 min and held there for 1.5 min for a total run time of 30 min. The column temperature was $35\,°\mathrm{C}$ with a flow rate of 150 µL/min. For MS-analysis the MS1 parameters were as described for negative ion mode except the AGC target was 3e6. MS2 parameters were the same with following exceptions: dynamic exclusion was set to 25s with an apex trigger from 3 to 10s. Stepped collision energies were set to 20, 40 and 80% NCE.

Metabolomics batch correction and differential analysis

Protein lysates derived from same plates used for metabolomics collection were assayed for total protein concentration with Pierce BCA Protein Assay Kit (ThermoFisher 23225) for normalizing raw metabolite values. The median protein concentration for each PDL and PDL.ctrl was calculated and divided by the median protein concentration across all samples for either cell line (WT and hTERT) to derive a protein concentration normalization factor. The raw metabolite values for each PDL and hTERT PDL.ctrl were multiplied by the protein concentration normalization factor for that strain and sample. Protein normalized metabolite values were then converted to log2 fold change values using the first time point as a reference (Figure 3 source data 2). To remove sample day batch effects, we took the protein normalized metabolite values and divide each WT metabolite value by the corresponding metabolite value in the temporally paired hTERT sample (e.g. PDL 25 values were divided by PDL 25.ctrl values) and converted to log2 fold change with first sample as reference.

Finally, the normalized log2 ratios were fit to a linear model to test for a linear trend across the time course. For each metabolite, we fit the model $y_{it}=\beta_0+\beta_1 T_t+\epsilon_{it}$, where $i=(1,...,3)$ indexes the replicates for each time point and $t=(1,...,4)$ indexes the cell passage vector $T=(33,37,46,50)$.

The model was fit with the lm() function in R Version 4.1.2. P-values from the two-sided hypothesis test $H_0 : \beta_1=0$ were FDR adjusted (across all proteins) using the qvalue function from the qvalue R package (version =2.26.0). If present, asterisks in figures indicate that the FDR adjusted p-value from this test was $< .05$.

Proteomics methods

Materials and sample preparation, extraction and digestion

LC-MS grade organic solvents, water, and tandem mass tag (TMT) isobaric reagents were purchased from Thermo Fisher Scientific (Waltham, MA). Trypsin was ordered from Promega Corporation (Madison, WI) and Lys-C from Wako Chemicals USA (Richmond, VA). Sep-Pak C18 cartridges were from Waters Corporation (Milford, MA). Unless otherwise stated, all other chemicals were purchased from Sigma-Aldrich (St. Louis, MO).

At time of sample collection, cells were trypsinized off the monolayer with TrypLE Express and media was used to neutralize the reaction. Cells were pelleted at 200 x g for 5 minutes and the supernatant was aspirated. Cell pellets were flash frozen in liquid nitrogen and stored at -80C until all samples were collected and ready for proteomics analysis. Cell pellets were resuspended in 450 µL of lysis buffer (75mM NaCl, 3% SDS, 50 mM HEPES, pH 8.5) and lysed by passage through a BD PrecisionGlide 21-gauge needle (20X). The lysate was sonicated for 5 minutes and then centrifuged (5 min, 16,000 x g) to remove cellular debris and the supernatant was collected.

bioRxiv preprint doi: https://doi.org/10.1101/2021.05.03.442497; this version posted November 12, 2021. The copyright holder for this preprint (which was not certified by peer review) is the author/funder. All rights reserved. No reuse allowed without permission.

Proteins were reduced with 5 mM dithiothreitol (DTT) for 30 minutes at 56 °C with shaking. Proteins were then alkylated with 15 mM iodoacetamide (IAM) for 30 minutes at room temperature (RT) in the dark, and excess IAM was quenched with 5 mM DTT for 20 minutes at RT in the dark. Protein purification was accomplished using a methanol-chloroform precipitation. Briefly, 800 µL methanol, 200 µL chloroform and 600 µL water were sequentially added to 200 µL of cell lysate, with 5 second intervals of vortexing between each addition. The samples were centrifuged for 30 minutes (16,000 x g at 4°C) to induce phase separation and both the top and bottom layers were removed. The precipitated protein pellet was washed with 600 µL methanol, vortexed briefly, then centrifuged for 10 minutes (16,000 x g at 4 °C). The methanol layer was removed and protein pellets were dried at RT for 10 minutes. Protein pellets were resuspended in digestion buffer (8 M urea, 50 mM HEPES, pH 8.5). The urea concentration was diluted to 4 M, then proteins were digested with Lys-C overnight (10 ng/µL, 25 °C, 16 h). The urea concentration was further diluted to 1 M and samples were digested with trypsin (5 ng/µL) for 6 hours at 37 °C.

Following digestion, peptides were acidified with trifluoroacetic acid (TFA) to a final concentration of 0.5% TFA. Peptides were desalted using Sep-Pak C18 solid-phase extraction (SPE) columns and samples were eluted sequentially, first with 40% acetonitrile (ACN)/0.5% acetic acid and then 80% ACN/0.5% acetic acid. Eluted peptides were dried in a CentriVap Benchtop Vacuum Concentrator (Labconco, Kansas City, MO) running at 30 °C. Peptide concentrations were measured using the Pierce BCA Protein Assay Kit, then 50 µg aliquots of each samples were dried in the CentriVap for further processing.

Tandem mass tag (TMT) labeling

Dried peptides were resuspended in 50 µL 200 mM HEPES/30% anhydrous ACN, then 200 µg of each TMT tag was added to 50 µg peptides. TMT 131c was used as the 'bridge sample' while the other tags (126, 127n, 127c, 128n, 128c, 129n, 129c, 130n, 130c, 131n) were used to label the individual samples. The TMT reaction was incubated for 1 hour at room temperature with gentle shaking, then quenched with 11 µL 5% hydroxylamine/200mM HEPES. All samples were acidified to a final concentration of 0.5% TFA. A small amount (4 µL) of each labeled sample was combined and desalted using StageTips to check TMT ratios and labeling efficiency. The TMT-labeled samples were then combined at a 1:1:1:1:1:1:1:1:1:1:1 peptide ratio into 11-plex samples (***Rappsilber et al., 2007***). The combined samples were desalted using Sep-Pak C18 cartridges and dried under vacuum.

High pH Reversed-Phase (HPRP) fractionation

The pooled TMT-labeled peptides were fractionated using high pH reversed-phase liquid chromatography on an Agilent 1260 Infinity HPLC equipped with a diode array detector set at 215, 220 and 254 nm wavelengths (Agilent Technologies, Santa Clara, CA). Peptides were separated on an Agilent ZORBAX Extend-C18 column (4.6 mm x 250 mm, 5 µm particle size) running at 500 µl/min at 25°C. Peptides were eluted with a gradient with initial starting condition of 100% buffer A (5% ACN, 10 mM ammonium bicarbonate) and 0% buffer B (95% ACN, 10 mM ammonium bicarbonate). Buffer B was increased to 35% over 60 minutes, then ramped up to 100% B in 6 seconds where it was held for 5 minutes. Buffer B was then decreased to 0% over 6 seconds and held for 10 minutes to re-equilibrate the column to original conditions. The samples were fractionated into 96 fractions, then pooled into 12 fractions as previously described (***Huttlin et al., 2010***). The fractions were dried under vacuum and resuspended in 5% ACN/5% formic acid (FA) for LC-MS/MS analysis.

Proteomics Data Acquisition and Analysis

LC-MS/MS Data Acquisition All samples were analyzed by an Orbitrap Fusion Lumos Tribrid mass spectrometer coupled to an EASY-nLC 1200 (Thermo Fisher Scientific). Peptides were separated using a microcapillary column (100 µm x 250 mm long, filled in-house with Maccel C18 AQ resin, 1.8 µm, 120 Å; Sepax Technologies, Newark, DE) operating at 60 °C with a flow rate of 300 nL/min. Pep-

bioRxiv preprint doi: https://doi.org/10.1101/2021.05.03.442497; this version posted November 12, 2021. The copyright holder for this preprint (which was not certified by peer review) is the author/funder. All rights reserved. No reuse allowed without permission.

tides were eluted into the mass spectrometer using a 180 min method, with acetonitrile increasing from 6 to 30% over a 165 min linear gradient in 0.125% formic acid. Mass spectrometry data was collected in data-dependent acquisition (DDA) mode. A high resolution MS1 scan (500-1200 m/z range, 60,000 resolution, AGC 5 x 105, 100 ms max. injection time, RF for S-lens 30) was collected in the Orbitrap, and the top 10 precursors were selected for MS2 and MS3 analysis. Ions were isolated using a 0.5 m/z window for MS2 spectra. The MS2 scan was performed in the quadrupole ion trap (CID, AGC 1 x 104, 30% normalized collision energy, 35 ms max. injection time) and the MS3 scan was analyzed in the Orbitrap (HCD, 60,000 resolution, max. AGC 5 x 104, 250 ms max. injection time, 50% normalized collision energy). The max. cycle time was set at 5 s. For TMT reporter ion quantification, up to 6 fragment ions from each MS2 spectra were selected for MS3 analysis using synchronous precursor selection (SPS).

Proteomics data analysis

The ***Ting et al.*** (***2011***) software pipeline and methods developed in the the Haas and Gygi labs was used to process all proteomics data (***Ting et al., 2011***). Raw files were converted to mzXML files and searched against a composite human UniProt database containing forward and reverse sequences using the Sequest algorithm. MS/MS spectra were matched with fully tryptic peptides from this composite dataset using a precursor ion tolerance of 20 ppm and a product ion tolerance of 0.6 Da. TMT modification of peptide N-termini and lysine residues (+229.162932 Da) and carbamidomethylation of cysteine residues (+57.02146 Da) were set as static modifications. Oxidation of methionine residues (+15.99492 Da) was set as a variable modification. Peptide spectral matches were filtered to a 1% false discovery rate (FDR) using linear discriminant analysis (LDA) as previously described (***Ting et al., 2011***). Non-unique peptides that matched to multiple proteins were assigned to proteins that contained the largest number of matched redundant peptides sequences using the principle of Occam's razor (***Ting et al., 2011***).

Quantification of TMT reporter ion intensities was performed by extracting the most intense ion within a 0.003 m/z window at the predicted m/z value for each reporter ion. TMT spectra were used for quantification when the sum of the signal-to-noise for all the reporter ions was greater than 200 and the isolation specificity was greater than 0.75.

Peptide level intensities were converted to log2 ratios by dividing each scan by the intensity in the bridge channel. Relative protein abundance, for each sample, was estimated with the posterior mean from a previously described Bayesian model using methods as described by ***O'Brien et al.*** (***2018***) with code located at https://github.com/ColtoCaro/compositionalMS.

Finally, the relative abundance estimates were fit to a linear model to test for a linear trend across the passages as described by ***Gaun et al.*** (***2021***). For each protein, we fit the model $y_{it}=\beta_0 + \beta_1 T_t + \epsilon_{it}$, where $i=(1,...,3)$ indexes the three replicates for each time point and $t=(1,...,7)$ indexes the cell passage vector $T=(18, 25, 32, 33, 37, 46, 50)$.

The model was fit with the lm() function in R Version 3.6.0. P-values from the two-sided hypothesis test $H_0 : \beta_1=0$ were FDR adjusted (across all proteins) using the p.adjust() function. If present, asterisks in all figures indicate that the FDR adjusted p-value from this test was $< .01$.

Regulatory analysis

LISA TF analysis

Identification of putative regulators of the gene expression changes observed in the bulk RNA-seq experiments and the pseudotime analysis was carried out using (***Qin et al., 2020***); a recent algorithm built to leverage the vast amount of protein-DNA interactions catalogued via ENCODE. We used the GUI hosted at http://lisa.cistrome.org/ to enter lists of genes derived from K-medians pseudotime clustering clustering. The online GUI has a max input of 500 genes. Accordingly, for clusters containing >500 genes, each gene was ranked by correlation with the cluster median and the top 500 genes were used. LISA output consists of a ranked file of transcription factors and chromatin modifiers with enrichment p-values associated with specific ENCODE experiments. Given

bioRxiv preprint doi: https://doi.org/10.1101/2021.05.03.442497; this version posted November 12, 2021. The copyright holder for this preprint (which was not certified by peer review) is the author/funder. All rights reserved. No reuse allowed without permission.

that the calculated p-values were derived from gene sets of different sizes and from different number of supporting experiments, we used the ranks as the input parameter for the LISA analysis shown in Figures 6D and 7D. A universe of top factors across clusters was compiled by concatenating the top 5 TFs from each individual LISA output. The rank matrix was then centered across clusters to identify TFs with the highest rank in specific clusters.

ATAC-seq peak motif enrichment

We built a binary peak-by-motif matrix where each row is a binary vector representing the presence of 405 motifs we used from CisBP (Catalog of Inferred Sequence Binding Preferences) which is a freely available online database of transcription factor (TF) binding specificities: http://cisbp.ccbr.utoronto.ca (***Weirauch et al., 2014***). We only used motifs for TFs with measurable RNA-seq in WI-38 cells. In order to characterize transcription factor activity changes during senescence, we implemented both a gene-centric and a gene-indepedent approach.

In the gene-centric approach, we tested enrichment of each of the 405 motifs in peaks that are 1) associated with a gene set of interest (within 50kb), and 2) significantly associated with senescence (adjusted p-value < 0.001 in PDL 50 vs PDL 20) as compared to all the other peaks using binomial test.

Alternatively, we trained a ridge logistic regression model using the binary motif matrix as features to distinguish peaks of significantly increased accessibility during senescence from peaks of significantly reduced accessibility in PDL 50 vs PDL 20. A model trained on two thirds of the data distinguishes the two sets of peaks with AUC=0.67 on held-out peaks. We then trained 10 independent models using all the data to evaluate the coefficients to identify features (motifs) that are most predictive of senescence.

Acknowledgements

The authors would like to thank Ari Firestone, Jason Rogers, Nick Bernstein, Jeff Settleman, Rochelle Buffenstein, Emily Stoops, Magdalena Preciado, and Antoine Roux for their feedback on the experiments, analysis and the manuscript. In addition the authors would also like to thank Leonard Hayflick for guidance and discussion.

Author Contributions

MR, DB, ADL, and RC conceived the project. MC and DGH planned the experiment. MC, RW, AI, JG, LC, TM, and TV performed the experiments. DGH led the data analysis. DGH, HY, IS, and JO performed data analysis. DGH, MC, DB and DRK wrote and edited the manuscript. MR, DB, ADL, RC, AF, CK, BB, FM, DRK, DGH provided support and oversight for the project.

bioRxiv preprint doi: https://doi.org/10.1101/2021.05.03.442497; this version posted November 12, 2021. The copyright holder for this preprint (which was not certified by peer review) is the author/funder. All rights reserved. No reuse allowed without permission.

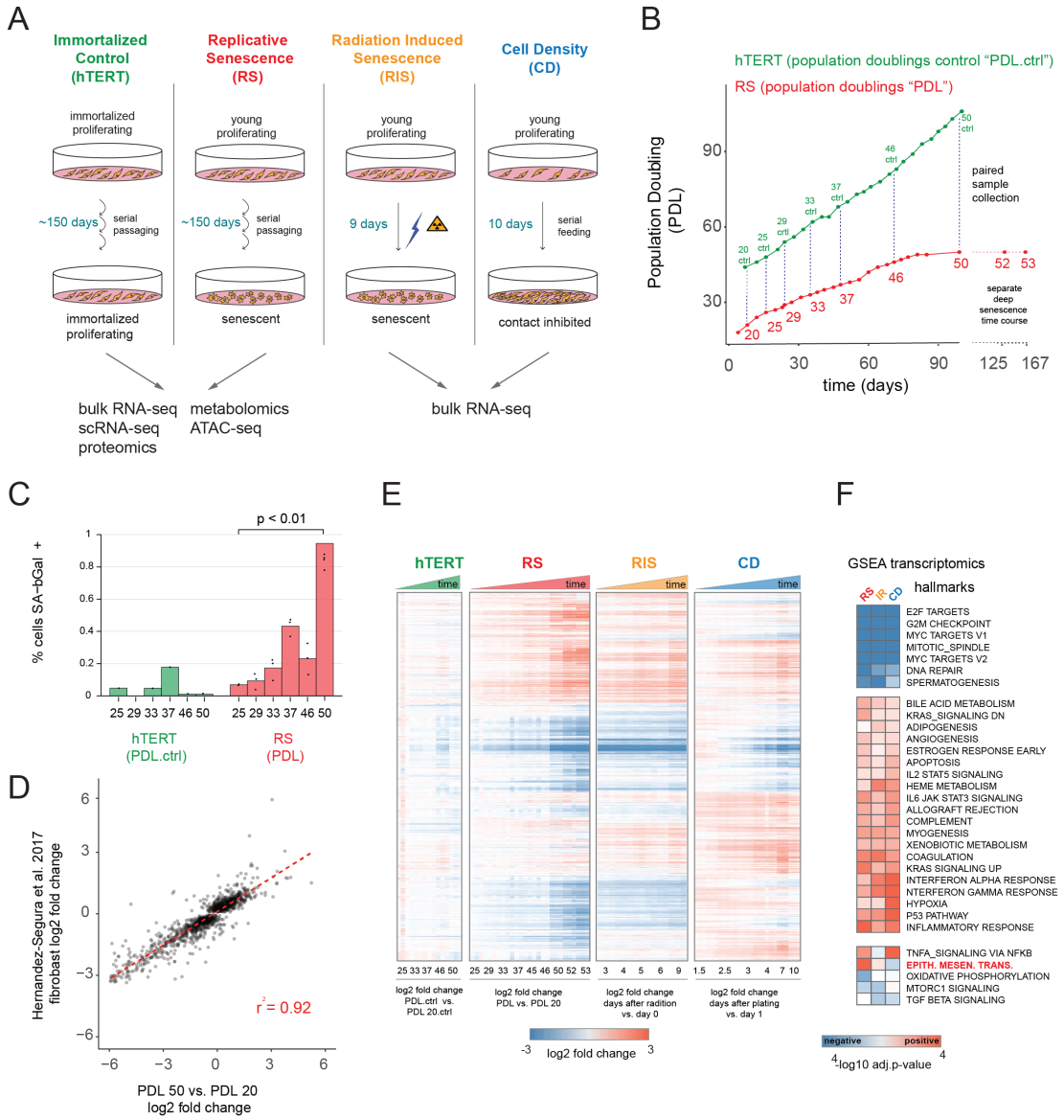

Figure 1: Expression dynamics of replicative senescence (RS), radiation induced senescence (RIS), increasing cell density (CD) and hTERT WI-38 cells. **(A)** Experimental design for the RS, RIS, CD and hTERT experiments. **(B)** Days in culture vs. population doublings (PDL) for WT WI-38 cells (red) and hTERT immortalized cells (green). Labeled points denote sample collection and are expressed in PDLs for RS time course or PDL controls (PDL.ctrl) for the hTERT time course. Temporally paired samples indicated by vertical dotted lines. PDLs 52 and 53 were collected in a separate "deep" senescence time course. **(C)** Percent cells staining positive for SA-βgal staining (y-axis) at increasing PDLs (x-axis) for WI-38 cells (red) and hTERT (green). Points represent replicate values. **(D)** Scatterplot of log2 fold changes in gene expression for PDL 50 vs PDL 20 (x-axis) vs. senescence log2 fold change derived from a generalized linear model compiling gene expression changes across multiple fibroblast cell lines during replicative senescence (***Hernandez-Segura et al., 2017***). **(E)** Hierarchical clustering of significant gene expression changes (FDR adjusted p-value < 0.01) across all conditions (n=3 replicates). Values are log2 fold change vs. the average of the first time point of each condition. Reference time point not shown. **(F)** Significant (FDR adjusted p-value < 0.01) Gene Set Enrichment Analysis (GSEA) results for RS, RIS and CD using the MSigDB Hallmarks annotation set. The -log10 p-value is colored by direction of enrichment (red=up, blue=down).

Figure 1–Figure supplement 1. Sample manifest

Figure 1–Figure supplement 2. Senescence markers

Figure 1–Figure supplement 3. Senescence markers cont'd

Figure 1–Figure supplement 4. Individual time point GSEA

bioRxiv preprint doi: https://doi.org/10.1101/2021.05.03.442497; this version posted November 12, 2021. The copyright holder for this preprint (which was not certified by peer review) is the author/funder. All rights reserved. No reuse allowed without permission.

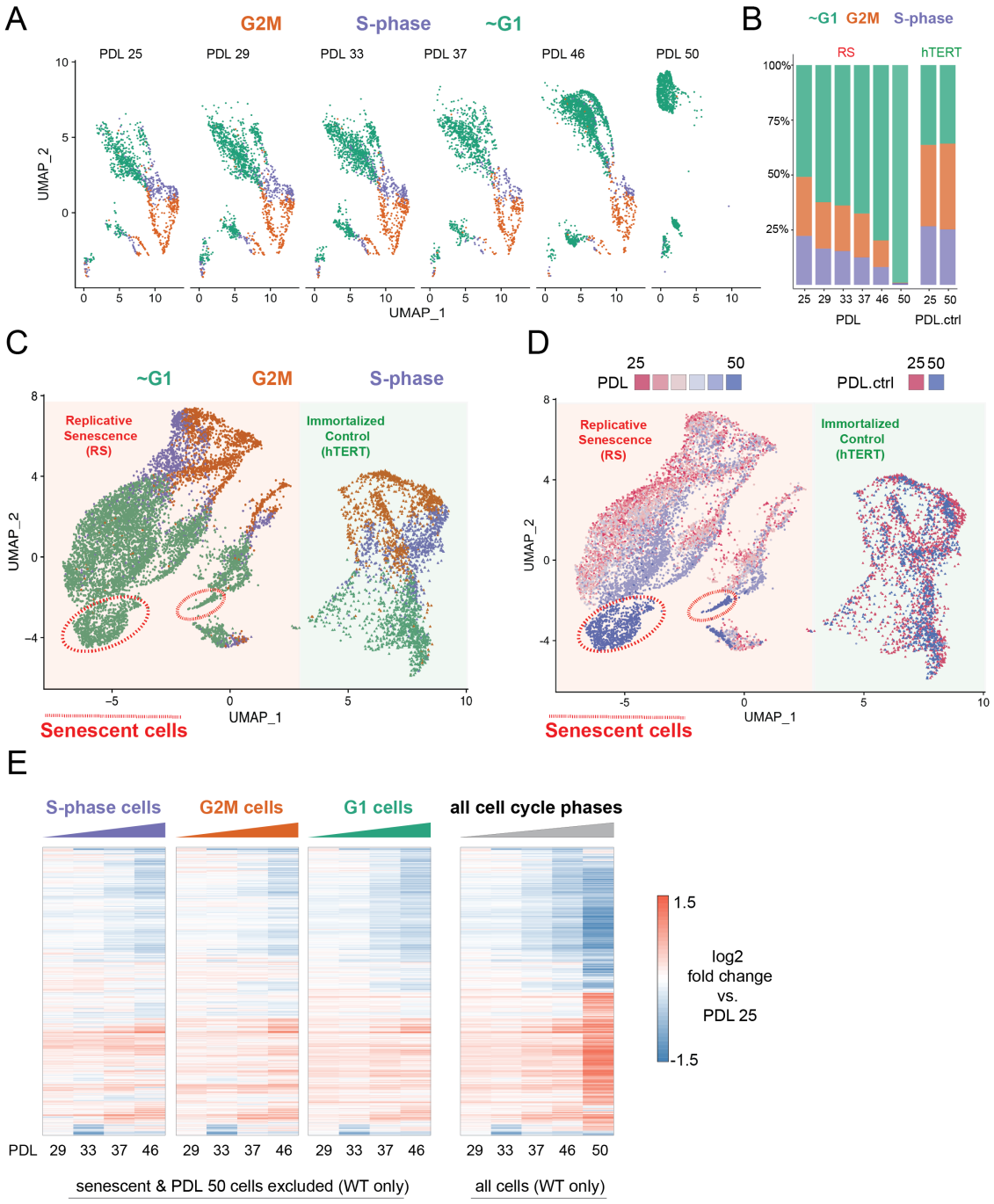

Figure 2: Cell cycle exit and distribution on approach to replicative senescence (RS) does not explain gradual increase in the replicative senescence transcriptome. **(A)** Individual UMAP projections of WT WI-38 cells; PDL colored by phases of the cell cycle (G1 = green, G2/M = orange, S-phase = purple). **(B)** Bar graph of cell cycle state percentages defined by transcriptomic score (y-axis) by PDL (x-axis) for WT WI-38 cells (left) and hTERT WI-38 cells (right). **(C)** UMAP projections of WT and hTERT WI-38 cells by PDL and PDL.ctrl colored by different phases of the cell cycle defined by transcriptomic score. **(D)** UMAP projection of all WI-38 cells from increasing PDLs (RS) or time point (hTERT)-colored from early (red) to late (blue). **(E)** The replicative senescence transcriptome manifests early in all phases of cell cycle. Heatmap of hierarchical clustering of gene expression values of differentially expressed genes as aggregated transcriptomic profiles for each cell cycle phase and PDL (left) versus all cells (right). Values are log2 fold change of each PDL against the reference PDL 25 (not shown).

Figure 2–Figure supplement 1. Buffer optimization for scRNA-seq

Figure 2–Figure supplement 2. Correlation between bulk and single cell RNA-seq

Figure 2–Figure supplement 3. UMAP of mitotic cells

Figure 2–Figure supplement 4. Senescence and cell density scoring of scRNA-seq cells

Figure 2–Figure supplement 5. Images of cell density at sampling

bioRxiv preprint doi: https://doi.org/10.1101/2021.05.03.442497; this version posted November 12, 2021. The copyright holder for this preprint (which was not certified by peer review) is the author/funder. All rights reserved. No reuse allowed without permission.

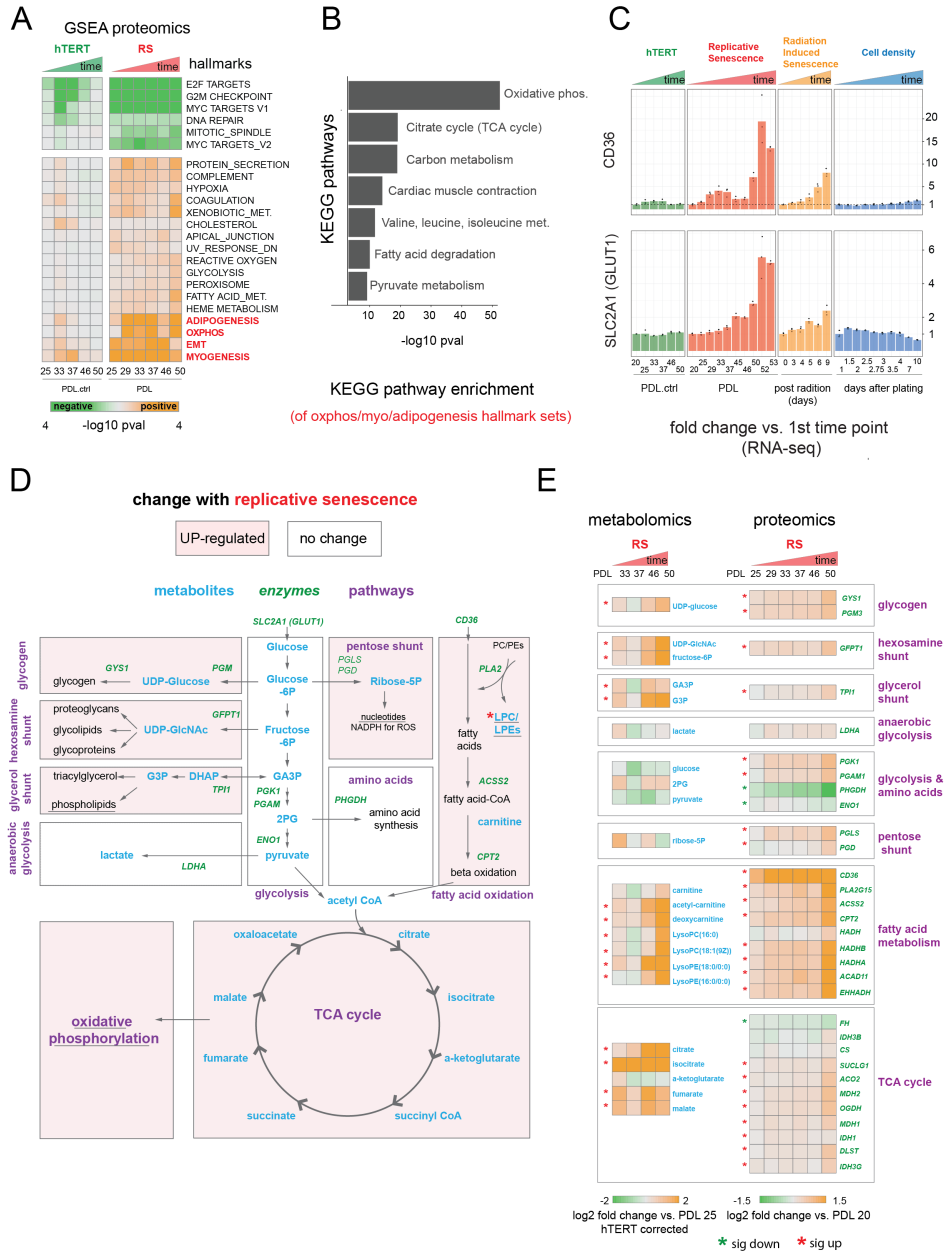

Figure 3: Proteomic and metabolomic changes during replicative senescence. **(A)** Significant (Benjamini-Hochberg adjusted p-value < 0.01) GSEA results for protein changes (n=3) using the MSigDB Hallmarks. Reference time point not shown. Values are -log10 p-value and are colored by the direction (orange=up, green=down). **(B)** KEGG and GO term enrichment of genes from A for selected annotations. **(C)** Gene expression changes (n=3) for insulin-independent glucose transporter SLC2A1 (left) and fatty acid transporter CD36 (right) in the hTERT, replicative senescence, radiation induced senescence and cell density time courses. **(D)** Diagram of glycolysis, glycolytic shunts, fatty acid import and oxidation, TCA cycle/oxidative phosphorylation. Metabolites are blue, proteins are italicized in green. **(E)** Metabolite (n=4) and protein changes (n=3) with senescence from D. Average hTERT corrected metabolite log2 fold change vs. PDL 25 as reference (not shown) are plotted. Proteomics values are average log2 fold change vs PDL 20 as reference (not shown). *:Significant changes (FDR adjusted p<0.05 metabolomics, FDR adjusted p<0.01 proteomics)

Figure 3–Figure supplement 1. PDL-dependent changes in the senescent proteome vs hTERT cells

Figure 3–Figure supplement 2. Correlation between bulk RNA-seq and proteomics

Figure 3–Figure supplement 3. Proteomic changes in oxidative phosphorylation annotation

Figure 3–Figure supplement 4. PDL-dependent changes in the senescent metabolome vs hTERT cells

Figure 3–Figure supplement 5. Kennedy pathway utilization during replicative senescence

bioRxiv preprint doi: https://doi.org/10.1101/2021.05.03.442497; this version posted November 12, 2021. The copyright holder for this preprint (which was not certified by peer review) is the author/funder. All rights reserved. No reuse allowed without permission.

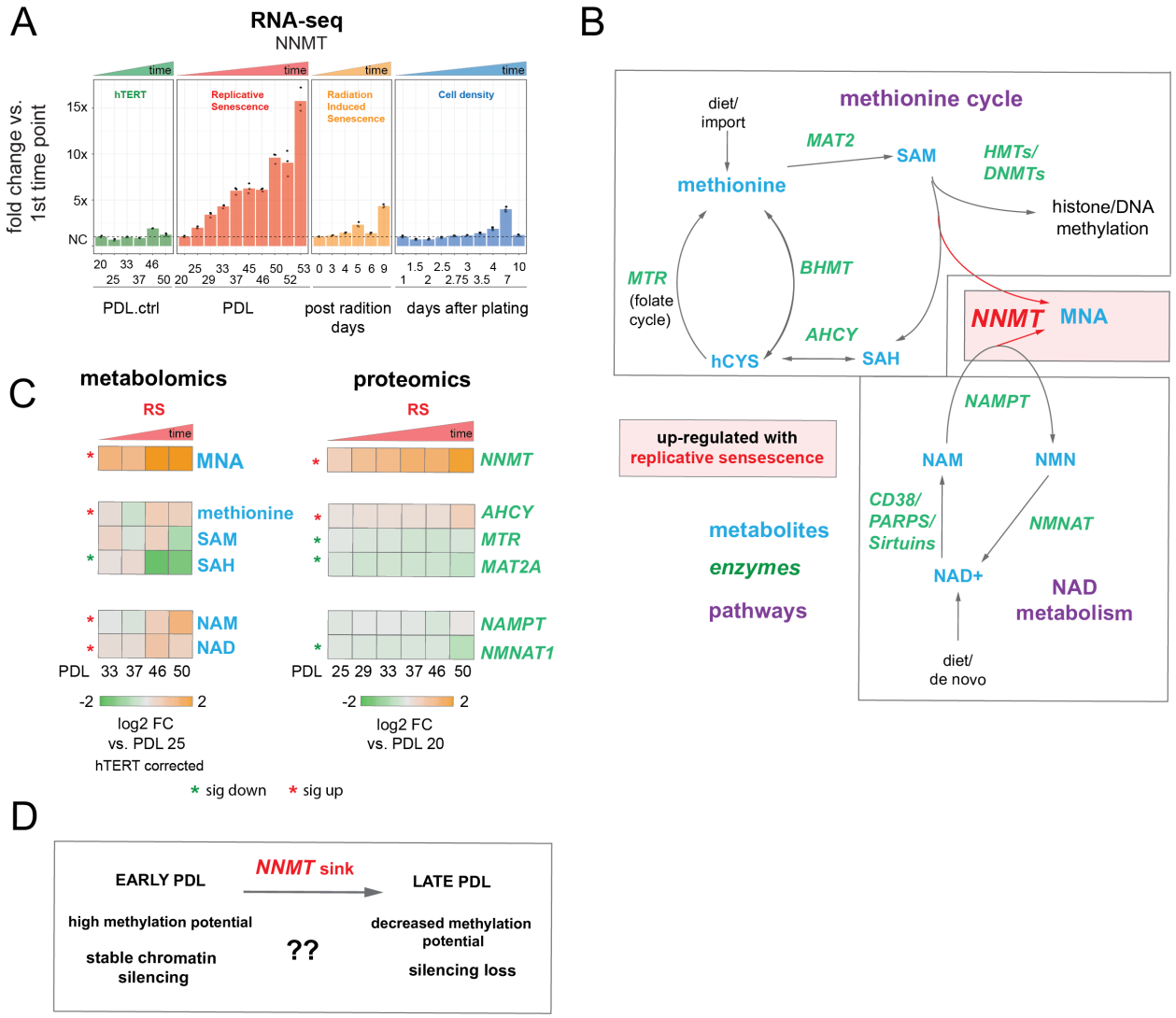

Figure 4: Nicotinamide n-methyltransferase (NNMT) links nicotinamide adenine dinucleotide (NAD) and methionine metabolism during replicative senescence. **(A)** Gene expression fold changes for the NNMT (top) in the hTERT, replicative senescence (RS), radiation induced senescence (RIS), and cell density (CD) time courses (3 replicate average, each point a replicate). Heatmaps of metabolite and protein changes during replicative senescence from B (bottom-replicate average). **(B)** Metabolic diagram of the methionine and NAD salvage pathways. Metabolites are blue, proteins are italicized in green. Shading indicates inferred pathway direction during replicative senescence based on metabolite/protein changes in A. **(C)** Heatmaps of metabolite and protein changes with replicative senescence from B (4 replicate average). Metabolomics data was batch corrected against hTERT samples and expressed as log2 fold change vs PDL 25 as reference(not shown). Proteomics data expressed as log2 fold change vs PDL 20 as reference (not shown). Significant changes (FDR adjusted $p<0.05$ metabolomics, FDR adjusted $p<0.01$ proteomics) during replicative senescence are denoted with asterisks. **(D)** Potential model for NNMT and metabolic regulation of chromatin state during replicative senescence.

bioRxiv preprint doi: https://doi.org/10.1101/2021.05.03.442497; this version posted November 12, 2021. The copyright holder for this preprint (which was not certified by peer review) is the author/funder. All rights reserved. No reuse allowed without permission.

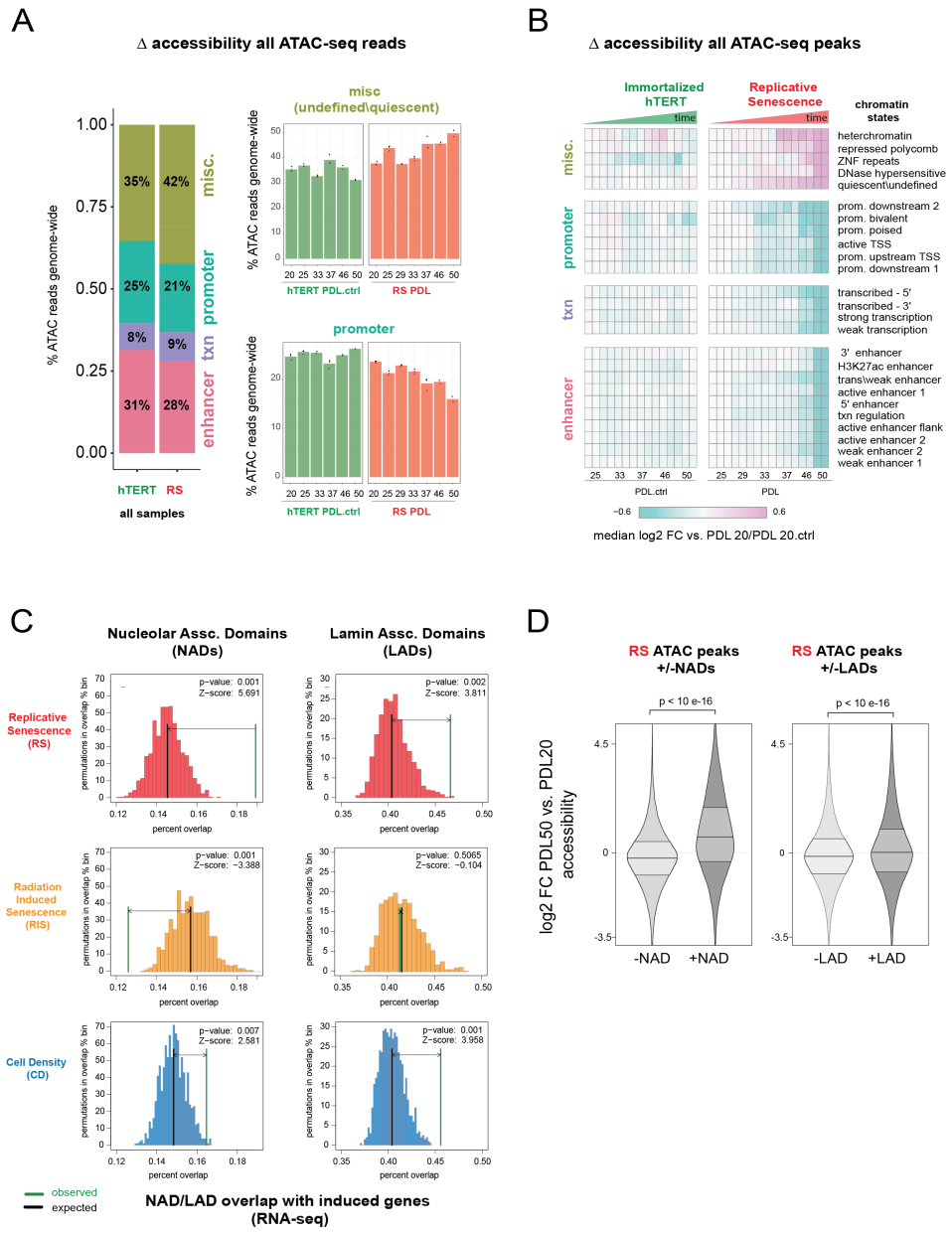

Figure 5: Increased accessibility within heterochromatin and nucleolar associated domains (NADs) is a dominant feature of the replicative senescence (RS) epigenome. **(A)** Percent of ATAC-seq reads falling into 4 broad chromatin states compiled from the ENCODE IMR-90 25 chromatin state prediction for all samples in WT or hTERT WI-38 cells. Percent of all ATAC-seq reads within two specific states (y-axis) vs PDL (x-axis) for WT (red) and hTERT (green) WI-38 cells (bar height denotes average of 3 replicates). **(B)** Median log2 fold change in ATAC-seq counts for significantly changing ATAC-seq peaks binned into ENCODE IMR-90 25 chromatin states (row) for each sample (column, n=2 or 3 replicates). Reference samples are PDL 20 or PDL 20.ctrl for WT and hTERT WI-38 cells respectively (not shown). **(C)** Observed and distribution of expected overlap of significantly induced genes (from Figure 1, RNA-seq) with NADs and LADs. Replicative senescence (red), radiation induced senescence (RIS) (orange) and cell density (CD) (blue). Median expected number of overlaps and observed number of overlaps shown by black and green lines respectively. **(D)** Average (n=2 or 3 replicates) log2 fold change distribution (PDL 50 vs PDL 20) for all ATAC-seq peaks that overlap or are excluded from NADS (left) or LADs (right).

Figure 5–Figure supplement 1. ATAC-seq library fragment distribution and size selection

Figure 5–Figure supplement 2. ATAC-seq library fragment distribution after size selection and sequencing

Figure 5–Figure supplement 3. ATAC-seq mitochondrial read percentages and ATAC-seq transcriptional start site enrichment

Figure 5–Figure supplement 4. ATAC-seq QC metrics and extended analysis

Figure 5–Figure supplement 5. Chromatin state profiles of ATAC-seq peaks in Nucleolar Associated Domains

bioRxiv preprint doi: https://doi.org/10.1101/2021.05.03.442497; this version posted November 12, 2021. The copyright holder for this preprint (which was not certified by peer review) is the author/funder. All rights reserved. No reuse allowed without permission.

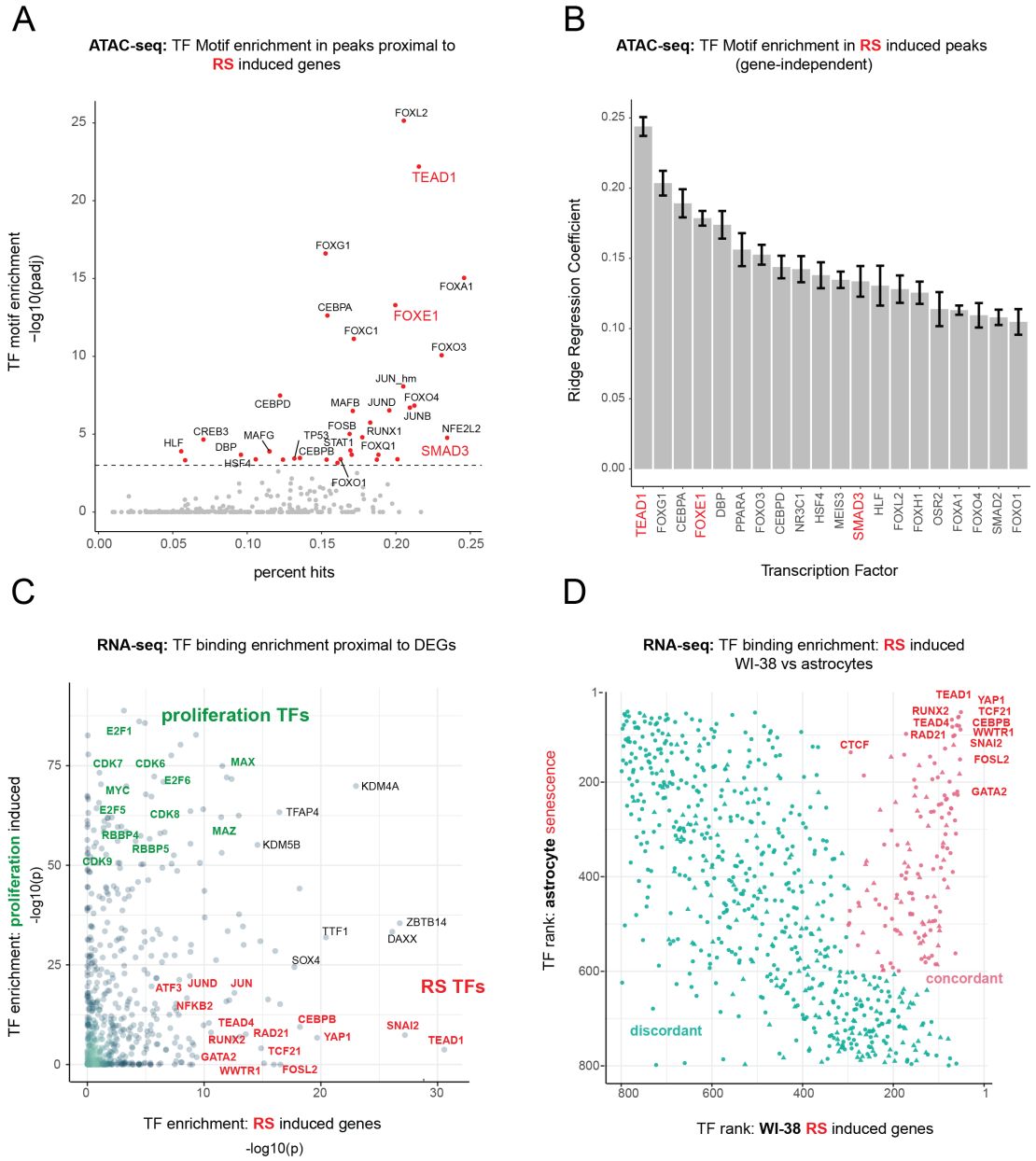

Figure 6: Master transcriptional regulators of replicative senescence **(A)** Scatter plot of transcription factor motif enrichment in ATAC-seq peaks surrounding significantly induced genes (FDR adjusted p< 0.01, log2 FC > 0.5) during replicative senescence. The Y-axis is the -log10 p-value; x-axis is the percent of input genes with the transcription factor motif. All points are transcription factors. Specific transcription factors of interest are called out in red. **(B)** Bar graph of ridge regression coefficient of motif predictive power in model of increasing peak accessibility with replicative senescence. Transcription factors of interest are highlighted in red. **(C)** Scatterplot of transcription factors enriched for binding in regulatory regions around replicative senescence depleted genes (y-axis, FDR adjusted p< 0.01, log2 FC < -0.5) vs. replicative senescence induced genes (x-axis, FDR adjusted p< 0.01, log2 FC < -0.5). Curated cell cycle transcription factors are colored in green; transcription factors of interest e.g. EMT/AP1/YAP1/TEAD1 etc. are colored in red. **(D)** Scatterplot of enriched transcription factors rank for binding enrichment in regulatory regions around senescence induced genes in astrocytes (y-axis) vs. replicative senescence induced genes in WI-38 cells (x-axis). transcription factors with discordant ranks/enrichment are colored in turquoise,transcription factors with concordant ranks/enrichment are colored in red; transcription factors of interest are labeled in red.

Figure 6–Figure supplement 1. FOXE1 expression during senescence.

bioRxiv preprint doi: https://doi.org/10.1101/2021.05.03.442497; this version posted November 12, 2021. The copyright holder for this preprint (which was not certified by peer review) is the author/funder. All rights reserved. No reuse allowed without permission.

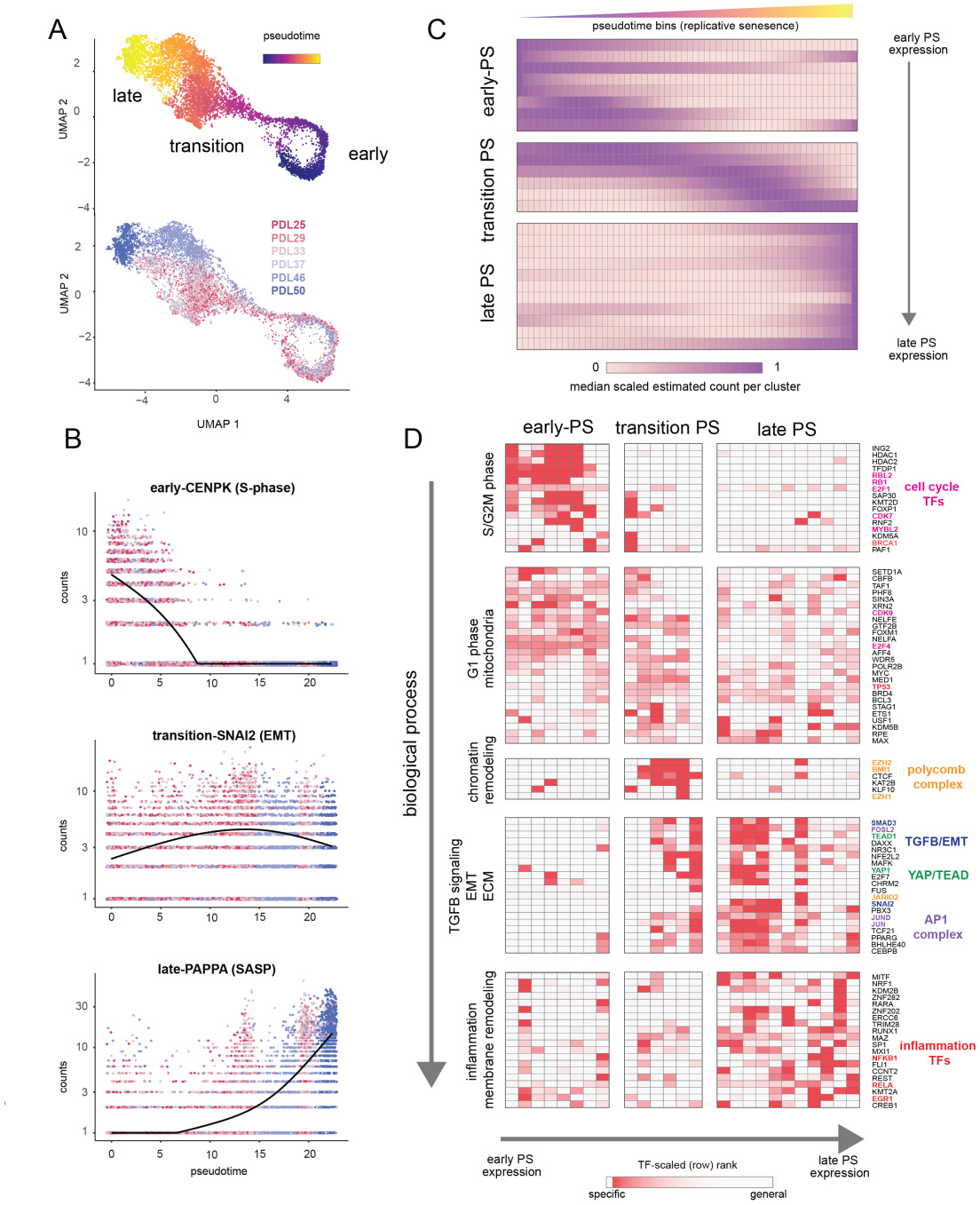

Figure 7: Pseudotime (PS) analysis of WI-38 approach to replicative senescence using single cell RNA-seq. **(A)** UMAP projection of single WI-38 cells collected at increasing PDLs (PDL25-red) to (PDL50-blue) and colored by pseudotime (top). **(B)** Scatterplot of single cell gene expression across pseudotime with 3 genes representative of changes that occur early in pseudotime (top), during the transition phase (middle) and in late pseudotime (bottom). Each point is a cell colored by PDL–PDL25 (red) to PDL50 (blue). x-axis is pseudotime, and y-axis is counts for the gene of interest. Black line is a cubic spline. **(C)** Hierarchical clustering and heatmap of smoothened gene expression trajectories over 60 pseudotime bins (x-axis) of 25 K-median gene expression clusters (y-axis). Value plotted is the scaled (min expression to max expression ; 0-1) median expression of all genes in the cluster. Clusters are divided into three (early, transition, late) pseudotime categories. **(D)** LISA transcription factor enrichment analysis using the 25 clusters from A divided into the same three (early, transition, late) pseudotime categories. Transcription factors and clusters are further divided on vertical axis into putative groupings based on transcription factor functions and GO term enrichment.

Figure 7–Figure supplement 1. Heatmap of genes changing with senescence pseudotime

Figure 7–Figure supplement 2. Heatmap of enriched gene sets for replicative senescence pseudotime clusters

bioRxiv preprint doi: https://doi.org/10.1101/2021.05.03.442497; this version posted November 12, 2021. The copyright holder for this preprint (which was not certified by peer review) is the author/funder. All rights reserved. No reuse allowed without permission.

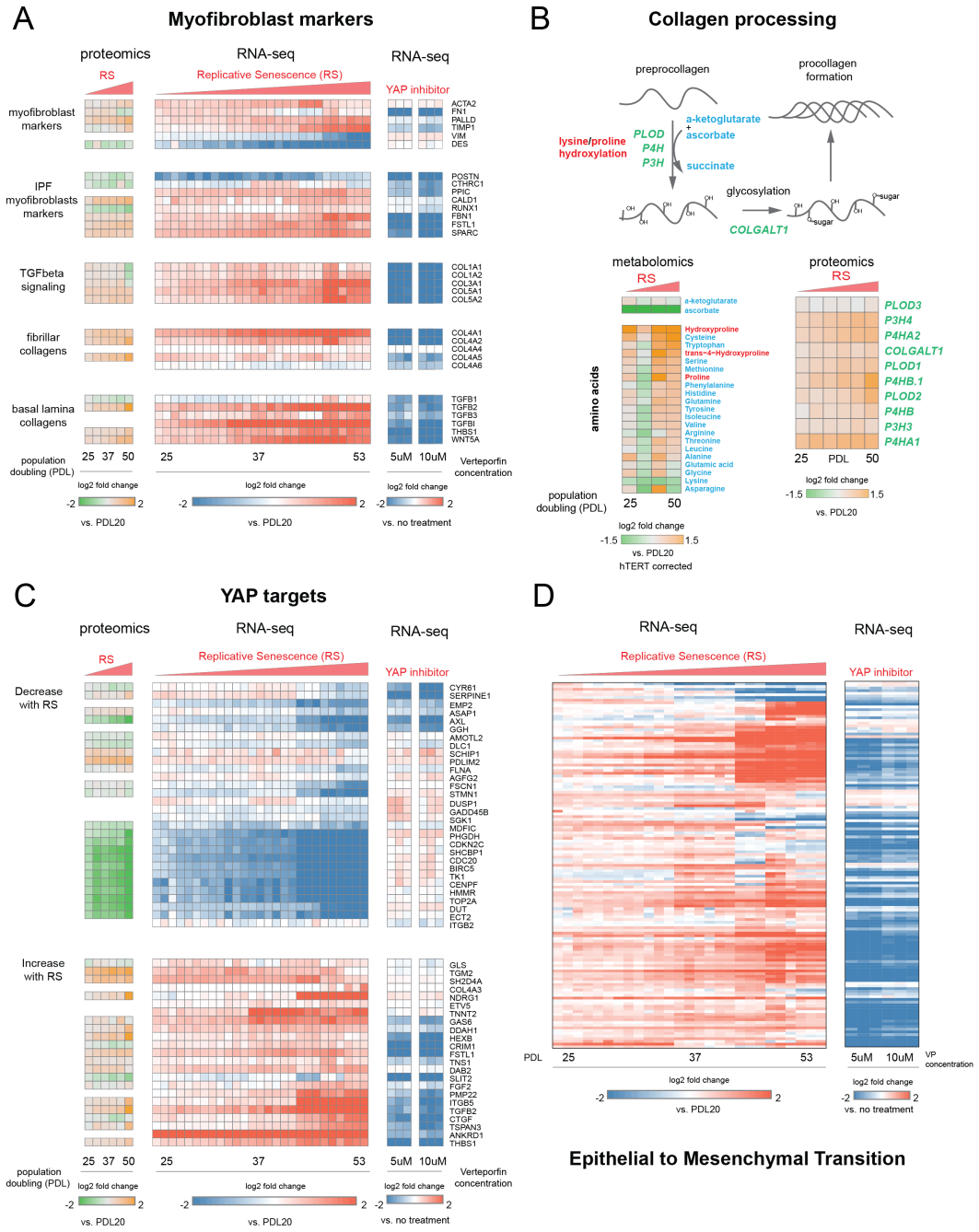

Figure 8: YAP regulation of myofibroblast markers and YAP1/TEAD1 targets during replicative senescence. **(A)** RNA-seq and proteomics heatmaps of selected genes based on myofibroblast markers and biology. Values plotted are log2 fold change of each PDL vs PDL 20 for replicative senescence timecourse and vs. no treatment for late PDL (PDL 40) WI-38 cells treated with the YAP inhibitor verteporfin. Proteomics values are median values for n=3 replicates. Values for individual RNA-seq replicates (n=3) are shown). **(B)** Diagram of collagen processing (left) with metabolites in blue and proteins in italicized green. Collagen specific amino acid derivatives are outlined in red. Heatmap of log2 fold changes for metabolites and proteins involved in collagen processing (right). Proteomics values are median values for n=3 replicates. Metabolomics values are hTERT batch corrected median values for n=4 replicates). **(C)** Heatmaps of YAP1 targets collected by ***Kurppa et al.*** (***2020***). for proteomics and RNA-seq during replicative senescence and in late PDL (PDL 40) WI-38 cells treated with the YAP inhibitor verteporfin. Values plotted are same as in A.) **(D)** Heatmap of log2 fold changes relative to PDL 20 or untreated control of leading edge genes from gene set enrichment analysis driving the Hallmarks EMT signature in verteporfin treated WI-38 cells and during replicative senescence. Values for individual RNA-seq replicates (n=3) are shown.

Figure 8–Figure supplement 1. Effect of inhibiting the YAP1/TEAD1 interaction with verteporfin treatment on WI-38 cells

bioRxiv preprint doi: https://doi.org/10.1101/2021.05.03.442497; this version posted November 12, 2021. The copyright holder for this preprint (which was not certified by peer review) is the author/funder. All rights reserved. No reuse allowed without permission.

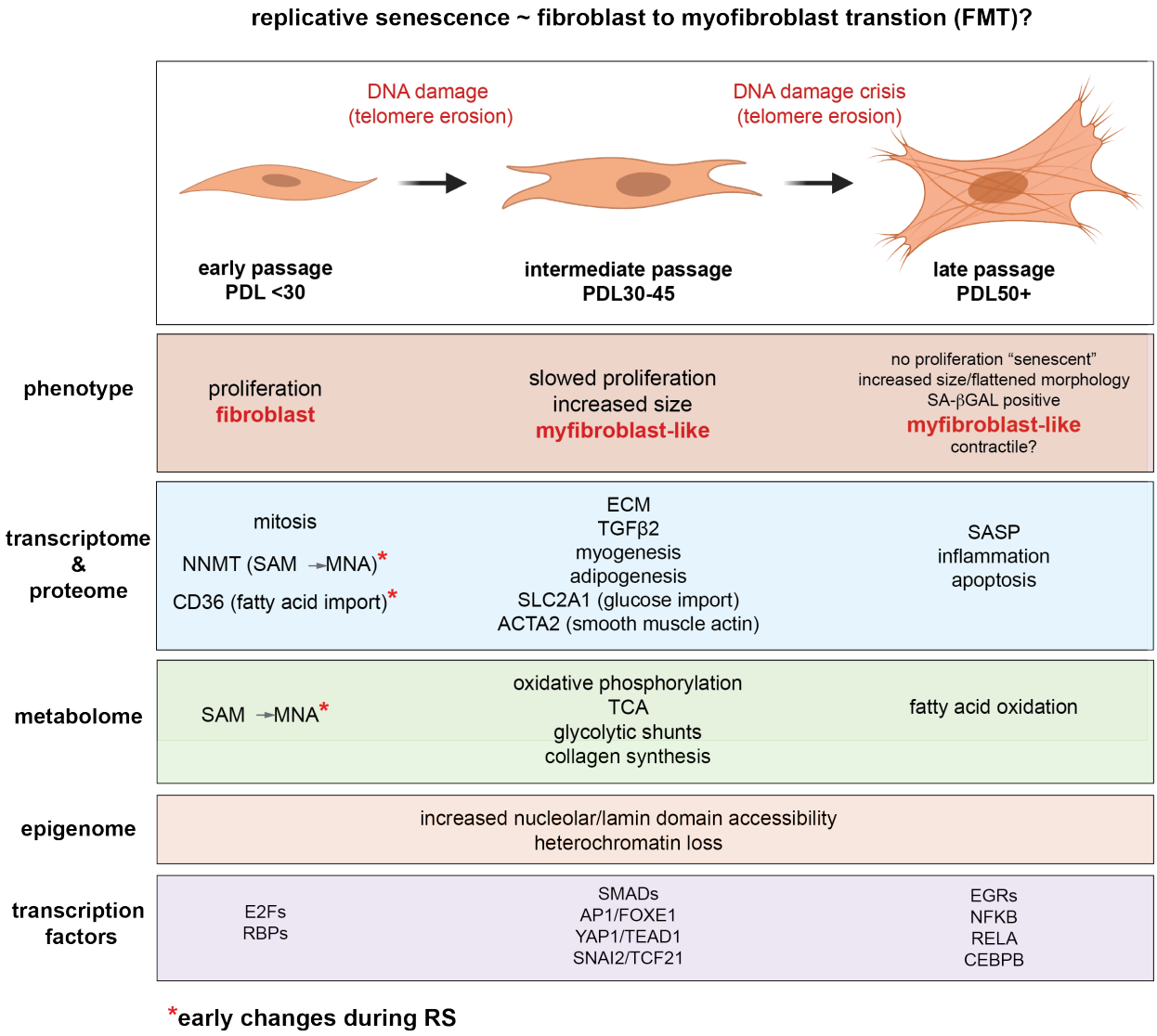

Figure 9: Replicative senescence fibroblast to myofibroblast transition (FMT) model. We divided Replicative senescence progression into three major categories and summarized our results across all data modalities focusing on features in common with myofibroblasts.

bioRxiv preprint doi: https://doi.org/10.1101/2021.05.03.442497; this version posted November 12, 2021. The copyright holder for this preprint (which was not certified by peer review) is the author/funder. All rights reserved. No reuse allowed without permission.

References

Absher PM, Absher R, Barnes W. Genealogies of clones of diploid fibroblasts: Cinemicrophotographic observations of cell division patterns in relation to population age. Experimental cell research. 1974; 88(1):95–104.

Acosta JC, Banito A, Wuestefeld T, Georgilis A, Janich P, Morton JP, Athineos D, Kang TW, Lasitschka F, Andrulis M, Pascual G, Morris KJ, Khan S, Jin H, Dharmalingam G, Snijders AP, Carroll T, Capper D, Pritchard C, Inman GJ, et al. A complex secretory program orchestrated by the inflammasome controls paracrine senescence. Nat Cell Biol. 2013 Aug; 15(8):978–990.

Aghajanian H, Kimura T, Rurik JG, Hancock AS, Leibowitz MS, Li L, Scholler J, Monslow J, Lo A, Han W, et al. Targeting cardiac fibrosis with engineered T cells. Nature. 2019; 573(7774):430–433.

Alder JK, Chen JJL, Lancaster L, Danoff S, Su Sc, Cogan JD, Vulto I, Xie M, Qi X, Tuder RM, et al. Short telomeres are a risk factor for idiopathic pulmonary fibrosis. Proceedings of the National Academy of Sciences. 2008; 105(35):13051–13056.

Amor C, Feucht J, Leibold J, Ho YJ, Zhu C, Alonso-Curbelo D, Mansilla-Soto J, Boyer JA, Li X, Giavridis T, et al. Senolytic CAR T cells reverse senescence-associated pathologies. Nature. 2020; 583(7814):127–132.

Armanios MY, Chen JJL, Cogan JD, Alder JK, Ingersoll RG, Markin C, Lawson WE, Xie M, Vulto I, Phillips III JA, et al. Telomerase mutations in families with idiopathic pulmonary fibrosis. New England Journal of Medicine. 2007; 356(13):1317–1326.

Azakie A, Lamont L, Fineman JR, He Y. Divergent transcriptional enhancer factor-1 regulates the cardiac troponin T promoter. Am J Physiol Cell Physiol. 2005 Dec; 289(6):C1522–34.

Becht E, McInnes L, Healy J, Dutertre CA, Kwok IW, Ng LG, Ginhoux F, Newell EW. Dimensionality reduction for visualizing single-cell data using UMAP. Nature biotechnology. 2019; 37(1):38–44.

Benayoun BA, Pollina EA, Brunet A. Epigenetic regulation of ageing: linking environmental inputs to genomic stability. Nature reviews Molecular cell biology. 2015; 16(10):593–610.

Benhaddou A, Keime C, Ye T, Morlon A, Michel I, Jost B, Mengus G, Davidson I. Transcription factor TEAD4 regulates expression of Myogenin and the unfolded protein response genes during C2C12 cell differentiation. Cell Death & Differentiation. 2012; 19(2):220–231.

Blondel VD, Guillaume JL, Lambiotte R, Lefebvre E. Fast unfolding of communities in large networks. Journal of statistical mechanics: theory and experiment. 2008; 2008(10):P10008.

Bodnar AG, Ouellette M, Frolkis M, Holt SE, Chiu CP, Morin GB, Harley CB, Shay JW, Lichtsteiner S, Wright WE. Extension of life-span by introduction of telomerase into normal human cells. Science. 1998 Jan; 279(5349):349–352.

Borghesan M, Hoogaars W, Varela-Eirin M, Talma N, Demaria M. A senescence-centric view of aging: implications for longevity and disease. Trends in Cell Biology. 2020; .

Boyera N, Galey I, Bernard B. Effect of vitamin C and its derivatives on collagen synthesis and cross-linking by normal human fibroblasts. International journal of cosmetic science. 1998; 20(3):151–158.

Campisi J, Di Fagagna FD. Cellular senescence: when bad things happen to good cells. Nature reviews Molecular cell biology. 2007; 8(9):729–740.

Cao J, Spielmann M, Qiu X, Huang X, Ibrahim DM, Hill AJ, Zhang F, Mundlos S, Christiansen L, Steemers FJ, et al. The single-cell transcriptional landscape of mammalian organogenesis. Nature. 2019; 566(7745):496–502.

Chakravarti D, Hu B, Mao X, Rashid A, Li J, Li J, Liao Wt, Whitley EM, Dey P, Hou P, et al. Telomere dysfunction activates YAP1 to drive tissue inflammation. Nature communications. 2020; 11(1):1–13.

Chen CC, Mo FE, Lau LF. The angiogenic factor Cyr61 activates a genetic program for wound healing in human skin fibroblasts. Journal of Biological Chemistry. 2001; 276(50):47329–47337.

Chen Z, Friedrich GA, Soriano P. Transcriptional enhancer factor 1 disruption by a retroviral gene trap leads to heart defects and embryonic lethality in mice. Genes & Development. 1994; 8(19):2293–2301.

Childs BG, Durik M, Baker DJ, Van Deursen JM. Cellular senescence in aging and age-related disease: from mechanisms to therapy. Nature medicine. 2015; 21(12):1424–1435.

bioRxiv preprint doi: https://doi.org/10.1101/2021.05.03.442497; this version posted November 12, 2021. The copyright holder for this preprint (which was not certified by peer review) is the author/funder. All rights reserved. No reuse allowed without permission.

Coppé JP, Kauser K, Campisi J, Beauséjour CM. Secretion of vascular endothelial growth factor by primary human fibroblasts at senescence. J Biol Chem. 2006 Oct; 281(40):29568–29574.

Coppé JP, Patil CK, Rodier F, Sun Y, Muñoz DP, Goldstein J, Nelson PS, Desprez PY, Campisi J. Senescence-associated secretory phenotypes reveal cell-nonautonomous functions of oncogenic RAS and the p53 tumor suppressor. PLoS Biol. 2008 Dec; 6(12):2853–2868.

Corbet C, Bastien E, de Jesus JPS, Dierge E, Martherus R, Vander Linden C, Doix B, Degavre C, Guilbaud C, Petit L, et al. TGFβ2-induced formation of lipid droplets supports acidosis-driven EMT and the metastatic spreading of cancer cells. Nature communications. 2020; 11(1):1–15.

Cronkhite JT, Xing C, Raghu G, Chin KM, Torres F, Rosenblatt RL, Garcia CK. Telomere shortening in familial and sporadic pulmonary fibrosis. Am J Respir Crit Care Med. 2008 Oct; 178(7):729–737.

Crowe EP, Tuzer F, Gregory BD, Donahue G, Gosai SJ, Cohen J, Leung YY, Yetkin E, Nativio R, Wang LS, et al. Changes in the transcriptome of human astrocytes accompanying oxidative stress-induced senescence. Frontiers in aging neuroscience. 2016; 8:208.

Dai J, Cai H, Li H, Zhuang Y, Min H, Wen Y, Yang J, Gao Q, Shi Y, Yi L. Association between telomere length and survival in patients with idiopathic pulmonary fibrosis. Respirology. 2015; 20(6):947–952.

De Cecco M, Ito T, Petrashen AP, Elias AE, Skvir NJ, Criscione SW, Caligiana A, Brocculi G, Adney EM, Boeke JD, et al. L1 drives IFN in senescent cells and promotes age-associated inflammation. Nature. 2019; 566(7742):73–78.

Demaria M, Ohtani N, Youssef SA, Rodier F, Toussaint W, Mitchell JR, Laberge RM, Vijg J, Van Steeg H, Dollé MET, Hoeijmakers JHJ, de Bruin A, Hara E, Campisi J. An essential role for senescent cells in optimal wound healing through secretion of PDGF-AA. Dev Cell. 2014 Dec; 31(6):722–733.

Dillinger S, Straub T, Németh A. Nucleolus association of chromosomal domains is largely maintained in cellular senescence despite massive nuclear reorganisation. PLoS One. 2017 Jun; 12(6):e0178821.

Ding Z, Ke R, Zhang Y, Fan Y, Fan J. FOXE1 inhibits cell proliferation, migration and invasion of papillary thyroid cancer by regulating PDGFA. Molecular and cellular endocrinology. 2019; 493:110420.

Duckworth A, Gibbons MA, Allen RJ, Almond H, Beaumont RN, Wood AR, Lunnon K, Lindsay MA, Wain LV, Tyrrell J, et al. Telomere length and risk of idiopathic pulmonary fibrosis and chronic obstructive pulmonary disease: a mendelian randomisation study. The Lancet Respiratory Medicine. 2021; 9(3):285–294.

Eckert MA, Coscia F, Chryplewicz A, Chang JW, Hernandez KM, Pan S, Tienda SM, Nahotko DA, Li G, Blaženović I, et al. Proteomics reveals NNMT as a master metabolic regulator of cancer-associated fibroblasts. Nature. 2019; 569(7758):723–728.

Elmore MR, Hohsfield LA, Kramár EA, Soreq L, Lee RJ, Pham ST, Najafi AR, Spangenberg EE, Wood MA, West BL, et al. Replacement of microglia in the aged brain reverses cognitive, synaptic, and neuronal deficits in mice. Aging cell. 2018; 17(6):e12832.

Ernst J, Kellis M. Large-scale imputation of epigenomic datasets for systematic annotation of diverse human tissues. Nat Biotechnol. 2015 Apr; 33(4):364–376.

Ewels P, Magnusson M, Lundin S, Käller M. MultiQC: summarize analysis results for multiple tools and samples in a single report. Bioinformatics. 2016; 32(19):3047–3048.

Flor AC, Wolfgeher D, Wu D, Kron SJ. A signature of enhanced lipid metabolism, lipid peroxidation and aldehyde stress in therapy-induced senescence. Cell death discovery. 2017; 3(1):1–12.

Fu L, Hu Y, Song M, Liu Z, Zhang W, Yu FX, Wu J, Wang S, Izpisua Belmonte JC, Chan P, Qu J, Tang F, Liu GH. Up-regulation of FOXD1 by YAP alleviates senescence and osteoarthritis. PLoS Biol. 2019 Apr; 17(4):e3000201.

Gaun A, Lewis Hardell KN, Olsson N, O'Brien JJ, Gollapudi S, Smith M, McAlister G, Huguet R, Keyser R, Buffenstein R, et al. Automated 16-plex plasma proteomics with real-time search and ion mobility mass spectrometry enables large-scale profiling in naked mole-rats and mice. Journal of Proteome Research. 2021; 20(2):1280–1295.

Gel B, Díez-Villanueva A, Serra E, Buschbeck M, Peinado MA, Malinverni R. regioneR: an R/Bioconductor package for the association analysis of genomic regions based on permutation tests. Bioinformatics. 2016; 32(2):289–291.

bioRxiv preprint doi: https://doi.org/10.1101/2021.05.03.442497; this version posted November 12, 2021. The copyright holder for this preprint (which was not certified by peer review) is the author/funder. All rights reserved. No reuse allowed without permission.

Gibb AA, Lazaropoulos MP, Elrod JW. Myofibroblasts and Fibrosis: Mitochondrial and Metabolic Control of Cellular Differentiation. Circulation Research. 2020; 127(3):427–447.

Gorgoulis V, Adams PD, Alimonti A, Bennett DC, Bischof O, Bishop C, Campisi J, Collado M, Evangelou K, Ferbeyre G, Gil J, Hara E, Krizhanovsky V, Jurk D, Maier AB, Narita M, Niedernhofer L, Passos JF, Robbins PD, Schmitt CA, et al. Cellular Senescence: Defining a Path Forward. Cell. 2019 Oct; 179(4):813–827.

Hafemeister C, Satija R. Normalization and variance stabilization of single-cell RNA-seq data using regularized negative binomial regression. Genome Biology. 2019; 20:296. https://doi.org/10.1186/s13059-019-1874-1, doi: 10.1186/s13059-019-1874-1.

Harley CB, Futcher AB, Greider CW. Telomeres shorten during ageing of human fibroblasts. Nature. 1990; 345(6274):458–460.

Hayflick L. The limited in vitro lifetime of human diploid cell strains. Experimental cell research. 1965; 37(3):614–636.

Hendrickson DG, Soifer I, Wranik BJ, Kim G, Robles M, Gibney PA, McIsaac RS. A new experimental platform facilitates assessment of the transcriptional and chromatin landscapes of aging yeast. Elife. 2018 Oct; 7.

Herbig U, Ferreira M, Condel L, Carey D, Sedivy JM. Cellular senescence in aging primates. Science. 2006; 311(5765):1257–1257.

Hernandez-Segura A, de Jong TV, Melov S, Guryev V, Campisi J, Demaria M. Unmasking Transcriptional Heterogeneity in Senescent Cells. Curr Biol. 2017 Sep; 27(17):2652–2660.e4.

Hernandez-Segura A, Nehme J, Demaria M. Hallmarks of cellular senescence. Trends in cell biology. 2018; 28(6):436–453.

Hinz B. Formation and function of the myofibroblast during tissue repair. Journal of Investigative Dermatology. 2007; 127(3):526–537.

Hinz B, Lagares D. Evasion of apoptosis by myofibroblasts: a hallmark of fibrotic diseases. Nat Rev Rheumatol. 2020 Jan; 16(1):11–31.

Hua W, Ten Dijke P, Kostidis S, Giera M, Hornsveld M. TGFβ-induced metabolic reprogramming during epithelial-to-mesenchymal transition in cancer. Cellular and Molecular Life Sciences. 2020; 77(11):2103–2123.

Huttlin EL, Jedrychowski MP, Elias JE, Goswami T, Rad R, Beausoleil SA, Villén J, Haas W, Sowa ME, Gygi SP. A tissue-specific atlas of mouse protein phosphorylation and expression. Cell. 2010; 143(7):1174–1189.

Idda ML, McClusky WG, Lodde V, Munk R, Abdelmohsen K, Rossi M, Gorospe M. Survey of senescent cell markers with age in human tissues. Aging. 2020 Mar; 12(5):4052–4066.

James EL, Lane JA, Michalek RD, Karoly ED, Parkinson EK. Replicatively senescent human fibroblasts reveal a distinct intracellular metabolic profile with alterations in NAD+ and nicotinamide metabolism. Scientific reports. 2016; 6(1):1–15.

Jeyapalan JC, Sedivy JM. Cellular senescence and organismal aging. Mechanisms of ageing and development. 2008; 129(7-8):467–474.

Jia L, Gu W, Zhang Y, Jiang B, Qiao X, Wen Y. Activated Yes-Associated Protein Accelerates Cell Cycle, Inhibits Apoptosis, and Delays Senescence in Human Periodontal Ligament Stem Cells. Int J Med Sci. 2018 Jul; 15(11):1241–1250.

Johmura Y, Yamanaka T, Omori S, Wang TW, Sugiura Y, Matsumoto M, Suzuki N, Kumamoto S, Yamaguchi K, Hatakeyama S, et al. Senolysis by glutaminolysis inhibition ameliorates various age-associated disorders. Science. 2021; 371(6526):265–270.

Jun JI, Lau LF. The matricellular protein CCN1 induces fibroblast senescence and restricts fibrosis in cutaneous wound healing. Nat Cell Biol. 2010 Jul; 12(7):676–685.

Kallel R, Belguith-Maalej S, Akdi A, Mnif M, Charfeddine I, Galofré P, Ghorbel A, Abid M, Marcos R, Ayadi H, et al. Genetic investigation of FOXE1 polyalanine tract in thyroid diseases: new insight on the role of FOXE1 in thyroid carcinoma. Cancer Biomarkers. 2011; 8(1):43–51.

Kim CL, Choi SH, Mo JS. Role of the Hippo Pathway in Fibrosis and Cancer. Cells. 2019 May; 8(5).

bioRxiv preprint doi: https://doi.org/10.1101/2021.05.03.442497; this version posted November 12, 2021. The copyright holder for this preprint (which was not certified by peer review) is the author/funder. All rights reserved. No reuse allowed without permission.

Kim W, Cho YS, Wang X, Park O, Ma X, Kim H, Gan W, Jho Eh, Cha B, Jeung Yj, et al. Hippo signaling is intrinsically regulated during cell cycle progression by APC/CCdh1. Proceedings of the National Academy of Sciences. 2019; 116(19):9423–9432.

Komatsu M, Kanda T, Urai H, Kurokochi A, Kitahama R, Shigaki S, Ono T, Yukioka H, Hasegawa K, Tokuyama H, et al. NNMT activation can contribute to the development of fatty liver disease by modulating the NAD+ metabolism. Scientific reports. 2018; 8(1):1–15.

Korotkevich G, Sukhov V, Sergushichev A. Fast gene set enrichment analysis. BioRxiv. 2019; p. 060012.

Kozieł R, Ruckenstuhl C, Albertini E, Neuhaus M, Netzberger C, Bust M, Madeo F, Wiesner RJ, Jansen-Dürr P. Methionine restriction slows down senescence in human diploid fibroblasts. Aging cell. 2014; 13(6):1038–1048.

Krizhanovsky V, Yon M, Dickins RA, Hearn S, Simon J, Miething C, Yee H, Zender L, Lowe SW. Senescence of activated stellate cells limits liver fibrosis. Cell. 2008 Aug; 134(4):657–667.

Kurppa KJ, Liu Y, To C, Zhang T, Fan M, Vajdi A, Knelson EH, Xie Y, Lim K, Cejas P, Portell A, Lizotte PH, Ficarro SB, Li S, Chen T, Haikala HM, Wang H, Bahcall M, Gao Y, Shalhout S, et al. Treatment-Induced Tumor Dormancy through YAP-Mediated Transcriptional Reprogramming of the Apoptotic Pathway. Cancer Cell. 2020 Jan; 37(1):104–122.e12.

Landin Malt A, Cagliero J, Legent K, Silber J, Zider A, Flagiello D. Alteration of TEAD1 expression levels confers apoptotic resistance through the transcriptional up-regulation of Livin. PLoS One. 2012 Sep; 7(9):e45498.

Lawrence M, Huber W, Pages H, Aboyoun P, Carlson M, Gentleman R, Morgan MT, Carey VJ. Software for computing and annotating genomic ranges. PLoS Comput Biol. 2013; 9(8):e1003118.

Lee Ck, Jeong Sh, Jang C, Bae H, Kim YH, Park I, Kim SK, Koh GY. Tumor metastasis to lymph nodes requires YAP-dependent metabolic adaptation. Science. 2019; 363(6427):644–649.

Levine JH, Simonds EF, Bendall SC, Davis KL, El-ad DA, Tadmor MD, Litvin O, Fienberg HG, Jager A, Zunder ER, et al. Data-driven phenotypic dissection of AML reveals progenitor-like cells that correlate with prognosis. Cell. 2015; 162(1):184–197.

Liberzon A, Birger C, Thorvaldsdóttir H, Ghandi M, Mesirov JP, Tamayo P. The molecular signatures database hallmark gene set collection. Cell systems. 2015; 1(6):417–425.

Liu T, Hu B, Chung MJ, Ullenbruch M, Jin H, Phan SH. Telomerase regulation of myofibroblast differentiation. American journal of respiratory cell and molecular biology. 2006; 34(5):625–633.

Liu T, Nozaki Y, Phan SH. Regulation of telomerase activity in rat lung fibroblasts. American journal of respiratory cell and molecular biology. 2002; 26(5):534–540.

Lodish H, Zipursky SL. Molecular cell biology. Biochem Mol Biol Educ. 2001; 29:126–133.

Lombardi AA, Gibb AA, Arif E, Kolmetzky DW, Tomar D, Luongo TS, Jadiya P, Murray EK, Lorkiewicz PK, Hajnóczky G, et al. Mitochondrial calcium exchange links metabolism with the epigenome to control cellular differentiation. Nature communications. 2019; 10(1):1–17.

López-Otín C, Blasco MA, Partridge L, Serrano M, Kroemer G. The hallmarks of aging. Cell. 2013; 153(6):1194–1217.

López-Otín C, Blasco MA, Partridge L, Serrano M, Kroemer G. The Hallmarks of Aging. Cell. 2013; 153(6):1194–1217.

López-Otín C, Galluzzi L, Freije JM, Madeo F, Kroemer G. Metabolic control of longevity. Cell. 2016; 166(4):802–821.

Love MI, Huber W, Anders S. Moderated estimation of fold change and dispersion for RNA-seq data with DESeq2. Genome biology. 2014; 15(12):550.

Lu C, Thompson CB. Metabolic regulation of epigenetics. Cell metabolism. 2012; 16(1):9–17.

Lucena MC, Carvalho-Cruz P, Donadio JL, Oliveira IA, de Queiroz RM, Marinho-Carvalho MM, Sola-Penna M, de Paula IF, Gondim KC, McComb ME, et al. Epithelial mesenchymal transition induces aberrant glycosylation through hexosamine biosynthetic pathway activation. Journal of Biological Chemistry. 2016; 291(25):12917–12929.

bioRxiv preprint doi: https://doi.org/10.1101/2021.05.03.442497; this version posted November 12, 2021. The copyright holder for this preprint (which was not certified by peer review) is the author/funder. All rights reserved. No reuse allowed without permission.

Ma S, Meng Z, Chen R, Guan KL. The Hippo pathway: biology and pathophysiology. Annual review of biochemistry. 2019; 88:577–604.

Macieira-Coelho A, Azzarone B. Aging of human fibroblasts is a succession of subtle changes in the cell cycle and has a final short stage with abrupt events. Experimental Cell Research. 1982; 141(2):325–332.

Mahmoudi S, Mancini E, Xu L, Moore A, Jahanbani F, Hebestreit K, Srinivasan R, Li X, Devarajan K, Prélot L, et al. Heterogeneity in old fibroblasts is linked to variability in reprogramming and wound healing. Nature. 2019; 574(7779):553–558.

Mascharak S, Davitt MF, Griffin M, Borrelli MR, Moore AL, Chen K, Duoto B, Chinta M, Foster DS, Shen AH, et al. Preventing Engrailed-1 activation in fibroblasts yields wound regeneration without scarring. Science. 2021; 372(6540).

McInnes L, Healy J, Melville J. Umap: Uniform manifold approximation and projection for dimension reduction. arXiv preprint arXiv:180203426. 2018; .

Mellone M, Hanley CJ, Thirdborough S, Mellows T, Garcia E, Woo J, Tod J, Frampton S, Jenei V, Moutasim KA, Kabir TD, Brennan PA, Venturi G, Ford K, Herranz N, Lim KP, Clarke J, Lambert DW, Prime SS, Underwood TJ, et al. Induction of fibroblast senescence generates a non-fibrogenic myofibroblast phenotype that differentially impacts on cancer prognosis. Aging. 2016 Dec; 9(1):114–132.

Meyerson M, Counter CM, Eaton EN, Ellisen LW, Steiner P, Caddle SD, Ziaugra L, Beijersbergen RL, Davidoff MJ, Liu Q, Bacchetti S, Haber DA, Weinberg RA. hEST2, the putative human telomerase catalytic subunit gene, is up-regulated in tumor cells and during immortalization. Cell. 1997 Aug; 90(4):785–795.

Mootha VK, Lindgren CM, Eriksson KF, Subramanian A, Sihag S, Lehar J, Puigserver P, Carlsson E, Ridderstråle M, Laurila E, et al. PGC-1α-responsive genes involved in oxidative phosphorylation are coordinately downregulated in human diabetes. Nature genetics. 2003; 34(3):267–273.

Nassrally MS, Lau A, Wise K, John N, Kotecha S, Lee KL, Brooks RF. Cell cycle arrest in replicative senescence is not an immediate consequence of telomere dysfunction. Mechanisms of ageing and development. 2019; 179:11–22.

Nestorowa S, Hamey FK, Pijuan Sala B, Diamanti E, Shepherd M, Laurenti E, Wilson NK, Kent DG, Göttgens B. A single-cell resolution map of mouse hematopoietic stem and progenitor cell differentiation. Blood. 2016 Aug; 128(8):e20–31.

Neurohr GE, Terry RL, Lengefeld J, Bonney M, Brittingham GP, Moretto F, Miettinen TP, Vaites LP, Soares LM, Paulo JA, et al. Excessive cell growth causes cytoplasm dilution and contributes to senescence. Cell. 2019; 176(5):1083–1097.

Ogrodnik M. Cellular aging beyond cellular senescence: Markers of senescence prior to cell cycle arrest in vitro and in vivo. Aging Cell. 2021; 20(4):e13338.

Ogrodnik M, Miwa S, Tchkonia T, Tiniakos D, Wilson CL, Lahat A, Day CP, Burt A, Palmer A, Anstee QM, et al. Cellular senescence drives age-dependent hepatic steatosis. Nature communications. 2017; 8(1):1–12.

Ogrodnik M, Salmonowicz H, Jurk D, Passos JF. Expansion and cell-cycle arrest: common denominators of cellular senescence. Trends in biochemical sciences. 2019; 44(12):996–1008.

O'Brien JJ, O'Connell JD, Paulo JA, Thakurta S, Rose CM, Weekes MP, Huttlin EL, Gygi SP. Compositional proteomics: effects of spatial constraints on protein quantification utilizing isobaric tags. Journal of proteome research. 2018; 17(1):590–599.

Passos JF, Saretzki G, Ahmed S, Nelson G, Richter T, Peters H, Wappler I, Birket MJ, Harold G, Schaeuble K, Birch-Machin MA, Kirkwood TBL, von Zglinicki T. Mitochondrial dysfunction accounts for the stochastic heterogeneity in telomere-dependent senescence. PLoS Biol. 2007 May; 5(5):e110.

Patro R, Duggal G, Love MI, Irizarry RA, Kingsford C. Salmon provides fast and bias-aware quantification of transcript expression. Nat Methods. 2017 Apr; 14(4):417–419.

Peng C, Zhu Y, Zhang W, Liao Q, Chen Y, Zhao X, Guo Q, Shen P, Zhen B, Qian X, et al. Regulation of the hippo-YAP pathway by glucose sensor O-GlcNAcylation. Molecular cell. 2017; 68(3):591–604.

bioRxiv preprint doi: https://doi.org/10.1101/2021.05.03.442497; this version posted November 12, 2021. The copyright holder for this preprint (which was not certified by peer review) is the author/funder. All rights reserved. No reuse allowed without permission.

Pereira JS, da Silva JG, Tomaz RA, Pinto AE, Bugalho MJ, Leite V, Cavaco BM. Identification of a novel germline FOXE1 variant in patients with familial non-medullary thyroid carcinoma (FNMTC). Endocrine. 2015 May; 49(1):204–214.

Phan SH. Biology of fibroblasts and myofibroblasts. Proceedings of the American Thoracic Society. 2008; 5(3):334–337.

Piccolo S, Dupont S, Cordenonsi M. The biology of YAP/TAZ: hippo signaling and beyond. Physiological reviews. 2014; .

Piersma B, de Rond S, Werker PMN, Boo S, Hinz B, van Beuge MM, Bank RA. YAP1 Is a Driver of Myofibroblast Differentiation in Normal and Diseased Fibroblasts. Am J Pathol. 2015 Dec; 185(12):3326–3337.

Pignolo RJ, Passos JF, Khosla S, Tchkonia T, Kirkland JL. Reducing senescent cell burden in aging and disease. Trends in molecular medicine. 2020; 26(7):630–638.

Pissios P. Nicotinamide N-methyltransferase: more than a vitamin B3 clearance enzyme. Trends in Endocrinology & Metabolism. 2017; 28(5):340–353.

Qin Q, Fan J, Zheng R, Wan C, Mei S, Wu Q, Sun H, Brown M, Zhang J, Meyer CA, Liu XS. Lisa: inferring transcriptional regulators through integrative modeling of public chromatin accessibility and ChIP-seq data. Genome Biol. 2020 Feb; 21(1):32.

Qiu X, Mao Q, Tang Y, Wang L, Chawla R, Pliner HA, Trapnell C. Reversed graph embedding resolves complex single-cell trajectories. Nat Methods. 2017 Oct; 14(10):979–982.

Raghu G, Weycker D, Edelsberg J, Bradford WZ, Oster G. Incidence and prevalence of idiopathic pulmonary fibrosis. American journal of respiratory and critical care medicine. 2006; 174(7):810–816.

Rappsilber J, Mann M, Ishihama Y. Protocol for micro-purification, enrichment, pre-fractionation and storage of peptides for proteomics using StageTips. Nature protocols. 2007; 2(8):1896.

Razdan N, Vasilopoulos T, Herbig U. Telomere dysfunction promotes transdifferentiation of human fibroblasts into myofibroblasts. Aging Cell. 2018 Dec; 17(6):e12838.

Ribeiro SMF, Poczatek M, Schultz-Cherry S, Villain M, Murphy-Ullrich JE. The Activation Sequence of Thrombospondin-1 Interacts with the Latency-associated Peptide to Regulate Activation of Latent Transforming Growth Factor-β. Journal of Biological Chemistry. 1999; 274(19):13586–13593.

Ritchie ME, Phipson B, Wu D, Hu Y, Law CW, Shi W, Smyth GK. limma powers differential expression analyses for RNA-sequencing and microarray studies. Nucleic acids research. 2015; 43(7):e47–e47.

Rogers JM, Waters CT, Seegar TCM, Jarrett SM, Hallworth AN, Blacklow SC, Bulyk ML. Bispecific Forkhead Transcription Factor FoxN3 Recognizes Two Distinct Motifs with Different DNA Shapes. Mol Cell. 2019 Apr; 74(2):245–253.e6.

Sabbineni H, Verma A, Somanath PR. Isoform-specific effects of transforming growth factor β on endothelial-to-mesenchymal transition. Journal of cellular physiology. 2018; 233(11):8418–8428.

Sadaie M, Salama R, Carroll T, Tomimatsu K, Chandra T, Young ARJ, Narita M, Pérez-Mancera PA, Bennett DC, Chong H, Kimura H, Narita M. Redistribution of the Lamin B1 genomic binding profile affects rearrangement of heterochromatic domains and SAHF formation during senescence. Genes Dev. 2013 Aug; 27(16):1800–1808.

Sahai E, Astsaturov I, Cukierman E, DeNardo DG, Egeblad M, Evans RM, Fearon D, Greten FR, Hingorani SR, Hunter T, et al. A framework for advancing our understanding of cancer-associated fibroblasts. Nature Reviews Cancer. 2020; 20(3):174–186.

Sedelnikova OA, Horikawa I, Zimonjic DB, Popescu NC, Bonner WM, Barrett JC. Senescing human cells and ageing mice accumulate DNA lesions with unrepairable double-strand breaks. Nature cell biology. 2004; 6(2):168–170.

Shin W, Rosin NL, Sparks H, Sinha S, Rahmani W, Sharma N, Workentine M, Abbasi S, Labit E, Stratton JA, Biernaskie J. Dysfunction of Hair Follicle Mesenchymal Progenitors Contributes to Age-Associated Hair Loss. Developmental Cell. 2020; 53(2):185–198.e7. https://www.sciencedirect.com/science/article/pii/S1534580720302318, doi: https://doi.org/10.1016/j.devcel.2020.03.019.

bioRxiv preprint doi: https://doi.org/10.1101/2021.05.03.442497; this version posted November 12, 2021. The copyright holder for this preprint (which was not certified by peer review) is the author/funder. All rights reserved. No reuse allowed without permission.

Smith JR, Whitney RG. Intraclonal variation in proliferative potential of human diploid fibroblasts: stochastic mechanism for cellular aging. Science. 1980 Jan; 207(4426):82–84.

de Sousa N, Rodríguez-Esteban G, Rojo-Laguna JI, Saló E, Adell T. Hippo signaling controls cell cycle and restricts cell plasticity in planarians. PLoS biology. 2018; 16(1):e2002399.

Sperber H, Mathieu J, Wang Y, Ferreccio A, Hesson J, Xu Z, Fischer KA, Devi A, Detraux D, Gu H, et al. The metabolome regulates the epigenetic landscape during naive-to-primed human embryonic stem cell transition. Nature cell biology. 2015; 17(12):1523–1535.

Strunz M, Simon LM, Ansari M, Kathiriya JJ, Angelidis I, Mayr CH, Tsidiridis G, Lange M, Mattner LF, Yee M, Ogar P, Sengupta A, Kukhtevich I, Schneider R, Zhao Z, Voss C, Stoeger T, Neumann JHL, Hilgendorff A, Behr J, et al. Alveolar regeneration through a Krt8+ transitional stem cell state that persists in human lung fibrosis. Nat Commun. 2020 Jul; 11(1):3559.

Stuart BD, Choi J, Zaidi S, Xing C, Holohan B, Chen R, Choi M, Dharwadkar P, Torres F, Girod CE, et al. Exome sequencing links mutations in PARN and RTEL1 with familial pulmonary fibrosis and telomere shortening. Nature genetics. 2015; 47(5):512–517.

Stuart BD, Lee JS, Kozlitina J, Noth I, Devine MS, Glazer CS, Torres F, Kaza V, Girod CE, Jones KD, et al. Effect of telomere length on survival in patients with idiopathic pulmonary fibrosis: an observational cohort study with independent validation. The lancet Respiratory medicine. 2014; 2(7):557–565.

Stuart T, Butler A, Hoffman P, Hafemeister C, Papalexi E, III WMM, Hao Y, Stoeckius M, Smibert P, Satija R. Comprehensive Integration of Single-Cell Data. Cell. 2019; 177:1888–1902. https://doi.org/10.1016/j.cell.2019.05.031, doi: 10.1016/j.cell.2019.05.031.

Subramanian A, Tamayo P, Mootha VK, Mukherjee S, Ebert BL, Gillette MA, Paulovich A, Pomeroy SL, Golub TR, Lander ES, et al. Gene set enrichment analysis: a knowledge-based approach for interpreting genome-wide expression profiles. Proceedings of the National Academy of Sciences. 2005; 102(43):15545–15550.

Tang H, Geng A, Zhang T, Wang C, Jiang Y, Mao Z. Single senescent cell sequencing reveals heterogeneity in senescent cells induced by telomere erosion. Protein & cell. 2019; 10(5):370–375.

Tang Y, Feinberg T, Keller ET, Li XY, Weiss SJ. Snail/Slug binding interactions with YAP/TAZ control skeletal stem cell self-renewal and differentiation. Nat Cell Biol. 2016 Sep; 18(9):917–929.

Ting L, Rad R, Gygi SP, Haas W. MS3 eliminates ratio distortion in isobaric multiplexed quantitative proteomics. Nature methods. 2011; 8(11):937–940.

Traag VA, Waltman L, van Eck NJ. From Louvain to Leiden: guaranteeing well-connected communities. Scientific reports. 2019; 9(1):1–12.

Trapnell C, Cacchiarelli D, Grimsby J, Pokharel P, Li S, Morse M, Lennon NJ, Livak KJ, Mikkelsen TS, Rinn JL. The dynamics and regulators of cell fate decisions are revealed by pseudotemporal ordering of single cells. Nat Biotechnol. 2014 Apr; 32(4):381–386.

Tsakiri KD, Cronkhite JT, Kuan PJ, Xing C, Raghu G, Weissler JC, Rosenblatt RL, Shay JW, Garcia CK. Adult-onset pulmonary fibrosis caused by mutations in telomerase. Proc Natl Acad Sci U S A. 2007 May; 104(18):7552–7557.

Ulanovskaya OA, Zuhl AM, Cravatt BF. NNMT promotes epigenetic remodeling in cancer by creating a metabolic methylation sink. Nature chemical biology. 2013; 9(5):300–306.

Unterluggauer H, Mazurek S, Lener B, Hütter E, Eigenbrodt E, Zwerschke W, Jansen-Dürr P. Premature senescence of human endothelial cells induced by inhibition of glutaminase. Biogerontology. 2008; 9(4):247–259.

Vassilev A, Kaneko KJ, Shu H, Zhao Y, DePamphilis ML. TEAD/TEF transcription factors utilize the activation domain of YAP65, a Src/Yes-associated protein localized in the cytoplasm. Genes Dev. 2001 May; 15(10):1229–1241.

Venza I, Visalli M, Parrillo L, De Felice M, Teti D, Venza M. MSX1 and TGF-beta3 are novel target genes functionally regulated by FOXE1. Hum Mol Genet. 2011 Mar; 20(5):1016–1025.

Victorelli S, Passos JF. Telomeres and Cell Senescence - Size Matters Not. EBioMedicine. 2017 Jul; 21:14–20.

Wagner V, Gil J, T cells engineered to target senescence. Nature Publishing Group; 2020.

bioRxiv preprint doi: https://doi.org/10.1101/2021.05.03.442497; this version posted November 12, 2021. The copyright holder for this preprint (which was not certified by peer review) is the author/funder. All rights reserved. No reuse allowed without permission.

Walker EJ, Heydet D, Veldre T, Ghildyal R. Transcriptomic changes during TGF-β-mediated differentiation of airway fibroblasts to myofibroblasts. Scientific reports. 2019; 9(1):1–14.

Wang C, Zhu X, Feng W, Yu Y, Jeong K, Guo W, Lu Y, Mills GB. Verteporfin inhibits YAP function through up-regulating 14-3-3σ sequestering YAP in the cytoplasm. American journal of cancer research. 2016; 6(1):27.

Weirauch MT, Yang A, Albu M, Cote AG, Montenegro-Montero A, Drewe P, Najafabadi HS, Lambert SA, Mann I, Cook K, et al. Determination and inference of eukaryotic transcription factor sequence specificity. Cell. 2014; 158(6):1431–1443.

Whitney R, et al. Intraclonal variation in proliferative potential of human diploid fibroblasts: stochastic mechanism for cellular aging. Science. 1980; 207(4426):82–84.

Wiley CD, Flynn JM, Morrissey C, Lebofsky R, Shuga J, Dong X, Unger MA, Vijg J, Melov S, Campisi J. Analysis of individual cells identifies cell-to-cell variability following induction of cellular senescence. Aging cell. 2017; 16(5):1043–1050.

Wirka RC, Wagh D, Paik DT, Pjanic M, Nguyen T, Miller CL, Kundu R, Nagao M, Coller J, Koyano TK, et al. Atheroprotective roles of smooth muscle cell phenotypic modulation and the TCF21 disease gene as revealed by single-cell analysis. Nature medicine. 2019; 25(8):1280–1289.

Xie Q, Chen J, Feng H, Peng S, Adams U, Bai Y, Huang L, Li J, Huang J, Meng S, Yuan Z. YAP/TEAD–Mediated Transcription Controls Cellular Senescence. Cancer Research. 2013; 73(12):3615–3624.

Xu Y, Mizuno T, Sridharan A, Du Y, Guo M, Tang J, Wikenheiser-Brokamp KA, Perl AKT, Funari VA, Gokey JJ, Stripp BR, Whitsett JA. Single-cell RNA sequencing identifies diverse roles of epithelial cells in idiopathic pulmonary fibrosis. JCI Insight. 2016 Dec; 1(20):e90558.

Xu Z, Duc KD, Holcman D, Teixeira MT. The length of the shortest telomere as the major determinant of the onset of replicative senescence. Genetics. 2013 Aug; 194(4):847–857.

Yanai H, Shteinberg A, Porat Z, Budovsky A, Braiman A, Zeische R, Fraifeld VE. Cellular senescence-like features of lung fibroblasts derived from idiopathic pulmonary fibrosis patients. Aging (Albany NY). 2015; 7(9):664.

Yousefzadeh MJ, Zhao J, Bukata C, Wade EA, McGowan SJ, Angelini LA, Bank MP, Gurkar AU, McGuckian CA, Calubag MF, Kato JI, Burd CE, Robbins PD, Niedernhofer LJ. Tissue specificity of senescent cell accumulation during physiologic and accelerated aging of mice. Aging Cell. 2020 Mar; 19(3):e13094.

Yu FX, Zhao B, Guan KL. Hippo Pathway in Organ Size Control, Tissue Homeostasis, and Cancer. Cell. 2015; 163(4):811–828.

Zhang H, Liu CY, Zha ZY, Zhao B, Yao J, Zhao S, Xiong Y, Lei QY, Guan KL. TEAD transcription factors mediate the function of TAZ in cell growth and epithelial-mesenchymal transition. Journal of biological chemistry. 2009; 284(20):13355–13362.

Zhang K, Rekhter MD, Gordon D, Phan SH. Myofibroblasts and their role in lung collagen gene expression during pulmonary fibrosis. A combined immunohistochemical and in situ hybridization study. Am J Pathol. 1994 Jul; 145(1):114–125.

Zhang X, Qiao Y, Wu Q, Chen Y, Zou S, Liu X, Zhu G, Zhao Y, Chen Y, Yu Y, et al. The essential role of YAP O-GlcNAcylation in high-glucose-stimulated liver tumorigenesis. Nature communications. 2017; 8(1):1–15.

Zhang Y, Liu T, Meyer CA, Eeckhoute J, Johnson DS, Bernstein BE, Nusbaum C, Myers RM, Brown M, Li W, et al. Model-based analysis of ChIP-Seq (MACS). Genome biology. 2008; 9(9):1–9.

Zhang Y, Parmigiani G, Johnson WE. ComBat-seq: batch effect adjustment for RNA-seq count data. NAR Genomics and Bioinformatics. 2020 09; 2(3). https://doi.org/10.1093/nargab/lqaa078, doi: 10.1093/nargab/lqaa078, lqaa078.

Zhao B, Ye X, Yu J, Li L, Li W, Li S, Yu J, Lin JD, Wang CY, Chinnaiyan AM, et al. TEAD mediates YAP-dependent gene induction and growth control. Genes & development. 2008; 22(14):1962–1971.

Zwerschke W, Mazurek S, Stöckl P, Hütter E, Eigenbrodt E, Jansen-Dürr P. Metabolic analysis of senescent human fibroblasts reveals a role for AMP in cellular senescence. Biochemical journal. 2003; 376(2):403–411.

bioRxiv preprint doi: https://doi.org/10.1101/2021.05.03.442497; this version posted November 12, 2021. The copyright holder for this preprint (which was not certified by peer review) is the author/funder. All rights reserved. No reuse allowed without permission.

				BATCH A					BATCH B	
	PDL20	PDL25	PDL29	PDL33	PDL37	PDL46	PDL50	PDL45	PDL52	PDL53
bulk RNA sec	X	X	X	X	X	X	X	X	X	X
scRNA seq		X	X	X	X	X	X			
proteomics	X	X	X	X	X	X	X			
metabalomics		X	X	X	X	X	X			
ATAC	X	X	X	X	X	X	X			
	TP1	TP2	TP3	TP4	TP5	TP6	TP7			
bulk RNA sec	X	X		X	X	X	X			
scRNA seq		X					X			
proteomics	X	X		X	X	X	X			
metabalomics		X		X	X	X	X			
ATAC	X	X		X	X	X	X			

Figure 1–Figure supplement 1. Sample manifest for WT and hTERT WI-38 cells.

bioRxiv preprint doi: https://doi.org/10.1101/2021.05.03.442497; this version posted November 12, 2021. The copyright holder for this preprint (which was not certified by peer review) is the author/funder. All rights reserved. No reuse allowed without permission.

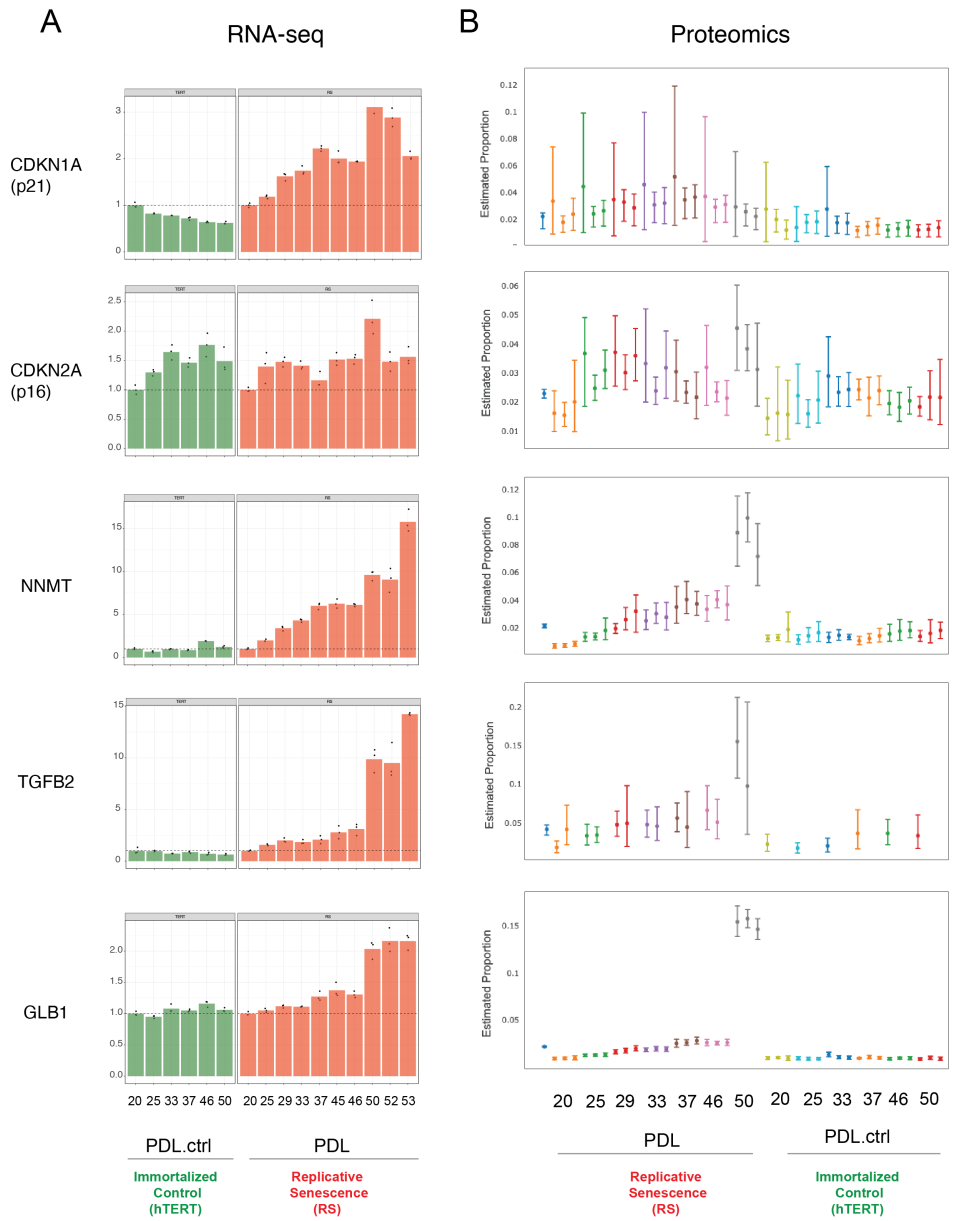

Figure 1–Figure supplement 2. Expression of canonical and novel senescence induced genes **(A)** RNA-seq quantification for p21, p16, NNMT, TGFB2, and GLB1 (beta-galactosidase) transcripts expressed as fold change relative to reference sample: PDL 20 for WT replicative senescence and PDL.ctrl 20 for hTERT. Bar height represents replicate average (n=3) and each point is an individual sample. **(B)** Proteomics quantification for same genes as in A. Estimates of relative protein abundance are provided as proportions of one biological replicate (n=3) relative to the total abundance observed across all other replicates in the experiment. This is obtained across multiple plexes with a Bayesian modeling of the intensities as log2 ratios to a bridge channel (blue sample far left). Protein level estimates from these models are then transformed with the inverse additive log-ratio transformation, resulting in a posterior distribution in proportion space.

bioRxiv preprint doi: https://doi.org/10.1101/2021.05.03.442497; this version posted November 12, 2021. The copyright holder for this preprint (which was not certified by peer review) is the author/funder. All rights reserved. No reuse allowed without permission.

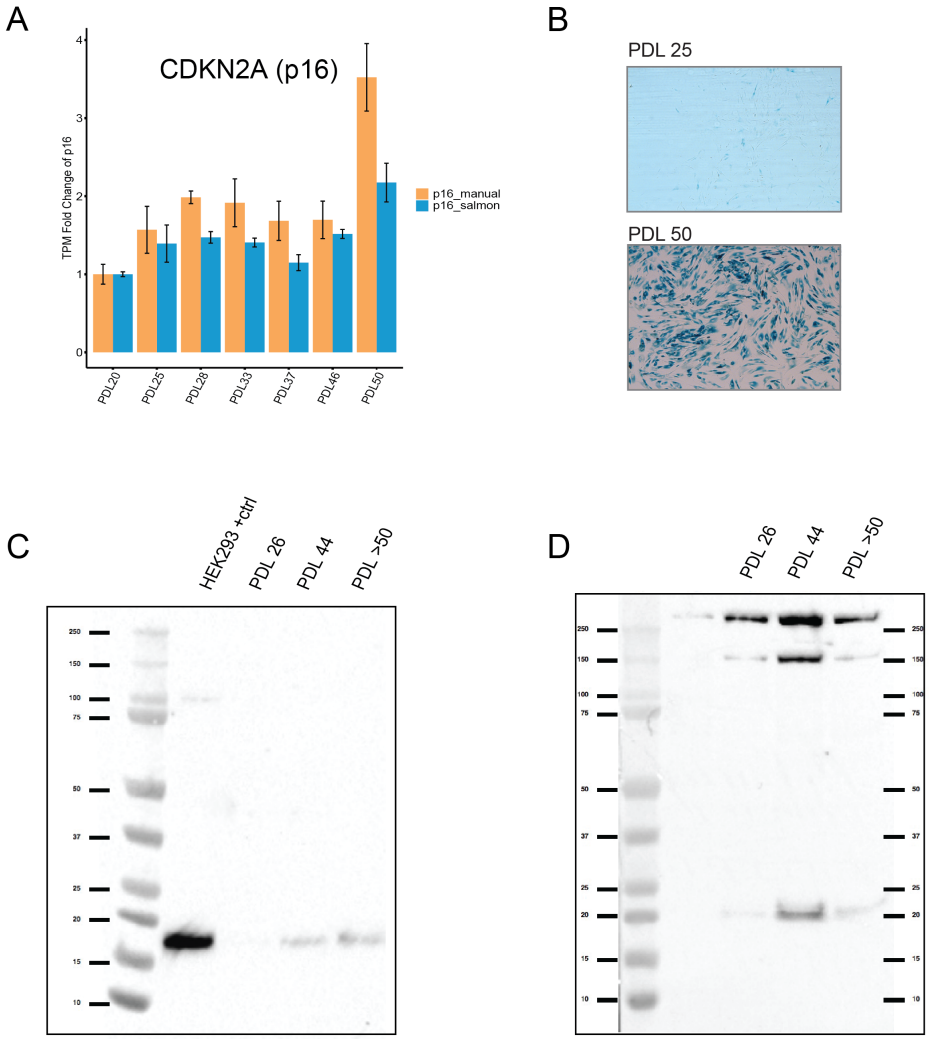

Figure 1–Figure supplement 3. Senescent WI-38 cells express classic senescence markers. **(A)** Quantification of p16 and p14 gene products from the CDKN1A locus. Values plotted are fold change levels relative to PDL 20. TPM values generated by Salmon using the gencode v29 annotation set that includes p16 and p14 in one locus (blue). A manual summation of the p16 only transcripts in the locus are shown (orange). Error bars represent the standard deviation of three samples. **(B)** Representative images for senescence-associated beta-galactosidase assay. **(C)** Western blot for p16 at three PDLs (26, 44 and >50). Far left lane is p16 positive control derived from HEK293 cells. **(D)** Western blot for p21 at three PDLs (26, 44 and >50). Far left lane is p21 negative control derived from HEK293 cells.

bioRxiv preprint doi: https://doi.org/10.1101/2021.05.03.442497; this version posted November 12, 2021. The copyright holder for this preprint (which was not certified by peer review) is the author/funder. All rights reserved. No reuse allowed without permission.

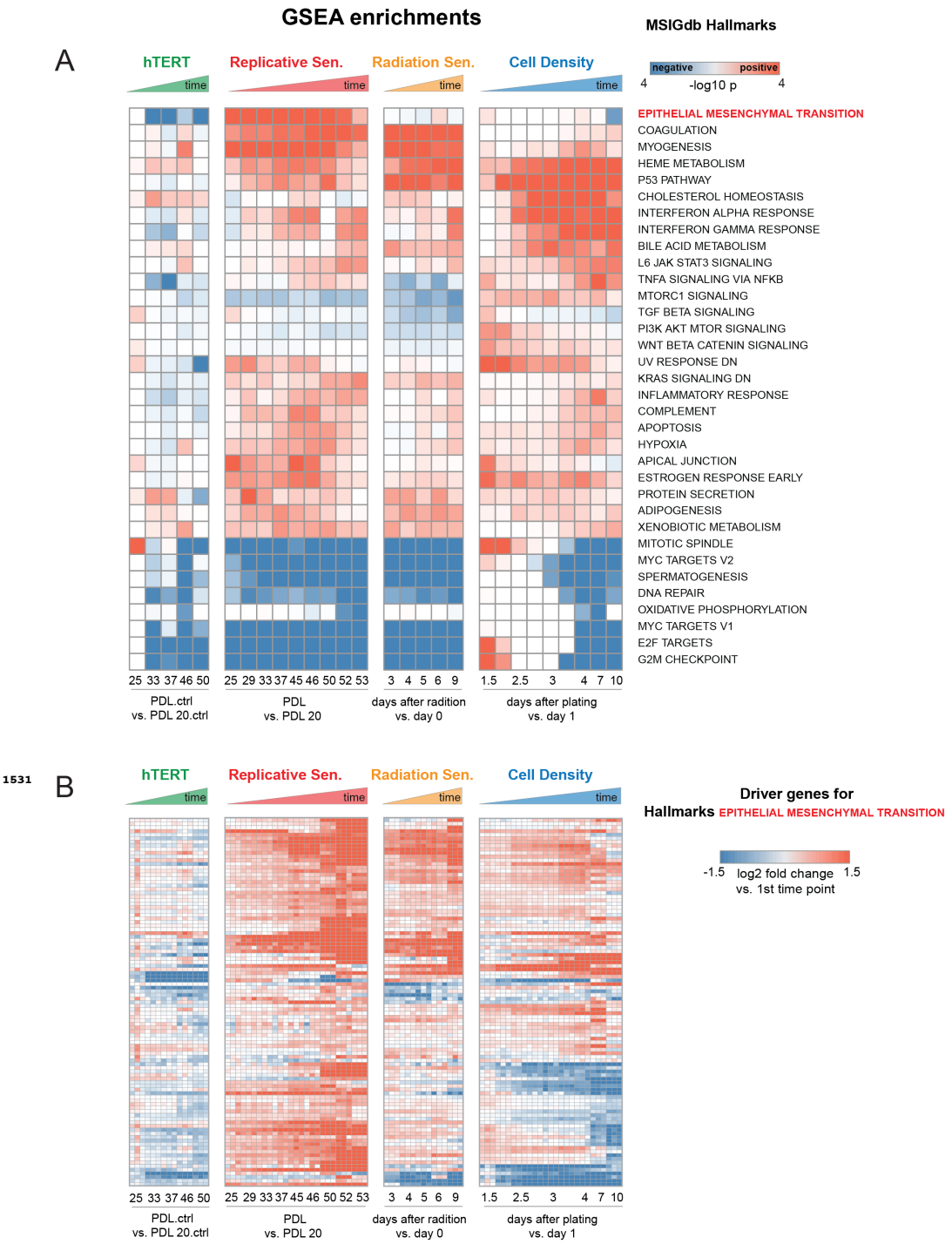

Figure 1–Figure supplement 4. Enrichment and induction of Epithelial to Mesenchymal Transition gene set during approach to replicative senescence. **(A)** GSEA was run using MSsigDB Hallmark gene sets. Data used for ranked list was the log2 fold changes at each time point vs. first the initial time point for each condition as indicated in B (i.e. PDL 20 for replicative senescence). Color indicates -log10 Benjamini-Hochberg p-value and direction of change e.g. red=enriched in up-regulated genes, blue=enriched in down-regulated genes. Epithelial to Mesenchymal Transition is highlighted in red.**(B)** Heatmap of 150 leading edge genes driving GSEA enrichment of EMT annotation compiled from all timepoints. Values are the log2 fold changes at each time point vs. first the initial time point for each condition as indicated. Values are individual (n=3) replicate samples.

bioRxiv preprint doi: https://doi.org/10.1101/2021.05.03.442497; this version posted November 12, 2021. The copyright holder for this preprint (which was not certified by peer review) is the author/funder. All rights reserved. No reuse allowed without permission.

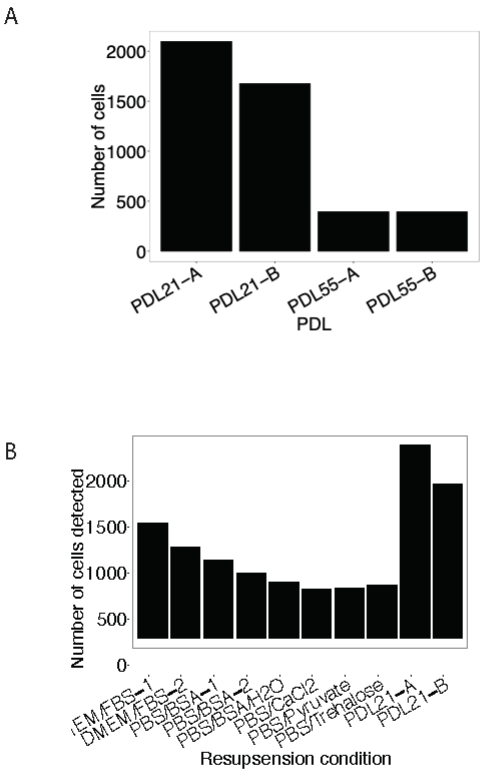

1532

Figure 2–Figure supplement 1. Using a modified resuspension buffer of DMEM+FBS increases detection of senescent cells with the 10x Genomics 3' single cell RNA-seq protocol. **(A)** Barplot comparing the number of cells detected (y-axis) as a function of the age of cells (x-axis). **(B)** Barplot representing the number of cells detected (y-axis) with various cell resuspension buffers. (y-axis).

bioRxiv preprint doi: https://doi.org/10.1101/2021.05.03.442497; this version posted November 12, 2021. The copyright holder for this preprint (which was not certified by peer review) is the author/funder. All rights reserved. No reuse allowed without permission.

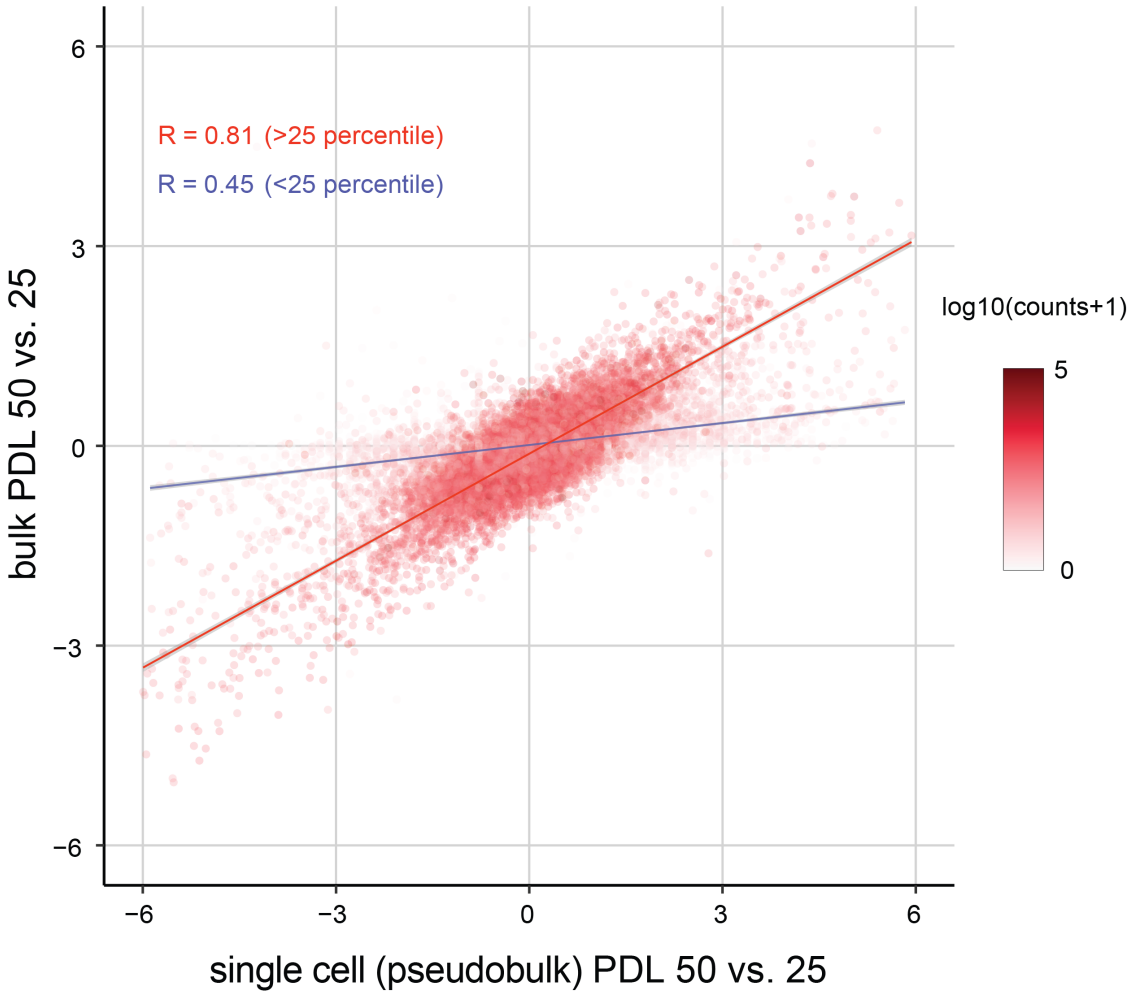

Figure 2–Figure supplement 2. Replicative senescence dependent gene expression changes measured by Bulk RNA-seq and single cell RNA-seq are highly concordant. Scatterplot comparing the log2 fold changes of PDL 50 vs PDL 25 measured using single cell pseudo-bulk count summations (x-axis) and actual bulk RNA-seq (y-axis). The color for each gene is the log10 normalized counts. The r for all genes is 0.77. The r for genes filtered at > 25th percentile is 0.81 (red line) and 0.45 for genes < 25th percentile (blue line) .

bioRxiv preprint doi: https://doi.org/10.1101/2021.05.03.442497; this version posted November 12, 2021. The copyright holder for this preprint (which was not certified by peer review) is the author/funder. All rights reserved. No reuse allowed without permission.

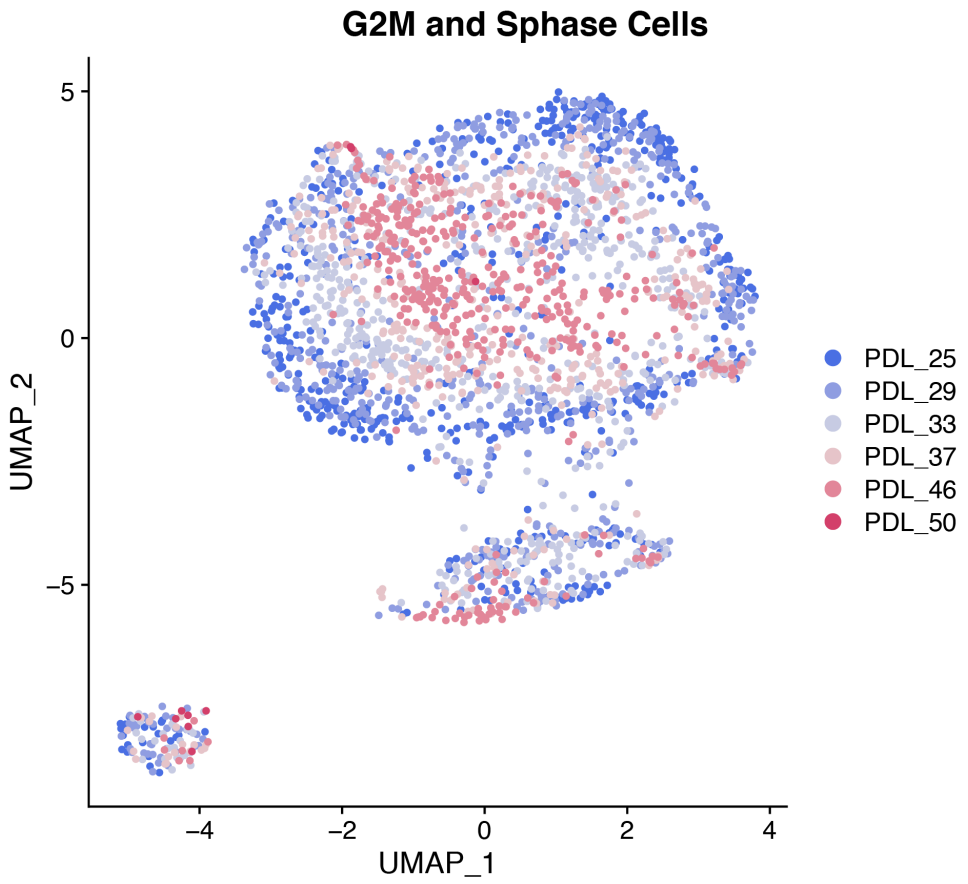

Figure 2–Figure supplement 3. Single cell UMAPs of high mitotic scoring (gene set) WI-38 cells. S phase and G2M scored cells were separated and reprocessed and visualized with a UMAP projection. In mitotic cells, PDL is the primary source of variance across all PDLs.

bioRxiv preprint doi: https://doi.org/10.1101/2021.05.03.442497; this version posted November 12, 2021. The copyright holder for this preprint (which was not certified by peer review) is the author/funder. All rights reserved. No reuse allowed without permission.

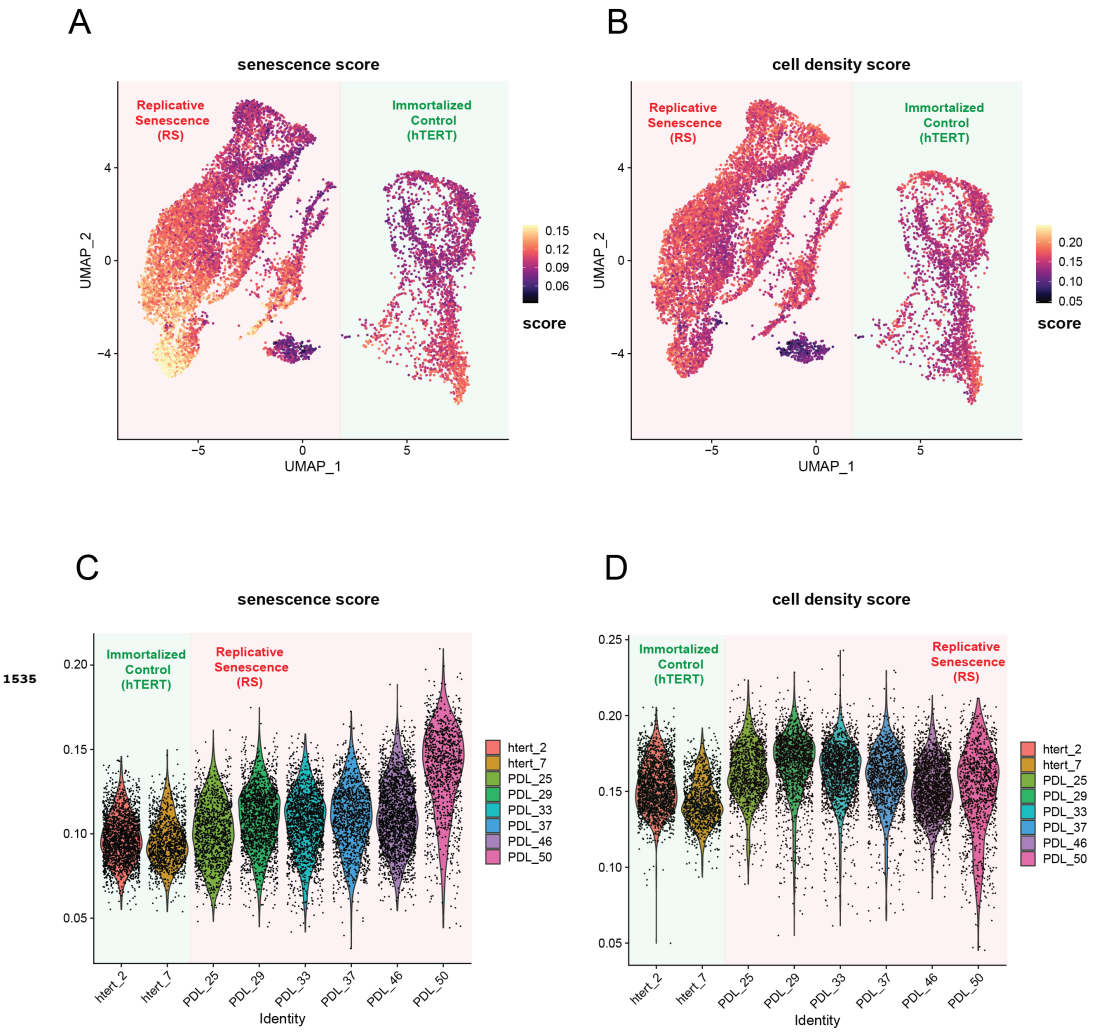

1535

Figure 2–Figure supplement 4. WT and hTERT WI-38 cells scored for senescence and cell density signatures. **(A)** UMAP projection of WT and hTERT single cell RNA-seq scored with a signature composed of significantly increasing genes with replicative senescence that are not significant in cell density experiments derived from bulk RNA-seq. Yellow represents cells scoring high, while black depicts cells scoring low for the senescence score. **(B)** As in A but scored for unique cell density signature. **(C)** Violin plot of cells scored as in A. Y-axis is the score assigned to each cell (point). Each PDL and hTERT PDL.ctrl asr on x-axis. Senescence score increases with PDL. **(D)** Violin plot of cells scored as in B for cell density. Y-axis is the score assigned to each cell (point). Each PDL and hTERT PDL.ctrl on x-axis. Cell density remains flat with increasing PDL.

bioRxiv preprint doi: https://doi.org/10.1101/2021.05.03.442497; this version posted November 12, 2021. The copyright holder for this preprint (which was not certified by peer review) is the author/funder. All rights reserved. No reuse allowed without permission.

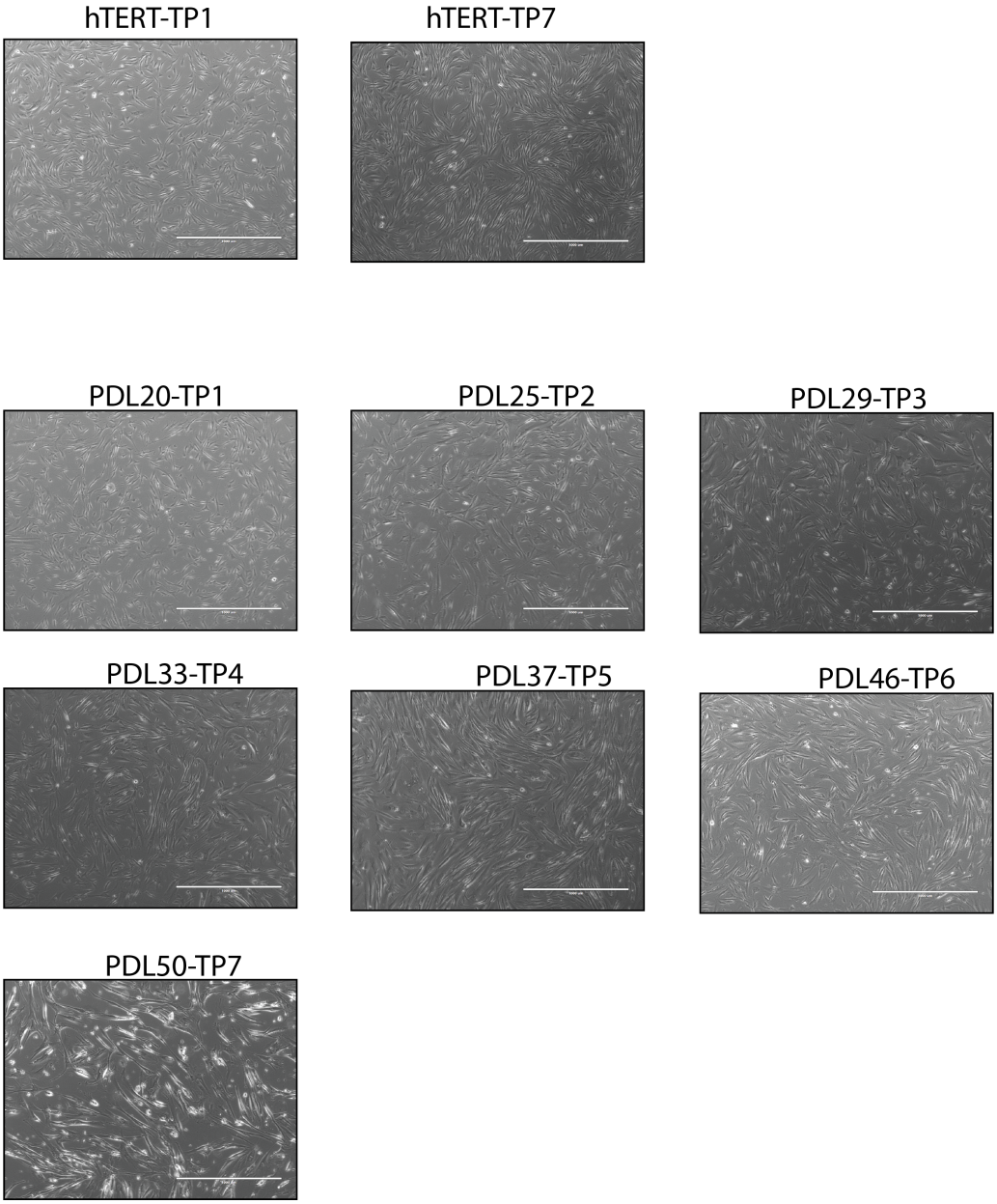

Figure 2–Figure supplement 5. Representative images of WI-38 cells at collection time points.

bioRxiv preprint doi: https://doi.org/10.1101/2021.05.03.442497; this version posted November 12, 2021. The copyright holder for this preprint (which was not certified by peer review) is the author/funder. All rights reserved. No reuse allowed without permission.

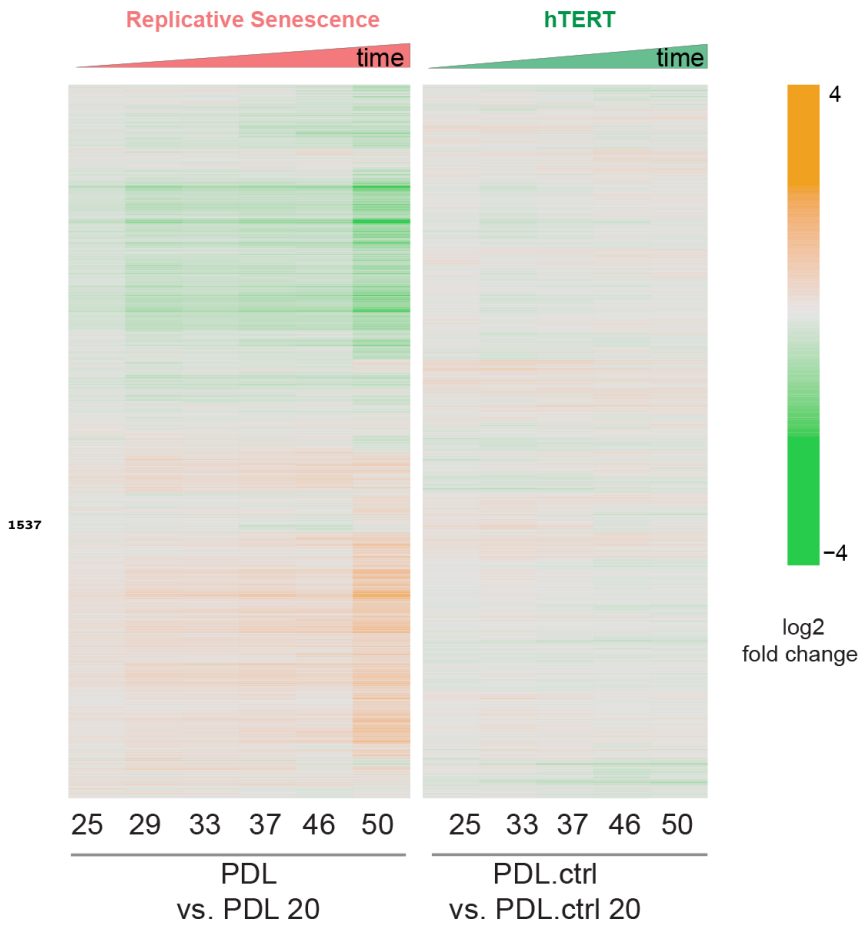

Figure 3–Figure supplement 1. Heatmap of hierarchical clustering of 8000 protein log2 fold changes at each time point/PDL versus first (not shown) for RS WT WI-38 (left) and hTERT WI-38 cells (right) from high induction (orange) to depletion (green).

bioRxiv preprint doi: https://doi.org/10.1101/2021.05.03.442497; this version posted November 12, 2021. The copyright holder for this preprint (which was not certified by peer review) is the author/funder. All rights reserved. No reuse allowed without permission.

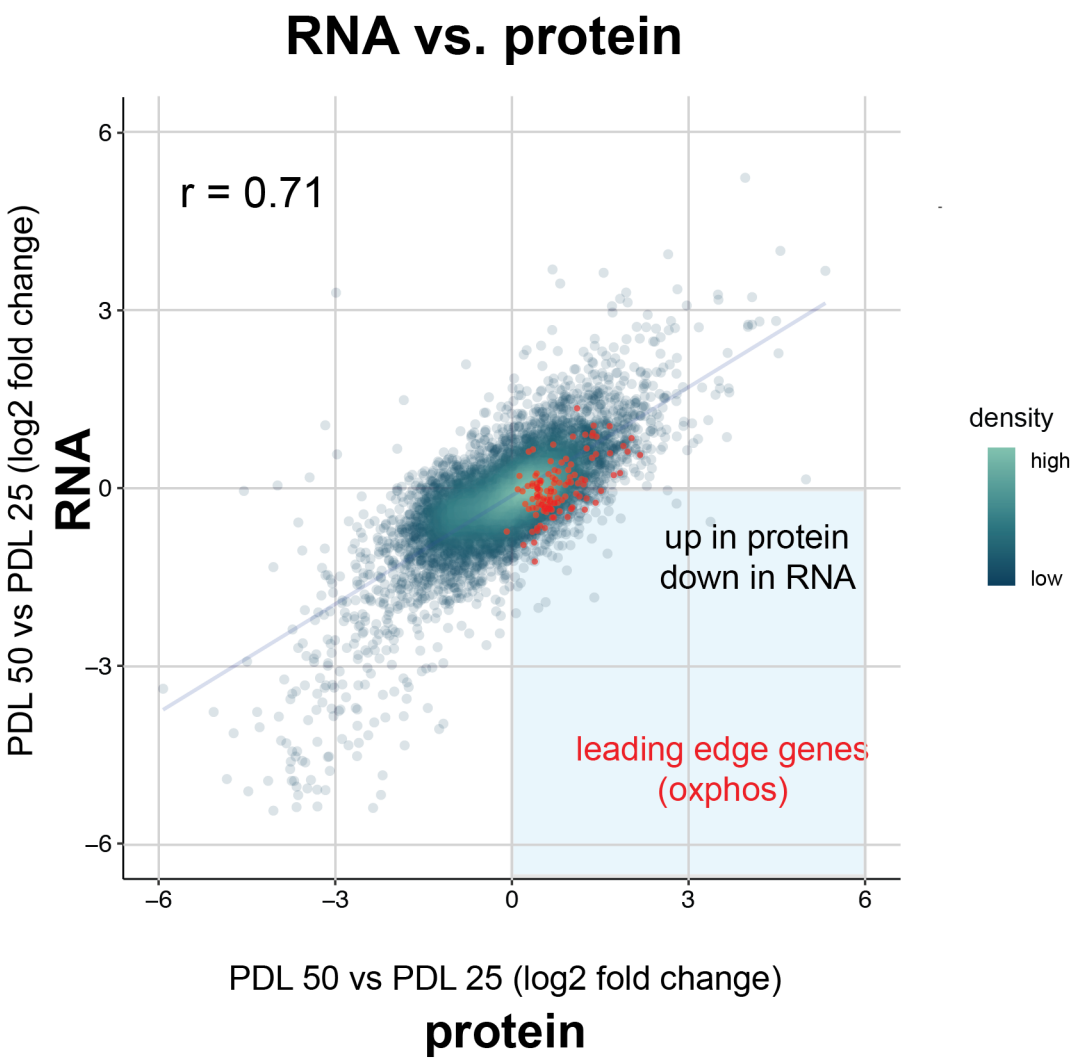

Figure 3–Figure supplement 2. Scatterplot comparing the log2 fold change expression of genes (x-axis) vs. protein (y-axis) in PDL 50 cells relative to PDL 20 cells. Oxidative phosphorylation leading edge genes from GSEA plotted in red. Point density colored from high (white) to low (green).

bioRxiv preprint doi: https://doi.org/10.1101/2021.05.03.442497; this version posted November 12, 2021. The copyright holder for this preprint (which was not certified by peer review) is the author/funder. All rights reserved. No reuse allowed without permission.

Figure 3–Figure supplement 3. Breakdown of the hallmark oxidative phosphorylation gene set into functional subsets reveals up regulation of most mitochondrial functions during replicative senescence. Heatmaps of log2 fold change proteomics data for the MSigDB hallmarks oxidative phosphorylation annotations set broken into constituent functional groups. Key in lower right with x-axis labels and color scale boundaries for all heatmaps.

bioRxiv preprint doi: https://doi.org/10.1101/2021.05.03.442497; this version posted November 12, 2021. The copyright holder for this preprint (which was not certified by peer review) is the author/funder. All rights reserved. No reuse allowed without permission.

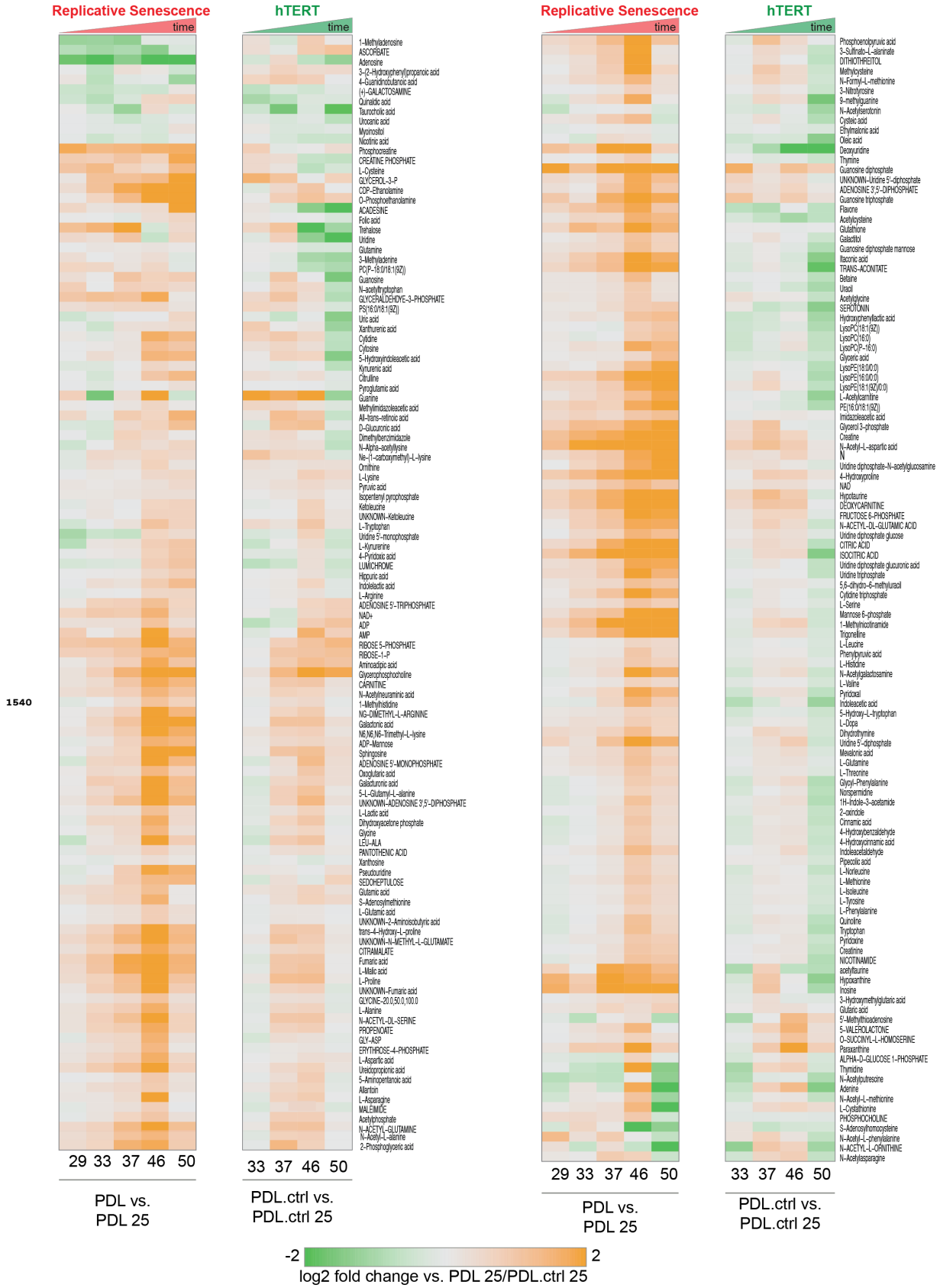

Figure 3–Figure supplement 4. PDL-dependent changes in the senescent metabolome vs hTERT cells. Heatmap of hierarchical clustering of 285 metabolite log2 fold changes at each PDL or PDL.ctrl versus first (not shown) for RS WT WI-38 (left) and hTERT WI-38 cells (right). Values range from high induction (orange) to depletion (green). Values shown are log2 Median values for n=4 replicates.

bioRxiv preprint doi: https://doi.org/10.1101/2021.05.03.442497; this version posted November 12, 2021. The copyright holder for this preprint (which was not certified by peer review) is the author/funder. All rights reserved. No reuse allowed without permission.

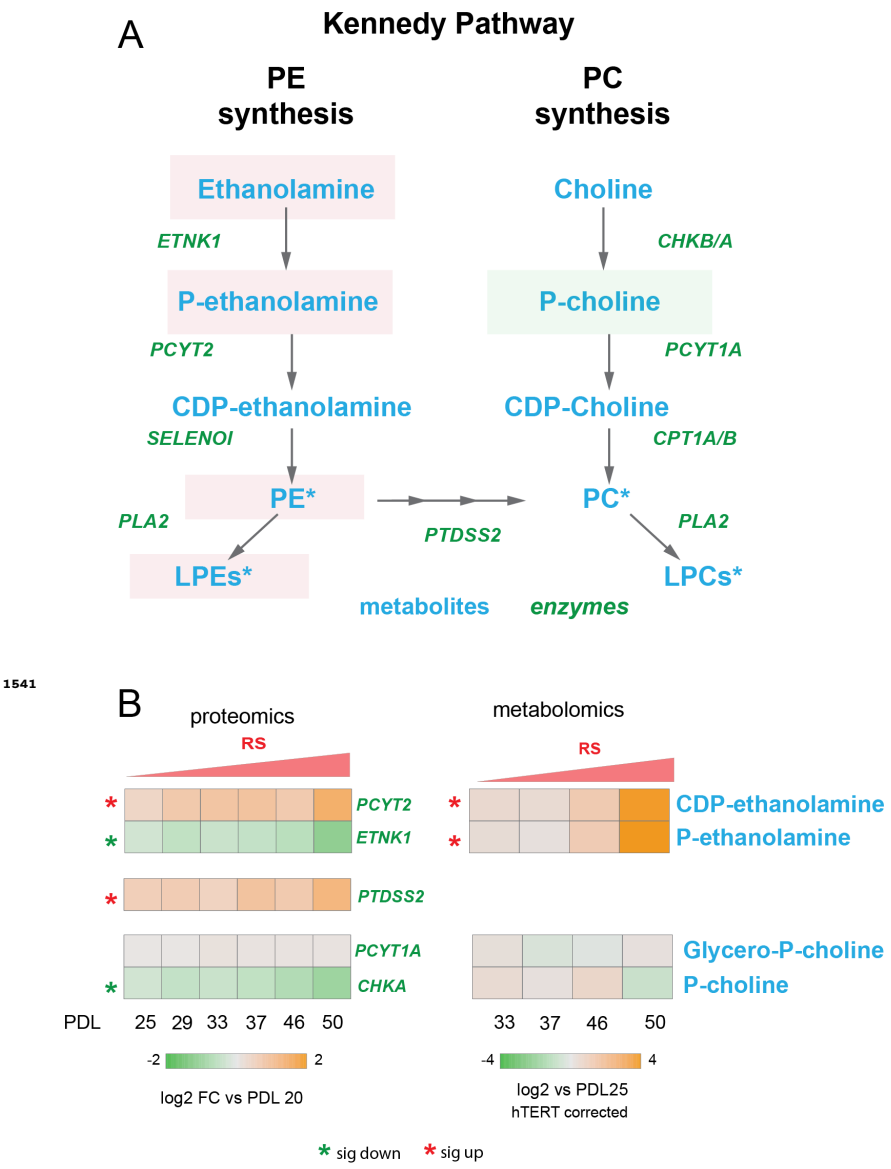

Figure 3–Figure supplement 5. Kennedy Pathway diagram. Metabolites in blue, proteins in italicized green. Heatmaps of log2 fold changes for metabolites and proteins from A. Median htert corrected values for n=4 replicates are shown. Significant changes (FDR adjusted p<0.05 metabolomics, FDR adjusted p<0.01 proteomics) during replicative senescence are denoted with asterisks.

bioRxiv preprint doi: https://doi.org/10.1101/2021.05.03.442497; this version posted November 12, 2021. The copyright holder for this preprint (which was not certified by peer review) is the author/funder. All rights reserved. No reuse allowed without permission.

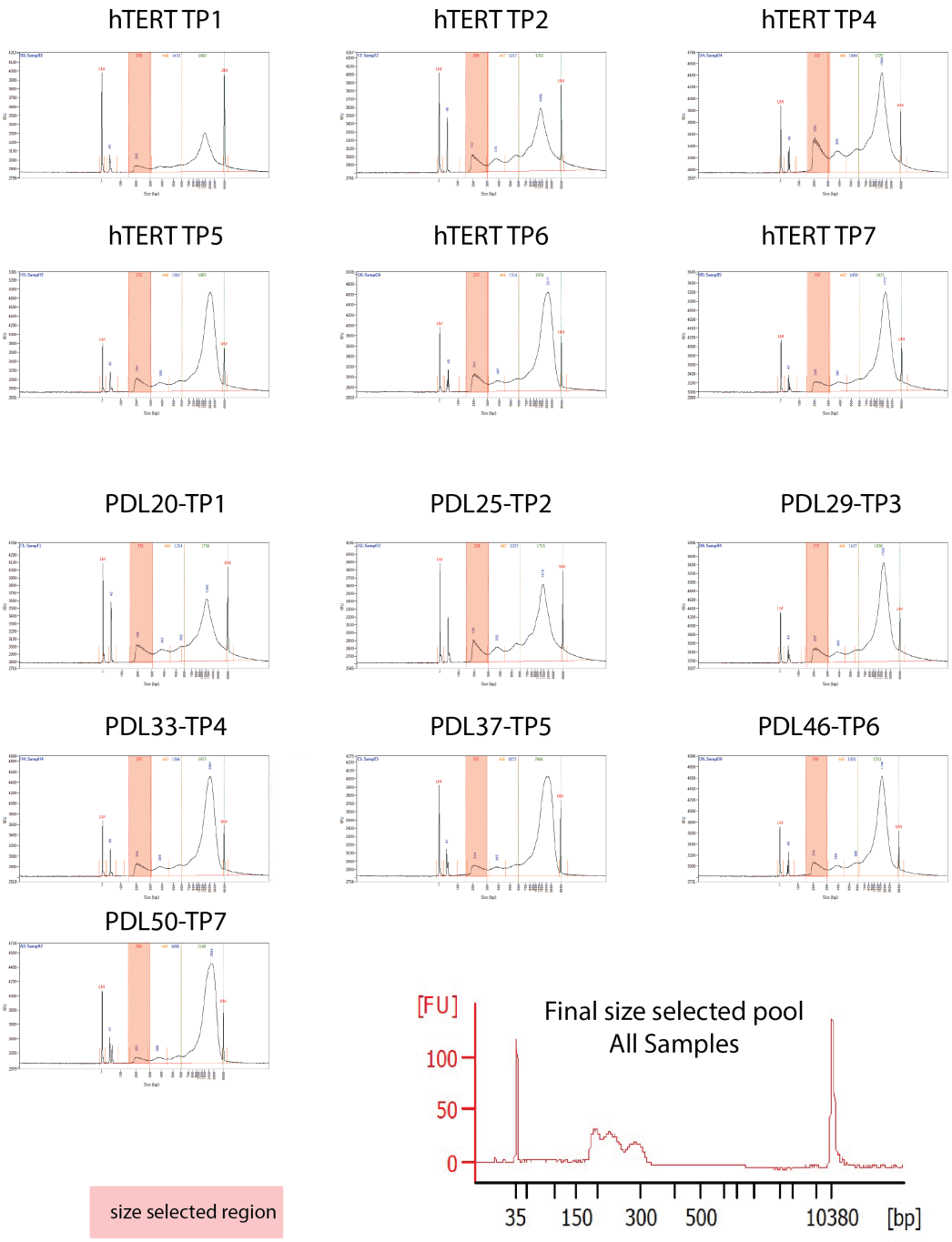

Figure 5–Figure supplement 1. ATAC-seq library fragment distribution and size selection.

bioRxiv preprint doi: https://doi.org/10.1101/2021.05.03.442497; this version posted November 12, 2021. The copyright holder for this preprint (which was not certified by peer review) is the author/funder. All rights reserved. No reuse allowed without permission.

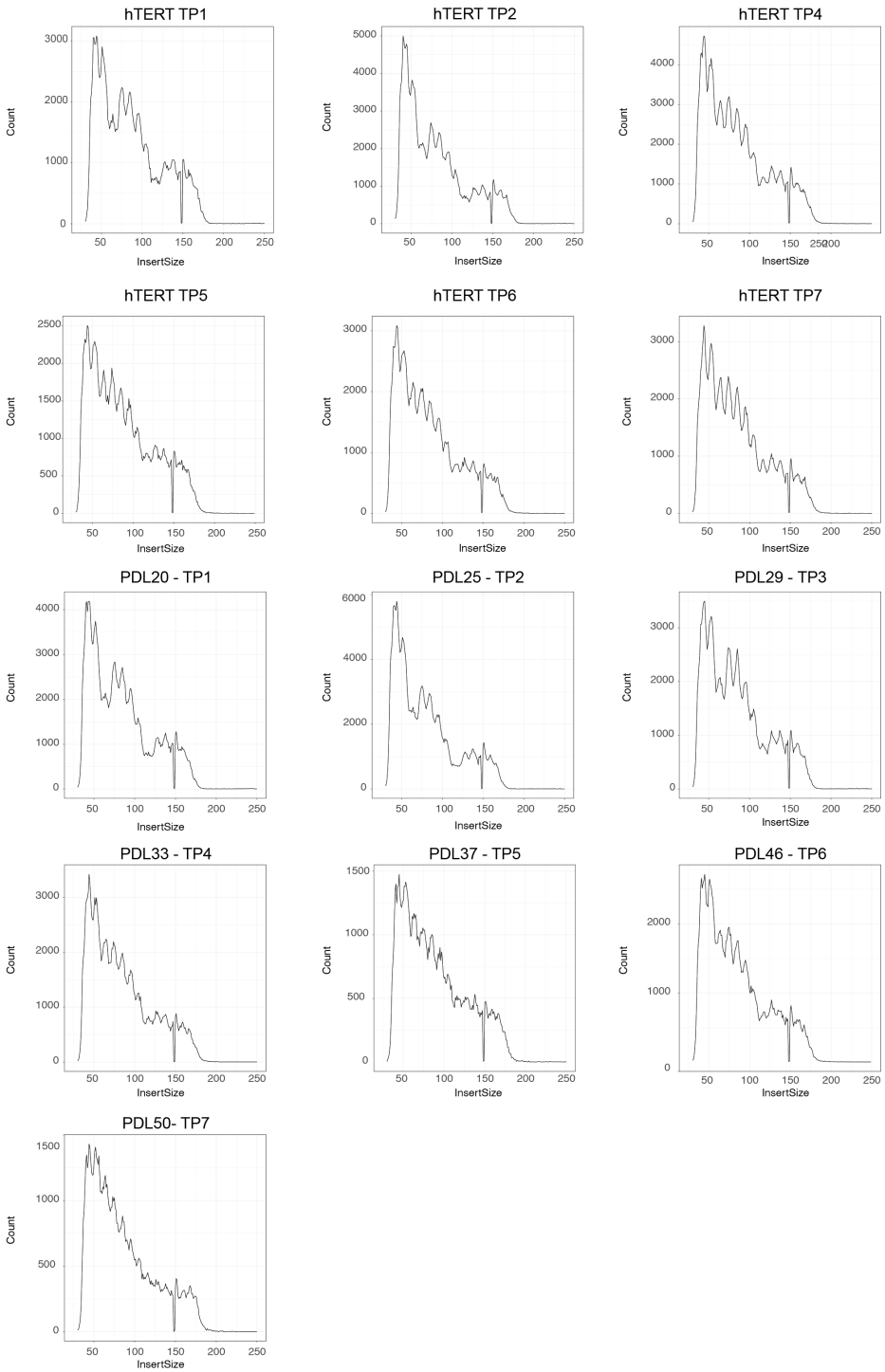

Figure 5–Figure supplement 2. ATAC-seq library fragment distribution after size selection and sequencing

bioRxiv preprint doi: https://doi.org/10.1101/2021.05.03.442497; this version posted November 12, 2021. The copyright holder for this preprint (which was not certified by peer review) is the author/funder. All rights reserved. No reuse allowed without permission.

A

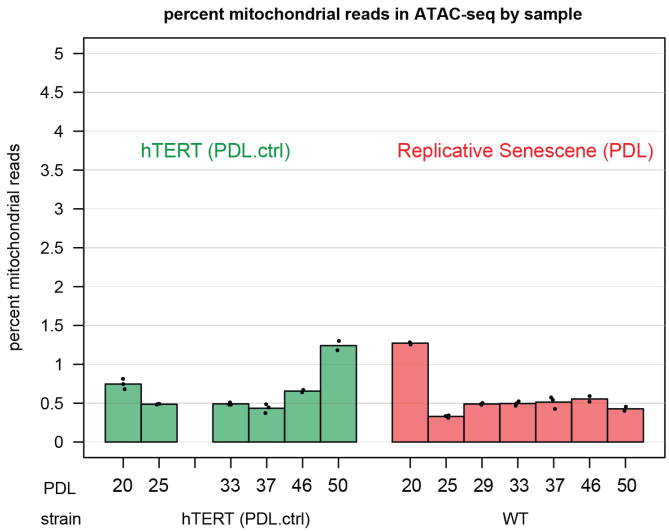

B

1544

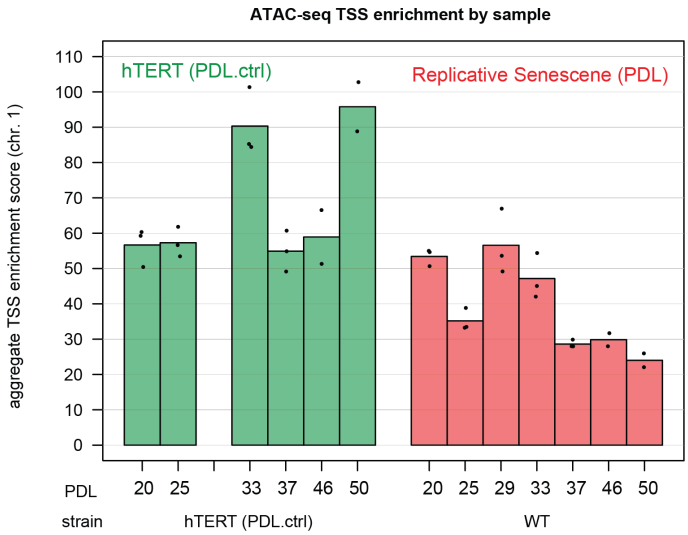

Figure 5–Figure supplement 3. ATAC-seq mitochondrial read percentages and ATAC-seq transcriptional start site enrichment. **(A)** Mitochondrial read percentages in sequenced and aligned ATAC-seq library for WT PDLs (red) hTERT time points (green) in triplicate. **(B)** Transcriptional start site enrichment in sequenced and aligned ATAC-seq libraries for WT PDLs (red) hTERT time points (green) in triplicate.

bioRxiv preprint doi: https://doi.org/10.1101/2021.05.03.442497; this version posted November 12, 2021. The copyright holder for this preprint (which was not certified by peer review) is the author/funder. All rights reserved. No reuse allowed without permission.

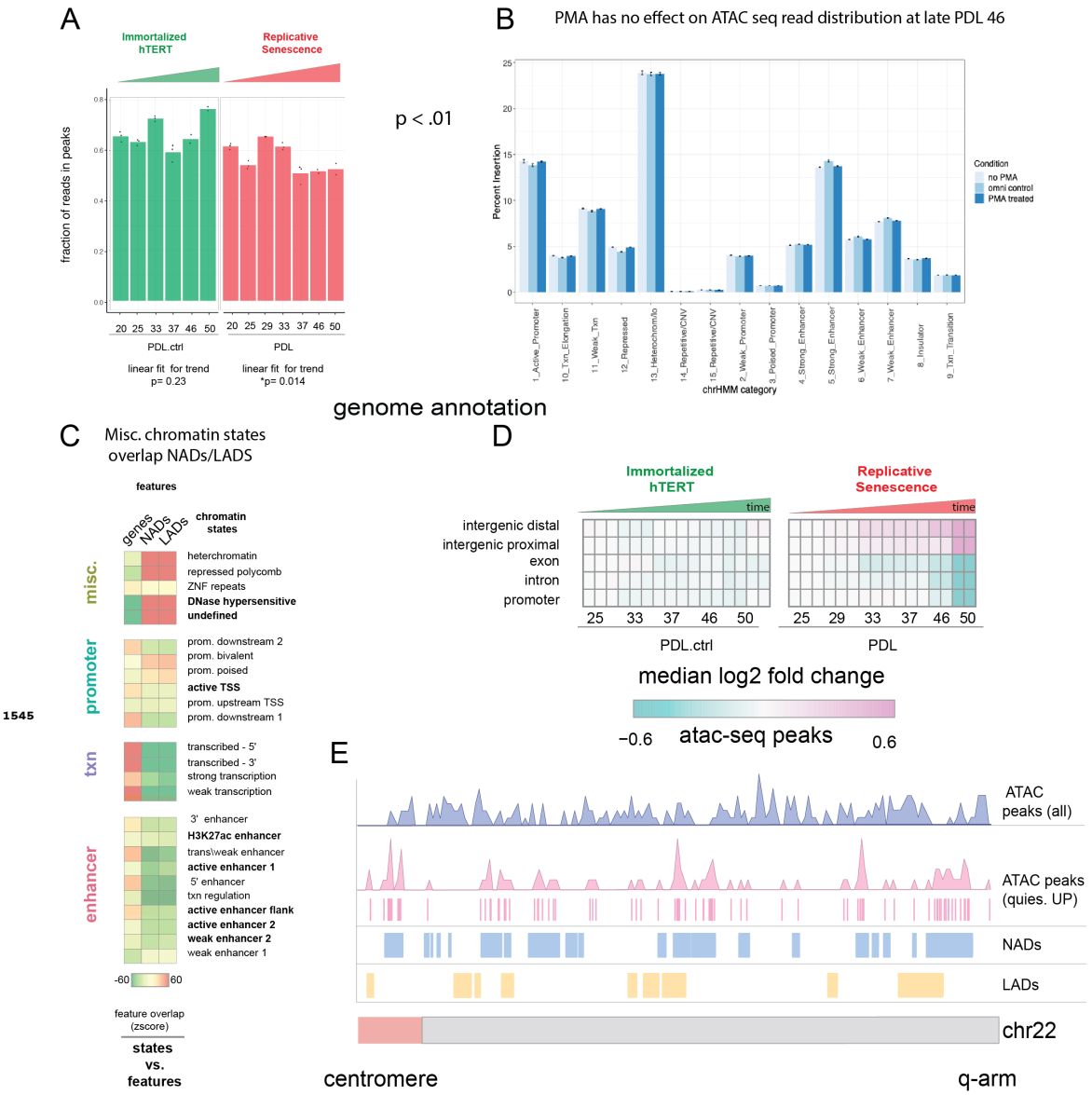

Figure 5–Figure supplement 4. ATAC-seq QC metrics, controls, and NADs/LADs browser shot. **(A)** Fraction of reads in peak by PDL (WT) and PDL.ctrl (hTERT).p values for linear fit over time are shown. WT cells exhibit a slight ~5% but significant reduction of fraction of reads in peaks. **(B)** PDL 46 read distribution across chromatin states +/- PMA. **(C)** Chromatin state overlap Z-scores for genes annotations and NADs and gene annotation and LADs. **(D)** Heatmap of median log2 fold change of ATAC-seq peak accessibility binned by genomic annotations (TxDb.Hsapiens.UCSC.hg38.knownGene–row) for each sample (column, n=2 or 3 replicates). Reference samples are PDL 20 or PDL 20.ctrl for WT and hTERT WI-38 cells respectively (not shown). **(E)** Chromosome level distribution of all ATAC-seq peaks (purple), ATAC-seq peaks increasing in accessibility located within the undefined/quiescent chromatin state annotation (pink), NADs (blue) and LADs (yellow).

bioRxiv preprint doi: https://doi.org/10.1101/2021.05.03.442497; this version posted November 12, 2021. The copyright holder for this preprint (which was not certified by peer review) is the author/funder. All rights reserved. No reuse allowed without permission.

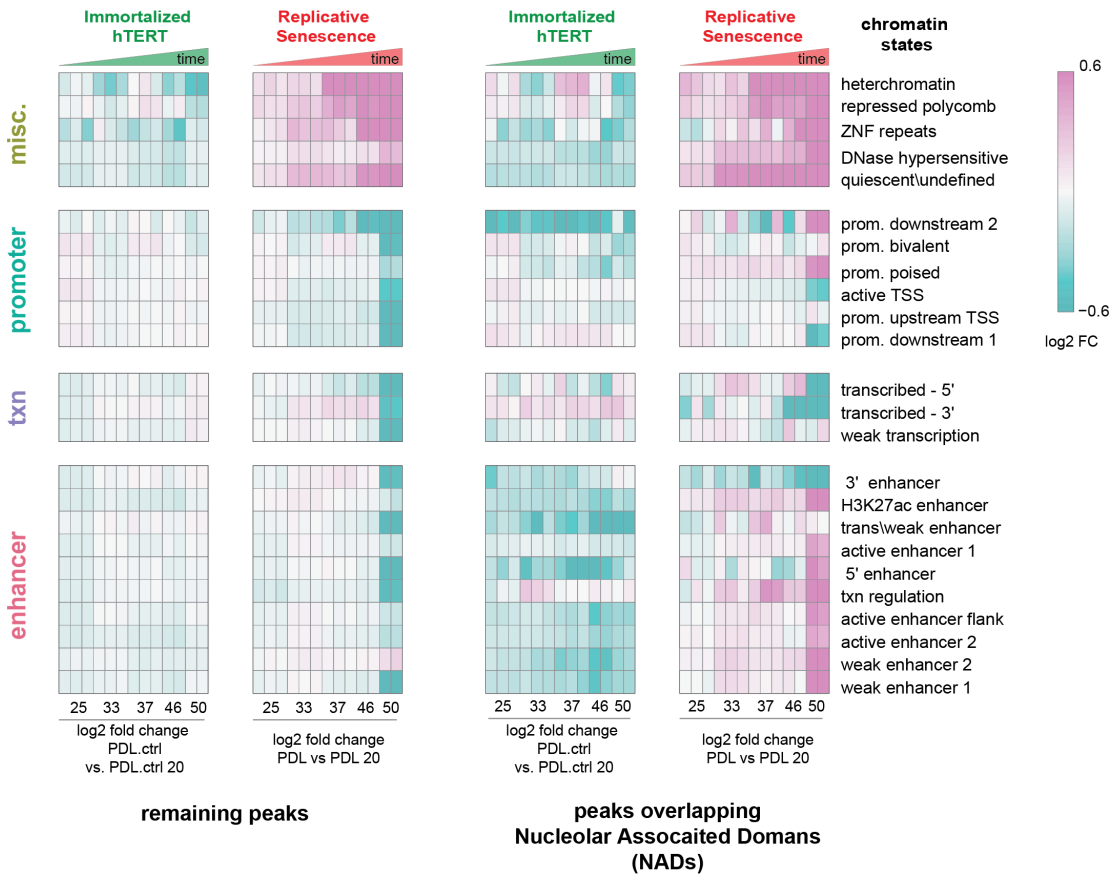

Figure 5–Figure supplement 5. Chromatin state profiles of ATAC-seq peaks in nucleolar associated domains (NADs) vs rest of the genome. Heatmap of all significant ATAC-seq peaks categorized by 25 chromatin states and then divided into peaks overlapping with NADs (right) and peaks excluded from NADs (left) for hTERT and WT replicative senescence time course. Normalized accessibility counts for peaks were aggregated by chromatin state and NAD overlap group. Values shown are log2 fold change of median accessibility for each time point and grouping versus the reference sample. PDL.ctrl 20 for hTERT and PDL 20 for WT replicative senescence time course. n=2 or 3 replicates.

bioRxiv preprint doi: https://doi.org/10.1101/2021.05.03.442497; this version posted November 12, 2021. The copyright holder for this preprint (which was not certified by peer review) is the author/funder. All rights reserved. No reuse allowed without permission.

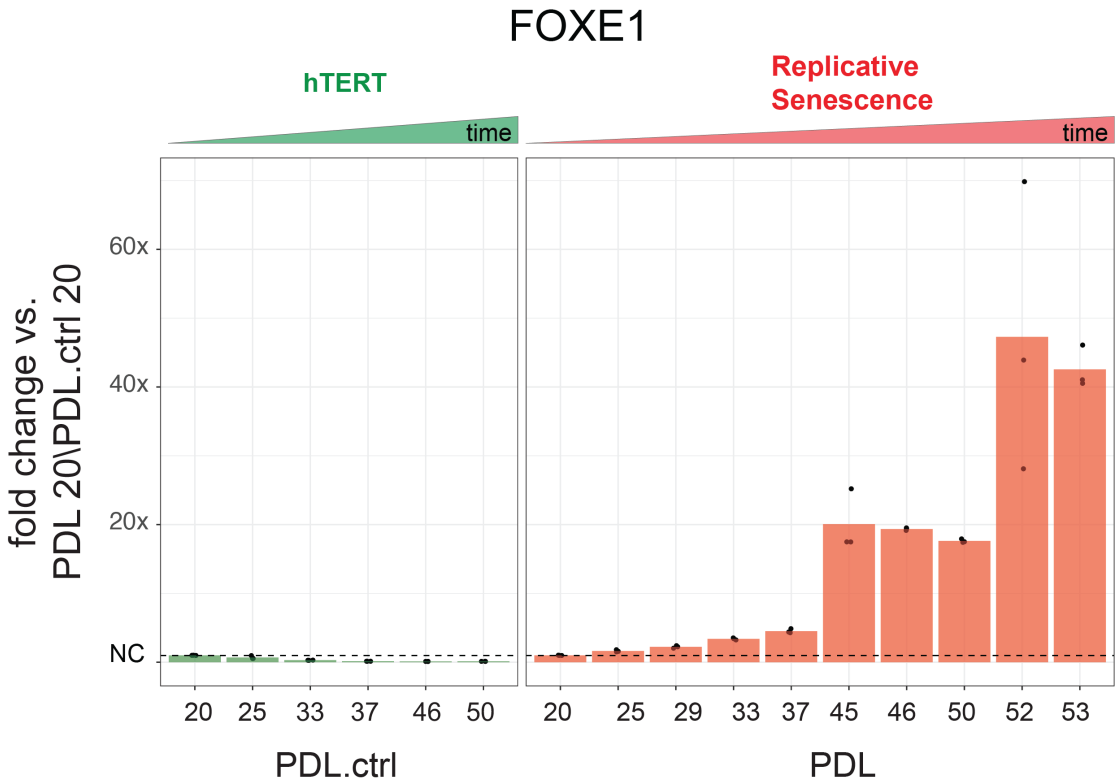

Figure 6–Figure supplement 1. Gene expression fold changes for the transcription factor FOXE1 across conditions. Gene expression fold changes (3 replicate average, each point a replicate) for the transcription factor FOXE1 in the hTERT and replicative senescence (RS) time courses.

bioRxiv preprint doi: https://doi.org/10.1101/2021.05.03.442497; this version posted November 12, 2021. The copyright holder for this preprint (which was not certified by peer review) is the author/funder. All rights reserved. No reuse allowed without permission.

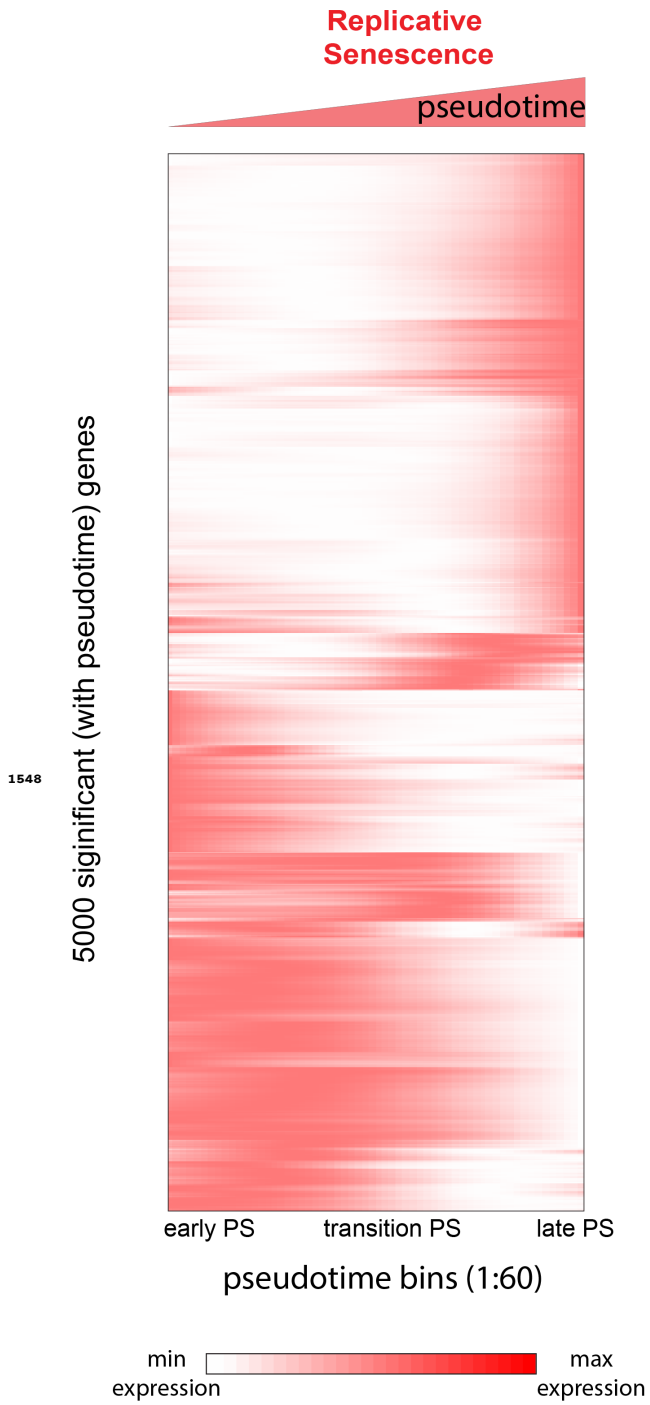

Figure 7–Figure supplement 1. Heatmap of gene expression changes for the top 5,000 significantly changing genes during replicative senescence pseudotime. Genes were hierarchically clustered, gene normalized and scaled (0-1) expression levels are depicted (white = low expression, red = high expression).

bioRxiv preprint doi: https://doi.org/10.1101/2021.05.03.442497; this version posted November 12, 2021. The copyright holder for this preprint (which was not certified by peer review) is the author/funder. All rights reserved. No reuse allowed without permission.

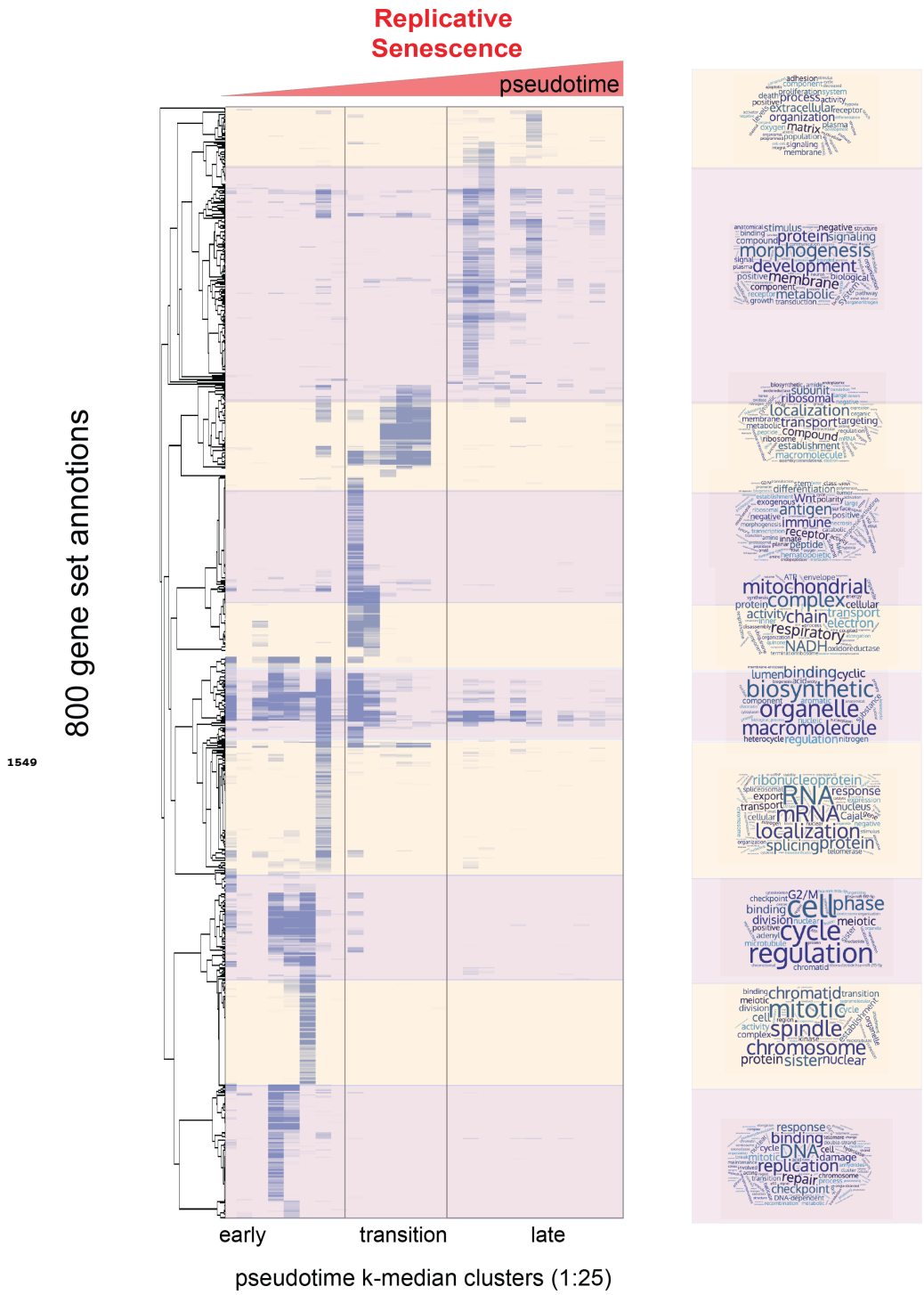

Figure 7–Figure supplement 2. Heatmap of enriched gene sets for replicative senescence pseudotime clusters (k-25). Heatmap of adjusted p-values for GO-term enrichment analysis on individual clusters from 6. Values plotted are row normalized -log10 p-value; light purple to dark purple. The ordered pseudotime clusters are shown on the x-axis while hierarchically clustered gene sets are shown on the y-axis. Hierarchical clustering of gene set enrichment was used to divide gene sets into 10 major clusters. GO-term names were used to create word clouds reflective of the types and functions of enriched gene sets.

bioRxiv preprint doi: https://doi.org/10.1101/2021.05.03.442497; this version posted November 12, 2021. The copyright holder for this preprint (which was not certified by peer review) is the author/funder. All rights reserved. No reuse allowed without permission.

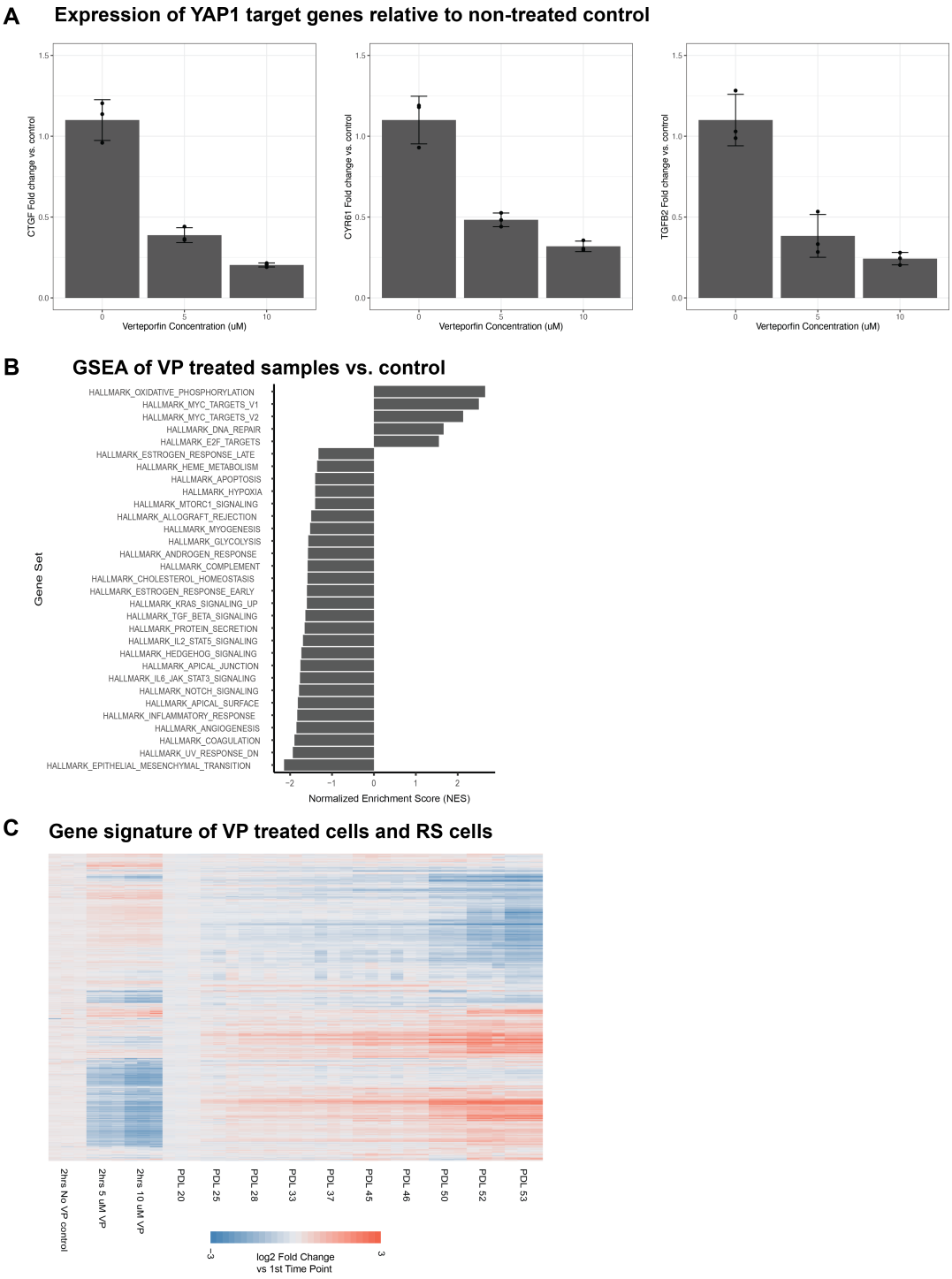

Figure 8–Figure supplement 1. Effect of inhibiting the YAP1/TEAD1 interaction with verteporfin treatment on WI-38 cells. **(A)** Barplots of the gene expression of 3 known YAP1 gene targets in verteporfin treated cells. Values plotted are fold changes relative to the mean of the control samples. Each condition was sampled at triplicate. Error bars indicate the standard deviation from the mean. **(B)** Barplot representing significant normalized enrichment score for each enrichment term from the MSigDB Hallmarks annotation. FDR adjusted p-values < 0.01. **(C)** Heatmap comparing gene expression changes in replicative senescence and verteporfin treated WI-38 cells. Values plotted are log2 fold change relative to the first time point in each experiment.